Solid-State NMR Investigations of Extracellular Matrixes and Cell Walls of Algae, Bacteria, Fungi, and Plants

Nader Ghassemi, Alexandre Poulhazan, Fabien Deligey, Frederic Mentink-Vigier, Isabelle Marcotte, and Tuo Wang*

Cite This: https://doi.org/10.1021/acs.chemrev.1c00669

Read Online

ACCESS | Metrics & More | Article Recommendations

ABSTRACT: Extracellular matrixes (ECMs), such as the cell walls and biofilms, are important for supporting cell integrity and function and regulating intercellular communication. These biomaterials are also of significant interest to the production of biofuels and the development of antimicrobial treatment. Solid-state nuclear magnetic resonance (ssNMR) and magic-angle spinning-dynamic nuclear polarization (MAS-DNP) are uniquely powerful for understanding the conformational structure, dynamical characteristics, and supramolecular assemblies of carbohydrates and other biomolecules in ECMs. This review highlights the recent high-resolution investigations of intact ECMs and native cells in many organisms spanning across plants, bacteria, fungi, and algae. We spotlight the structural principles identified in ECMs, discuss the current technical limitation and underexplored biochemical topics, and point out the promising opportunities enabled by the recent advances of the rapidly evolving ssNMR technology.

CONTENTS

1. INTRODUCTION

1.1. Current Status of NMR Research on Extracellular Matrixes

Exposed to environmental stresses, living organisms have developed the extracellular matrix (ECM) to regulate the integrity and communication of cells. Although the plasma membrane determines the cell border, bacterial, fungal, plant, and algal cells are further covered by a carbohydrate-rich layer called the cell wall, which plays pivotal roles in protecting the cell cytoplasm from contaminants and other stresses and in supporting cellular growth and differentiation.[1−4] Bacterial and fungal ECMs, such as cell walls and biofilms, are associated with toxicity and virulence and serve as the targets of many antifungals and antibiotics.[5−7] The ECM materials are highly diverse in molecular composition and ultrastructure, accommodating carbohydrates, proteins, lipids, polyphenols, and occasionally some inorganic components. A large collection of methods based on vibrational spectroscopy, biochemical assays, chromatography coupled with mass spectrometry, neutron and X-ray diffraction, as well as imaging methods have been employed to analyze the composition and architecture of these biocomposites on different length scales, from covalent linkage patterns to microscopic-level arrangement of polymer meshes.[8−12]

Benefited from the nondestructive nature and atomic-level resolution, nuclear magnetic resonance (NMR) has proven to be a useful tool for analyzing biomolecules in many organisms.[13] The number of annual NMR publications on topics related to plants, bacteria, algae, and fungi has increased by 9-fold over the past three decades, from slightly over 300 papers in 1991 to more than 2700 studies in 2020, with around 37,000 accumulated studies over this period (Figure 1). The number of studies decreases sequentially in the research fields of plants, bacteria, fungi, and then algae. Most solution NMR investigations focus on metabolite identification and structural determination, but isolation, chemical modification, and solubilization procedures are often required before ECM material could be subjected to structural characterization, which can compromise the physical properties and chemical structures of biomacromolecules.[14,15] In response to this technical obstacle, solid-state NMR (ssNMR) has emerged as a promising technique for investigating intact ECM material using intact insoluble materials and even whole cells and organisms that are free from chemical treatments.[16−20] Since 1991, around 1700 ssNMR studies have been conducted on bacteria, fungi, algae, and plants, with the majority (more than 1000 articles) published after 2011. These ssNMR investigations were mainly focused on plants (47%) and bacteria (32%), while fungi (17%) and algae (4%) are under-investigated. Expedited by the development of high-field ssNMR and magic-angle spinning dynamic nuclear polarization (MAS-DNP) techniques,[21−24] a rapid expansion of ssNMR applications on ECM materials is expected in the near future.

This review emphasizes the cell walls and biofilms of two pathogenic microbes, namely, bacteria and fungi, as well as the biomass of two photosynthetic organisms, i.e., algae and plants. We will focus on the panorama of ssNMR research published in the past decade, which has combined structural and dynamical angles to describe the nanoscale architecture of cell walls. Specific consideration is devoted to the applications of multidimensional (2D/3D) correlation methods to isotopically enriched cell-wall materials,[17,18] providing sufficient sensitivity and resolution for understanding such complex biosystems. We will highlight the experimental protocols and data interpretation pathways for deriving the varied compositions and polymorphic structures of biomacromolecules along with their nanoscale assembly and the formation of integrated networks. We will also discuss the possibility of investigating unlabeled biomaterials as enabled by technical advances in MAS-DNP and proton-detection techniques.[27,28] The methodology and structural schemes summarized here will guide the ongoing investigations of the modes of action and structural effects of antimicrobial therapies and facilitate the development of cost-effective production of bioenergy and biopolymers.

1.2. Structural Components of Extracellular Matrixes

ECM biomaterials are hierarchical assemblies of covalently linked and/or physically stacked polysaccharides and glyco-conjugates, which are formed by an array of relatively simple building blocks: the monosaccharides (Figure 2). These supramolecular networks are highly complex and diverse in structures and functions. The organization of bacterial cell walls can substantially differ in the Gram-positive (such as *Staphylococcus aureus*) and Gram-negative (such as *Escherichia coli*) species, leading to distinct cell morphologies and different mechanisms of action for antibiotics.[2,29] Underneath the capsule of Gram-positive bacteria, there is a cell-wall layer rich in
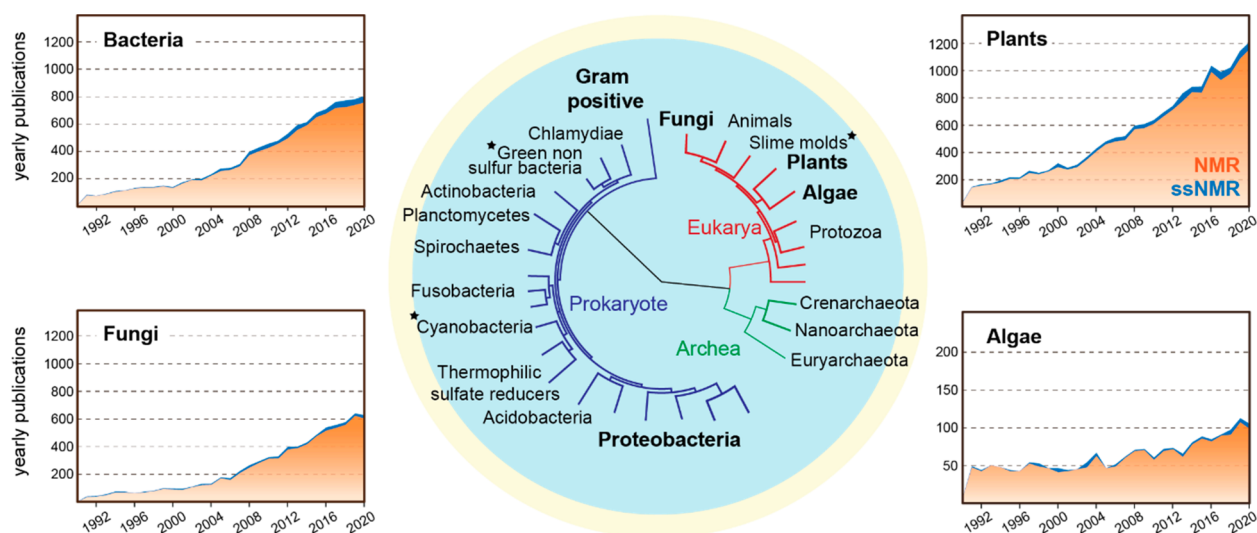
Figure 1. NMR studies of various organisms. A simplified phylogenetic tree of organisms based on genetic sequencing presents the diversity and evolutionary relationships between biological species.[25,26] The organisms described in this review are in bold, with their associated number of NMR publications summarized as four separate panels. The annual number of publications between 1991 and 2020 has been plotted using data indexed by Web of Science. Asterisks in the central plot indicate other organisms that have also been categorized. Most of the published works were focused on plants or bacteria.

peptidoglycan (PG) anchored in the plasma membrane via lipoteichoic acid (LTA), which assemble into a thick and compact crust covering the cell surface. On the contrary, Gram-negative bacteria have a thin layer of periplasmic peptidoglycan that is sandwiched between the permeable lipopolysaccharide (LPS)-rich outer membrane and the internal phospholipid-rich plasma membrane. A fundamental molecule present in both groups is the PG, which is made up of linear polysaccharides (typically 50−250 disaccharide long) and linked to small peptides (usually up to five amino acid residues).[7,30]

Bacteria infect animal tissues not only as a single cell but also through a multicellular arrangement called biofilm. Biofilms enable the cohabitation of cells and preserve a safe environment for bacteria communities to evolve and resist chemical and physiological reactions, thus becoming a major contributor to the globally increasing multidrug resistance.[31,32] On the other hand, such biomaterial also has promising applications in aquatic biofouling[33] and medical sterilization.[32] Biofilms are mostly made of proteins (e.g., functional amyloids) but can also be accompanied by other biomolecules including polysaccharides (such as cellulose derivatives) and lipid components.[34−36]

The cell wall is also present in another pathogenic microorganism, the fungus. Over 3 million patients are exposed to invasive fungal infections annually, and around half of them die despite antifungal treatment.[5,37,38] Fungal infections can also cause morbidities such as asthma, allergy, chronic skin infections, and keratitis.[5] In addition, immunosuppressive medical interventions, the widespread cases of AIDS, and the outbreak of the COVID-19 pandemic rampantly elevate the risk of fungi infections.[39,40] The mechanical strength and plasticity of fungal cell walls are essential for preserving cellular viability, adjusting cellular permeability, and enduring osmotic stresses.[41,42] Some of the cell-wall components, such as β-glucans and mannans, are the main targets for antibodies in the diagnosis of fungal infection.[43] Benefited from their unique chemical identities and absence in the host cells, fungal polysaccharides are also ideal targets for antifungal agents. Recently, three inhibitors of β-1,3-glucan biosynthesis, all of

which are lipopeptide compounds from the echinocandin family, have been clinically approved and are currently used in medical therapies.[44,45]

As mentioned, fungal cell walls are primarily made up of polysaccharides and glycoproteins, together with a low amount of pigments. These molecules are often immunogenic and promote cellular and humoral distortions when infections occur.[46] The major carbohydrate components include three commonly found polysaccharides, namely, the partially crystalline and rigid chitin (a long-chain polymer of *N*-acetylglucosamine), the cross-linking β-glucans, and the surface-exposed and protein-associated mannans (Figure 2).[47] In addition, galactosaminogalactan (GAG) and α-1,3-glucans represent two under-investigated molecules unique to certain fungal species.[48] The fungal cell wall is structurally dynamic, with a variable composition depending on the species, cell types (for example, hyphae or conidia), age, and environmental stresses. Previous ssNMR studies have primarily focused on three pathogenic fungi, *Cryptococcus neoformans*, *Aspergillus fumigatus*, and *Candida albicans*,[49−52] but the territory is rapidly expanding to other fungal species.

Plants and algae share a history of over 1 billion years through their ability to perform photosynthesis, with cell walls being the product of energy conversion and carbon capture.[53] As ancestors of higher plants, most microalgae are protected by a plant-like cell wall. However, a glycoprotein-rich cell wall is frequently found in Volvocales (e.g., *Chlamydomonas sp.*), while partially mineralized fungi-like matrixes with a high amount of chitin protect some diatoms such as *Cyclotella* and *Thalassiosira* (Figure 2).[54−56]

Land plants evolved from Charophyceae microalgae,[57] which conquered freshwater habitats, but both are thought to be the result of endosymbiosis with a cyanobacterium.[53,58,59] While displaying a diverse geometry according to their function,[60] plant cells are typically made of two distinct walls. Present in all plants and formed during cytokinesis, the primary cell wall is characterized by a high extendibility to accommodate plant growth.[61,62] The secondary cell wall is usually deposited after

C
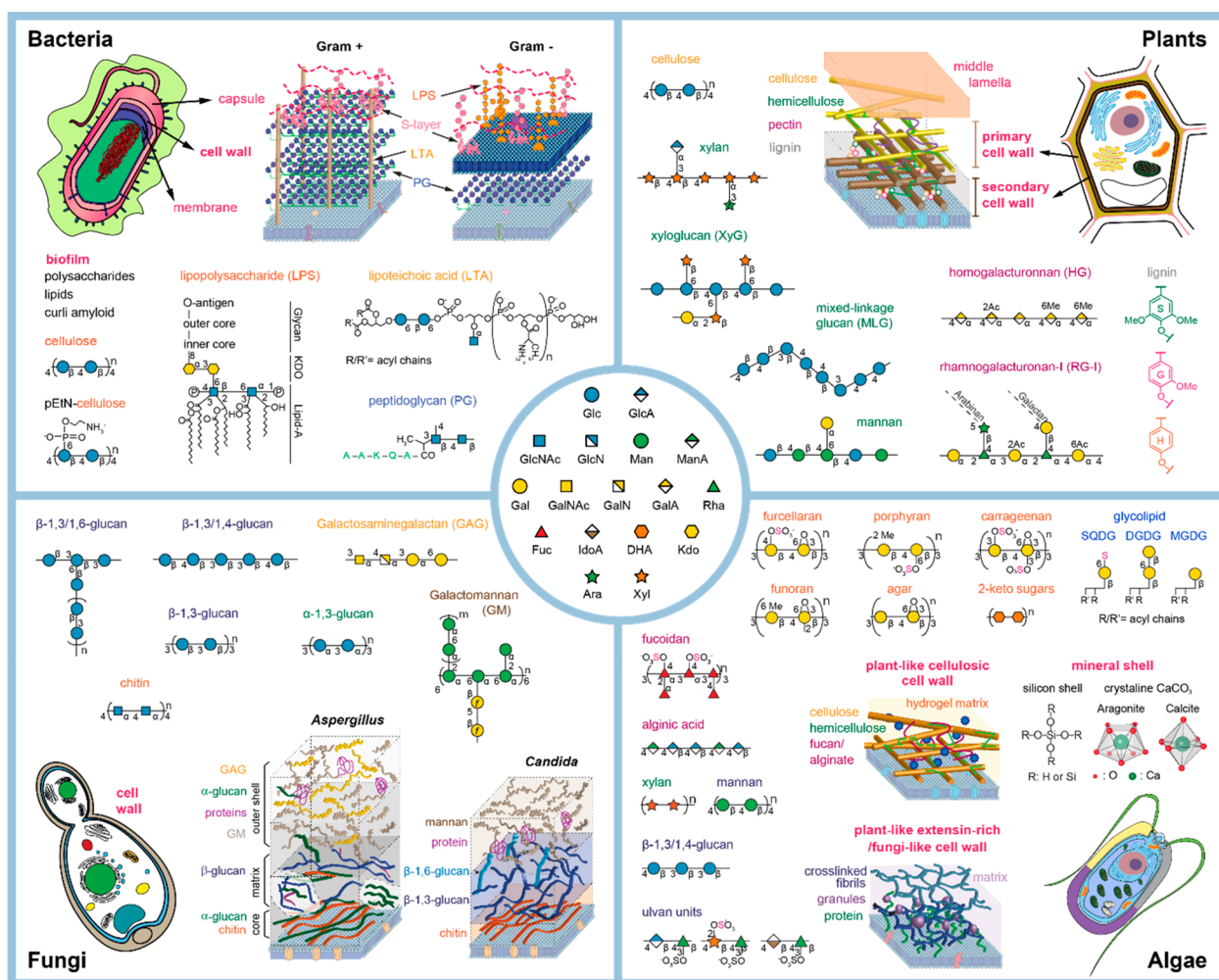
Figure 2. Simplified representation of cell walls and biomolecules studied by ssNMR. Built from very fundamental monosaccharide units (central panel), the polymerized carbohydrate components exhibit highly diverse structures and can associate with each other and other molecules to form the cell-wall materials in bacteria (top left), plants (top right), fungi (bottom left), and algae (bottom right). The structural schemes of molecules and ECMs are briefly summarized in section 1.2 and will guide the detailed discussions in later sections.

cell expansion has ceased, further strengthening the resilience and mechanical integrity.[63] Both cell walls contain rigid scaffolds of cellulose microfibrils enclosed in a soft matrix, which is a mesh formed by hemicellulose and pectin in primary cell walls but changes to a hemicellulose and lignin mixture in secondary cell walls.[64−67] Understanding the polymer network in such lignocellulosic biomass will facilitate the development of more digestible crops and cost-effective conversion technology for biofuel production.[68−70]

2. SOLID-STATE NMR SPECTROSCOPY AND MAS-DNP METHODOLOGY

2.1. A Practical Guide of ssNMR Techniques for ECM Characterization

The use of the ssNMR technique minimizes and sometimes eliminates the need for purification and isolation, allowing for the characterization of intact ECM materials or native cells. However, these advantages come with two challenges: the intrinsically low sensitivity of NMR and the often-insufficient resolution for cellular studies. Here we briefly discuss the fundamental phenomena underlying the technical difficulties in investigating ECM materials. More in-depth descriptions of NMR spectroscopy can be found in multiple references.[71−73]

Many of the ssNMR studies of ECMs are using intact cells or tissues. In-cell ssNMR studies can be conducted on four categories of samples, including purified molecules or simplified and reconstituted systems (*in vitro*), extracted but structurally preserved macromolecular complexes such as the cell envelope (*ex vivo/ex situ*), intact but metabolically compromised cells (*in situ*/in cell/whole cell; often without awareness of the cell viability), and recently living cells directly packed into MAS rotors (*in vivo*).[49,50,74−82] Studying living cells using ssNMR presents an attractive research avenue, but careful consideration should be given regarding the sample preparation and experimental conditions. Recently, Frederick et al. have proposed the use of viability measurements before and after the experiment to closely monitor the cell state under MAS-DNP investigations.[83] Since the spinning of the sample can induce centrifugal and dehydrating effects, the experimental time and spinning frequency should be moderated to maintain cell integrity and viability. Other factors include the physiological concentration of cells, the heating effect due to radiofrequency pulses, and the limited availability of media and nutrients in MAS rotors.

Solid-state NMR detects signals coming from the excitation of nuclear spins $^1/_2$ and above. Nuclear spins are sensitive to local
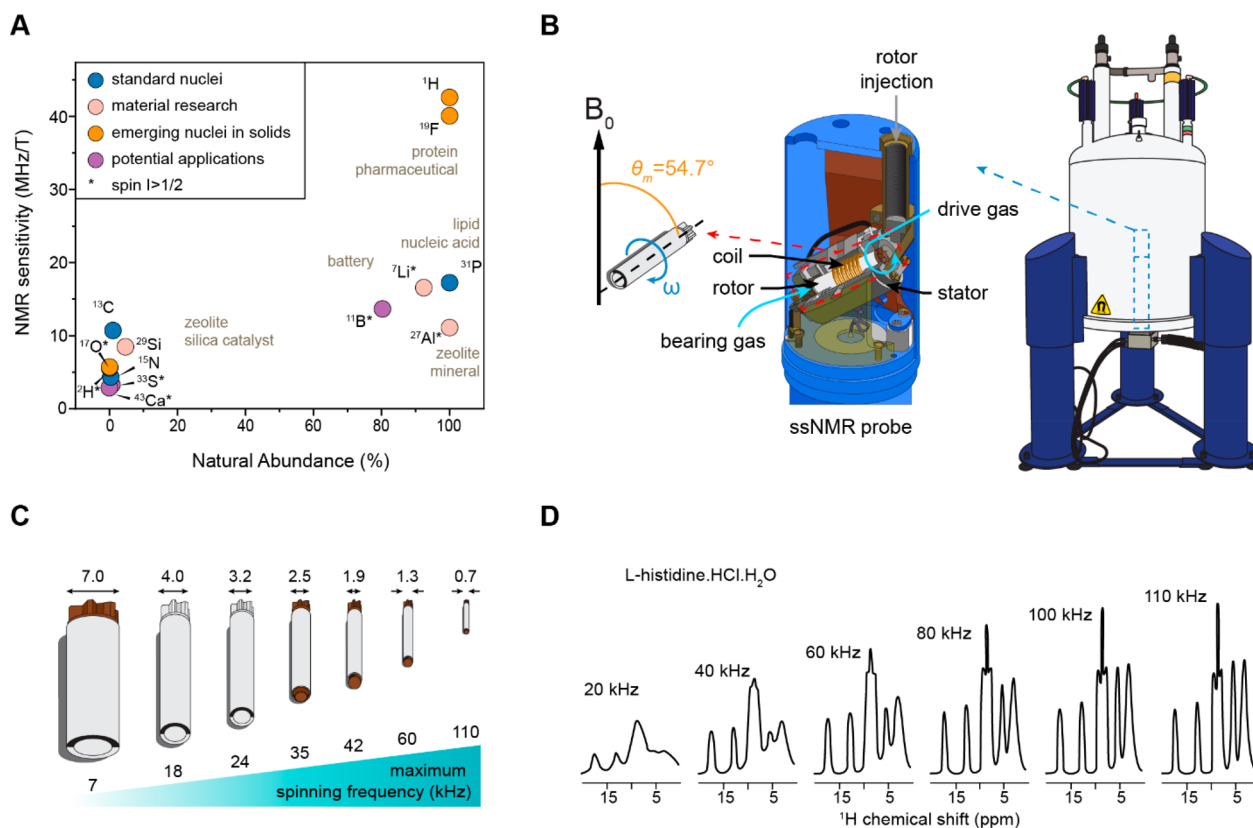
Figure 3. Technical aspects of ssNMR spectroscopy. (A) Typical NMR nuclei exploited in biomolecular and material research showing different sensitivities and natural abundances. ^{13}C, ^{15}N, and ^{31}P are the most common nuclei used for ECM research, while ^{1}H, ^{19}F, and ^{17}O are still underused. Quadrupolar nuclei are indicated using an asterisk. Common nuclei used in material research are also shown. (B) Solid-state NMR probe with radiofrequency emission and detection (coil), as well as bearing and driving gas for the MAS of the rotor containing the sample. (C) Various rotor diameters (mm) containing different sample quantities for reaching different MAS frequencies (kHz). (D) Proton detection in solids enabled by ultrafast MAS. The resolution increases with spinning speed. Panel D is adapted with permission from ref 98. Copyright 2016 Elsevier.

chemical environments and atomic interactions and, therefore, enable studying structural and dynamical parameters.[13,84] A large variety of nuclei are used in the investigation of biomolecules and functional materials, from protein structure determination to the functional scheme of catalysts and batteries (Figure 3A). Carbon-13 (^{13}C) is usually the standard nucleus for cellular ssNMR, as its chemical shift spans a sufficiently large range to resolve a huge number of chemically inequivalent carbon sites in carbohydrates, lipids, proteins, and polyphenol polymers.[85] Since the ^{13}C isotope has a small gyromagnetic ratio and a low natural abundance of 1.1%, isotopic enrichment is generally required to circumvent the challenges of limited sensitivity.[80,86] Proton (^{1}H) and oxygen-17 (^{17}O) are also pertinent nuclei for most biomolecules considering their elemental composition, but they are still underused in ECM research mainly due to the limited dispersion of chemical shifts or low abundance of these isotopes.[87−89] Nitrogen-15 (^{15}N) is useful for characterizing protein constituents and nitrogenated polysaccharides (such as chitin, chitosan, and GAG), and ^{31}P and ^{2}H are the key isotopes for characterizing lipid molecules such as glycolipids and phospholipids.[90−92] ^{2}H and ^{19}F are potential replacements of ^{1}H with minimal structural perturbation,[93−97] thus exhibiting an increasing interest in biomolecular ssNMR. Multiple exotic nuclei, such as ^{29}Si, ^{11}B, ^{43}Ca, and ^{33}S, might be of potential applications to the bioinorganic centers of ECMs, such as the borate esters and calcium egg boxes in pectin complexes as well as algal biosilica and sulfated molecules.

For solid-state samples, a complication appears: the chemical shift and many spin−spin interactions are orientation-dependent, which leads to broad spectra under static and non-oriented conditions, limiting both resolution and sensitivity. Magic-angle spinning (MAS) has thus been developed to average these anisotropic interactions.[99,100] Nowadays, static experiments are used only for specific cases and most ssNMR studies are conducted under MAS conditions. From the experimental perspective, a biological sample is packed into an MAS rotor to spin at an angle of 54.74° relative to the static magnetic field direction (Figure 3B). The outer diameter of commercial rotors typically varies from 0.7 to 7 mm, which can contain 0.5 to 500 mg of materials (Figure 3C). The MAS frequencies are mainly restricted by the rotor size; for example, a 0.7 mm rotor enables stable ultrafast spinning up to 111 kHz, which efficiently averages out ^{1}H−^{1}H dipolar couplings and enables high-resolution ^{1}H detection of protonated solids (Figure 3D).[88,101−103]

The NMR signal originates from the nonuniform distribution of the spin population. In particular, the population difference for spins distributed in different energy levels split by the Zeeman interactions (and further by interspin interactions) is the prime origin of the magnetic resonance phenomenon. The smaller the population difference, the lower the detected signal and the lower the sensitivity. Unfortunately, the energy diagram spans in the tens to hundreds of MHz regime which leads to a very small population difference when compared with the total number of spins in each state (in the range of $10^{-5}–10^{-4}$). This
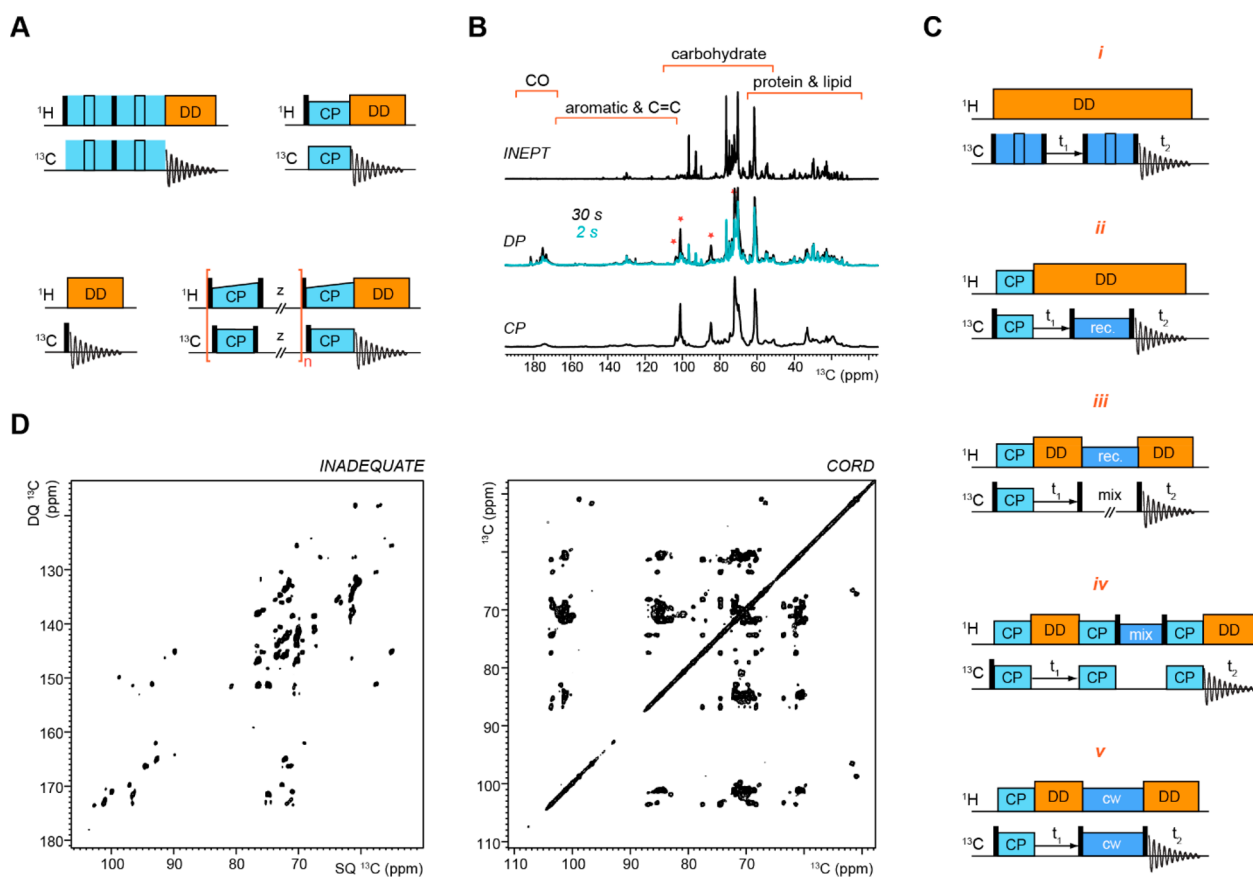
Figure 4. Representative ssNMR pulse sequences and spectra. (A) 1D ^{13}C experiments of refocused INEPT (top left), CP (top right), DP (bottom left), and MultiCP (bottom right). (B) Representative spectra collected on the living cells of *A. fumigatus*. From top to bottom are ^{13}C spectra measured using refocused INEPT, ^{13}C DP with long (30 s; black spectrum) and short (2 s; blue spectrum) recycle delays, and ^{13}C CP. Asterisks show the dephasing of signals from rigid components in the 2 s DP spectrum, which were enhanced in CP. (C) Five types (i−v) of ssNMR pulse sequences for measuring ^{13}C−^{13}C homonuclear correlation experiments. Abbreviations are used for the pulse sequences: cross-polarization (CP); dipolar decoupling (DD); recoupling (rec.); continuous wave (cw). (D) Representative 2D ^{13}C−^{13}C spectra measured using J-INADEQUATE (left) and CORD (right) experiments. All spectra shown here were collected on an 800 MHz NMR spectrometer on intact *A. fumigatus* cells.[49] Panels B and D are adapted with permission from ref 49. Copyright 2018 Springer Nature.

energy scale is what makes NMR a high-resolution technique but also one of the least-sensitive spectroscopic methods. The sensitivity of ssNMR is often evaluated using the signal-to-noise (S/N) ratio that can be calculated using collected spectra:[104,105]

$$S/N \propto n\gamma_e T^{-1}\sqrt{(\gamma_d{}^3 B_0{}^3 t)} \cdot f_{CP} \cdot \eta \sqrt{VQ} \qquad (1)$$

Better S/N ratios can be obtained by packing more sample or isotopically labeling the material to increase the number of spins (n), elongating the experimental time (t) to collect more scans if the interscan delay time (recycle delays) is fixed, lowering the temperature (T), measuring the sample on a larger magnet with higher field strength (B_0), optimizing the ^{1}H−^{13}C cross-polarization efficiency (f_{CP}), and building better probes with optimized parameters for coil filling (η), coil volume (V), and coil quality (Q). The signal-to-noise ratio will be increased, ideally in proportion to the square root of the number of scans. Two additional factors are the gyromagnetic ratios of the excited (γ_e) and detected nucleus (γ_d), which inspired the development of many sensitivity-enhancing methods, including cross-polarization (CP) and DNP, to transfer polarization from the "more-sensitive" nuclei or even electrons to the "less-sensitive" nuclei.

We chose ^{13}C as the standard nucleus for ECM studies for its abundance, nontoxic enrichment, reasonable sensitivity, spin $^1/_2$ nature (Figure 3A), and, more importantly, its well-dispersed

chemical shifts. Chemical shifts (δ) are sensitive indicators of chemical environments and are typically reported in parts per million (ppm), as defined by

$$\delta = 10^6\left(\frac{\omega_{obs} - \omega_{ref}}{\omega_{ref}}\right) \qquad (2)$$

where the differences of observed and reference frequencies are normalized by the reference frequency after considering a 10^6 factor. The reference frequency can be obtained using the standard resonance frequency of nuclei in a standard compound such as tetramethylsilane (TMS; most used for ECM studies) and sodium trimethylsilylpropanesulfonate (DSS; more applicable to protein research). Resonance frequencies of given nuclei slightly vary depending on the local chemical environments, resulting in resolvable peaks in an NMR spectrum. The smaller and larger chemical shifts are sometimes described as "upfield" (or more shielded) and "downfield" (or less shielded), respectively. These terms describe the effective field experienced by a nucleus, which has been reduced (shielded) or increased (deshielded) by the additional magnetic field created by the surrounding electrons when compared to a reference compound.

To rapidly screen a large collection of cells and ECM materials, one-dimensional ^{13}C spectra are typically measured
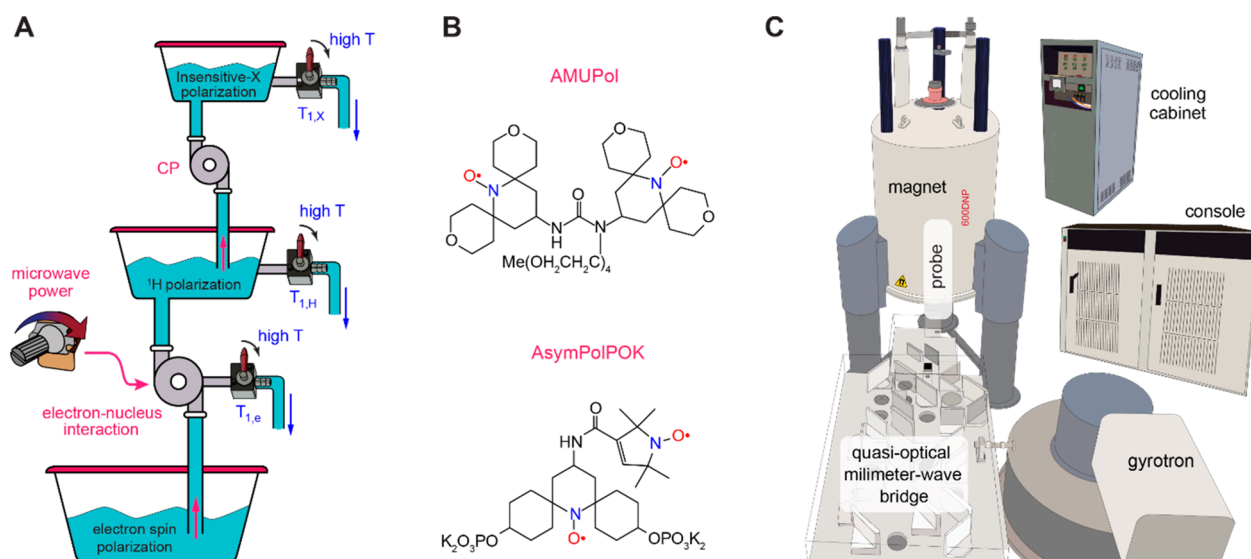
Figure 5. Mechanism, radical, and instrumentation of MAS-DNP. (A) Scheme simplifying the DNP process. The microwave irradiation enables the transfer of electron spin polarization to the protons via the electron−nucleus interaction, and the proton polarization is then transferred to the less sensitive X nuclei via CP. The proton polarization level depends on the nuclear and electron relaxation times $T_{1,H}$ and $T_{1,e}$. Short $T_{1,e}$ prevents efficient polarization transfer, while short $T_{1,H}$ reduces the ability of protons to retain polarization. (B) Examples of biradicals used for ECM characterizations.[170,171] (C) The MAS-DNP setup at the National High Magnetic Field Laboratory, USA. The microwave irradiation is generated by a second harmonic gyrotron emitting a Gaussian beam at 395 GHz. The beam's power, polarization, and gating are controlled by a quasi-optical bridge and directed toward the probe in the NMR magnet where the sample is irradiated and spun at 3−15 kHz, as regulated by the console. Cooling to ~100 K is achieved using a dedicated cooling cabinet.[172]

using different ways of creating the initial magnetization (Figure 4A,B).[80] *J*-coupling-mediated ^1H−^{13}C INEPT spectra are commonly used to select the highly dynamic polymers and largely solvated molecules.[106] Direct polarization (DP) of ^{13}C can either give quantitative detection of all carbons by using sufficiently long recycle delays (the interscan delay) or provide selective detection of mobile molecules by using short recycle delays. For a carbon site, a long recycle delay set equivalent to 4−5 times of its ^{13}C spin−lattice (T_1) relaxation time constants can efficiently detect 98.2−99.3% of the carbons (thus giving quantitative detection), while a short recycle delay of a quarter of the ^{13}C−T_1 can only detect 22% of the signal (thus being suppressed and filtered). The dipolar-mediated ^1H−^{13}C CP preferentially detects the rigid molecules with stronger ^1H−^{13}C dipolar coupling or the chemical motifs with higher proton densities.[107] A MultiCP method has been developed recently to provide quantitative detection through repetitive ^1H−^{13}C cross-polarization and ^1H repolarization steps, providing a time-efficient replacement for ^{13}C-DP experiment.[108,109] These 1D ^{13}C experiments are frequently used to assess the characteristics of the dynamically heterogeneous ECM or cellular materials to guide the design of more sophisticated experiments.

Multidimensional (typically 2D or 3D) correlation spectra are often required for adequately resolving the large number of chemically different biomolecules and their variable conformational structures in a cellular system. The conventional 2D ^{13}C−^{13}C correlation experiments in solids could be grouped into five categories depending on the mechanisms used for ^{13}C−^{13}C polarization transfer (Figure 4C,D): (i) *J*-coupling based experiments that enable through-bond polarization transfer such as the J-INADEQUATE experiment,[110−113] (ii) direct recoupling of ^{13}C−^{13}C homonuclear dipolar couplings using recoupling blocks such as RFDR or symmetry-based sequences,[114−116] (iii) assisting ^{13}C−^{13}C spin diffusion by either passively (without recoupling pulses, for example, PDSD) or

actively (with recoupling pulses, for example, DARR, CORD, and PARIS) recoupling the ^{13}C−^1H dipolar couplings,[117−119] (iv) ^1H−^1H spin diffusion preceded and followed by ^{13}C−^1H and ^1H−^{13}C heteronuclear polarization transfer, such as CHHC,[120,121] and (v) recently developed third-spin assisted recoupling (TSAR) schemes such as PAR.[122−124]

The introduction of more dimensions provides additional resolution and enables structurally enlightening methods by engineering the polarization transfer pathway. A straightforward way is to combine 2D sequences with different polarization blocks (INEPT, CP, DP, etc.) to distinguish components with different mobilities. Spectral editing methods can be applied to select molecules based on their chemical structures or dynamics. Examples include the selection of aromatics or non-protonated carbons through dipolar-gated sequences, the suppression of signals from rigid components via relaxation filters, the highlight of nitrogenated carbohydrates against other glycans using their ^{15}N−^{13}C dipolar couplings, and the detection of hydrated molecules using water-edited experiments.[125−128] In addition, the homonuclear spatial proximities (e.g., ^{13}C−^{13}C and ^1H−^1H) probed using 2D correlation experiments and the heteronuclear distances (e.g., ^{13}C−^{19}F and ^{13}C−^{15}N) determined by Rotational-Echo DOuble-Resonance (REDOR) provide structural restraints for understanding intermolecular packing.[129]

NMR is a powerful tool for investigating the dynamics of biomolecules, which can be correlated to their structural roles. For example, ECM polymers are often found to form rigid scaffolds or are distributed in soft matrixes as observed in plant and fungal cell walls.[16,130−132] The dynamical characteristics of polymers can be studied using a variety of relaxation experiments that probe motions on different time scales, as well as measurements of dipolar couplings and chemical shift anisotropy.[133,134] It should be noted that there is still a missing connection between the mechanical compliance of ECM

materials and the molecular dynamics of polymers measured by NMR, which requires further investigations.[61]

Non-uniform sampling (NUS) acquisition methods have been introduced to reduce the experimental time by skipping a fraction of the data that can be deduced or extrapolated from the rest of the experiment.[135] In general, NUS refers to any pattern of data acquisition that is performed at irregular time intervals or with variable numbers of transients taken at different time points.[136] NUS has become a standard approach in solution NMR and emerges as a frontier of ssNMR.[137−139] Studies of ECM and cells present promising future NUS applications. Paramagnetic relaxation enhancement (PRE) is another important method that has been employed for the structure determination of proteins[140−143] and recently applied to carbohydrate and ECMs.[144,145] PRE substantially extends the reach of distance measurement (to 10−35 Å);[146] therefore, it is uniquely capable of providing long-distance restraints that are important to the structure determination of large biomolecular systems.

The ssNMR versatile toolbox can serve a variety of purposes, from resonance assignment to investigations of polymer dynamics, water association, and supramolecular organization.[147] Methodological advances in ^{1}H detection,[148,149] sensitivity-enhancing MAS-DNP,[147,150−153] and ultrahigh-field magnets (1.0−1.5 GHz)[154−157] have further extended the technical capability of ssNMR.

2.2. Sensitivity-Enhancing MAS-DNP as an Emerging Technique

At natural isotopic abundance, ^{13}C represents only ∼1.1% of all the carbon atoms. To measure a 2D ^{13}C−^{13}C correlation, the first ^{13}C nucleus must be neighbored with another ^{13}C nucleus, meaning that only 1.1% × 1.1% or ∼1/10,000 of carbon pairs can generate a correlation. To overcome this sensitivity limitation, a solution is to "hyperpolarize" the nuclear spins. The most common approach nowadays is MAS-DNP,[21,158] which consists of doping the sample with a polarizing agent (PA), a molecule with unpaired electron spins, and then cooling and spinning the sample while irradiating with an appropriate microwave frequency. The gyromagnetic ratio of the unpaired electron spins leads to a polarization that is theoretically ∼658 times greater than the ^{1}H's and ∼2600-fold greater than ^{13}C polarization under identical experimental conditions. Typically, the electron spin resonant frequencies are in the hundreds of GHz.

This large electron polarization can be transferred to the surrounding nuclei by applying appropriate microwave irradiation that depends on the PA's structure.[147] The nature of the transfer, at the quantum level, can be classified as solid effect (SE), cross effect (CE), thermal mixing, or Overhauser effect.[21,151,159−169] The type of active mechanism depends on the PA's nature, its concentration, the magnetic field, the microwave power, and the temperature.

A naive analogy to explain the SE DNP process is illustrated in Figure 5A using buckets, pumps, valves, and liquid. The polarization (liquid) of the electron spin is pumped up toward the proton bucket under microwave irradiation. In the SE mechanism, the microwave drives a forbidden electron−nuclei transition that enables the transfer of polarization from the electron spin toward the protons. The stronger the microwave, the faster the transfer; however, a short electron longitudinal relaxation $T_{1,e}$ plays against this transfer by preventing the polarization from being transferred efficiently. Once transferred

to the proton bucket, the polarization can subsequently be transferred to an X nucleus (e.g., ^{13}C or ^{15}N) via CP, for example. In both cases, the ^{1}H and X nucleus buckets can leak polarization via their corresponding longitudinal relaxation mechanisms $T_{1,H}$ and $T_{1,X}$, respectively. The analogy clarifies the role of the relaxation times: $T_{1,e}$ and $T_{1,H}$ must be long to favor a high level of hyperpolarization. This is often the case when the sample temperature is lowered.

The analogy has its limitation: infinite microwave does not lead to infinitely fast or infinitely high polarization transfer, as the hyperpolarization plateaus beyond a certain microwave power. In addition, the polarization of the electrons, protons, and X spin systems is in constant equilibrium processes with their environment. This means that the electron spin polarization is repopulated at a rate proportional to $1/T_{1,e}$, which was omitted to keep the analogy more accessible.

For MAS-DNP, CE is the most used mechanism, while the Overhauser effect is anecdotal[166,173−175] and thermal mixing under MAS has not been demonstrated. The CE generates a high degree of ^{1}H polarization in a very short amount of time, enabling high ^{13}C polarization and quick experiment repetitions for signal averaging and phase cycling. An accurate analogy for CE is harder to establish, but the general concepts shown in the SE analogy (Figure 5A) remain applicable: the microwave irradiation helps "activate" a transfer of polarization from electron spins to proton spins, and the relaxation times must be long enough to enable the mechanism and maintain significant nuclear polarization levels. More detailed explanations of the CE mechanism under MAS can be found in many recent articles.[169,176−185]

The CE is obtained when the PA possesses two interacting unpaired electron spins, and the span of their Larmor frequency must be greater than the Larmor frequency of the targeted nuclei. This is easily reached for bis-nitroxides that were the first biradicals designed to efficiently polarize ^{1}H.[186,187] These biradicals are dubbed "homo-biradicals", as they consist of the same electron spin species. AMUPol drawn in Figure 5B belongs to that category.[170] Another class called "hetero-biradicals" are made of different electron spin species, such as a nitroxide and a Trityl for TEMPTriPol,[188] and have been introduced more recently to overcome limitations at high magnetic fields. In general, these biradicals are dissolved in a glass-forming matrix, like the mixture of glycerol/water or DMSO/water, and the resulting solution is used to wet the sample of interest.

Since their early inception, these biradicals have been massively improved. Experimentalists and chemists have designed ever better performing biradicals by educated guess.[170,188−197] Their efforts illustrated the crucial role of biradicals' solubility, the molecular weights' impact on the electron spin relaxation times, and the importance of the coupling between the two electrons' spins. In parallel, theoretical analyses revealed how complex the mechanism of polarization transfer is under MAS, identified the parameters determining the polarization transfer efficiency, and revealed the rate at which it occurs.[166,171,176−178,180−182,184,198−202] Nowadays, theoretical models have reached the capability for the *in silico* design of efficient PAs, for instance, the AsymPolPOK (Figure 5B), and the prediction of nuclear hyperpolarization and buildup rate.[171,181]

Today's best biradicals deliver nuclear polarization levels that are ∼100 times greater than the thermal equilibrium,[171,178,181,198,199] with polarization transfer happening on

the time scale of seconds,[170,171,193,195,196] additionally offering massive time saving.

MAS-DNP requires special instrumentation, which consists of the NMR magnet and consoles, a dedicated probe, a powerful microwave source, an optional microwave control system, and a heat exchanger (Figure 5C). The microwave source is typically a gyrotron that generates powerful coherent microwave irradiation.[203−206] The cooling and spinning are carried out with cold nitrogen gas to secure a low sample temperature of ∼100 K, which enables long relaxation times of electron and nuclear spins for efficient MAS-DNP. The probe and rotor are designed to ensure that the microwave irradiation can reach the sample as well as enable MAS at low temperature.

MAS-DNP instrumentation has been improved since its commercialization. MAS-DNP spectrometers are commercially available for magnetic fields of 9.4 T/400 MHz/263 GHz and up to 21.1 T/900 MHz/590 GHz.[205−207] In recent years, probes using smaller rotors (0.7−1.9 mm) have been developed to join the originally commercialized 3.2 mm probes. High-resolution ^{1}H capabilities are now accessible thanks to the 0.7 mm rotors that can spin up to 65 kHz in an MAS-DNP instrument.[205,207,208] Smaller rotors seem to have additional benefits at high magnetic fields. Indeed, a drastic loss of hyperpolarization performance for bis-nitroxides in 3.2 mm rotors at high magnetic fields (>14.1 T) has been observed. This loss seems less pronounced for smaller rotors, which may indicate that high-field DNP is more sensitive to microwave absorption.[206,209] This has been circumvented by using hetero-biradicals which are optimal with weaker microwave power.[198]

Low temperatures make the spinning slower by ∼50% as compared to room temperature conditions,[205,206] limiting the resolution and pulse sequence library that can be used. To enable both higher nuclear hyperpolarization and faster spinning, closed-loop helium spinning systems have been recently developed.[210−216] Temperature reduction also lengthens relaxation times, therefore reducing the need for stronger microwave irradiation.[217,218] A closed-circuit helium system can reach dramatically lower temperatures, enabling these benefits. In addition, the speed of sound in He is much higher than that for N_2 and results in faster spinning at a given temperature.[210,211]

The low temperature required for MAS-DNP often leads to less-resolved spectra for more dynamic molecules. This is not the case for rigid carbohydrates, and the cell wall in general, as illustrated by recent work on ECMs,[82,219,220] and the sensitivity gains are sufficient to forego isotope sample enrichment altogether, as demonstrated recently on rice stems.[221,222] For complementary information on the topic, we refer the reader to other reviews.[21,151,158,167,223−226] In sum, experiments that were deemed impossible previously, such as natural-abundance ^{13}C−^{13}C correlation, can now be executed on a time scale of a few hours to a day.[27,227−231]

3. SOLID-STATE NMR STUDIES OF PLANT MATERIAL

3.1. Plant Cell Wall: A Heterogeneous Network of Biopolymers

Three classes of polysaccharides coexist in the plant cell wall, i.e., cellulose, hemicellulose, and pectin.[67,232] Cellulose microfibrils can be viewed as the stiff scaffold of the polymer network.[65] Synthesized by cellulose synthase (CesA) proteins in the plasma membrane using UDP-glucose substrates, 18 linear chains of β-(1,4)-glucose residues are held together by hydrogen bonds to

form a partially crystalline microfibril with a diameter of 3−5 nm.[233] As for hemicellulose, it is typically a branched polysaccharide with high diversity in monosaccharide composition and branching pattern.[234,235] Common hemicelluloses include xyloglucan, xylans, mixed-linkage glucan (MLG), and mannan (Figure 2). Many types of xylans and mannans are present with variable patterns of substitutions, including arabinoxylan (AX), glucuronoarabinoxylan (GAX), galactomannan, glucomannan, and galactoglucomannan (GGM). The structure of pectin is difficult to define, as it includes a large collection of sugar units, mainly uronic acids but also galactose, rhamnose, arabinose, and xylose.[236,237] Hence, no single technique can provide complete resolution or separation of all of these sugars. Pectin is perceived as an integrated matrix formed by covalently interconnected structural domains, including homogalacturonan (HG) and rhamnogalacturonan-I (RG-I), together with a low percentage of RG-II and proteoglycans.[238,239] Finally, lignin is an important non-carbohydrate polyphenolic component and is polymerized from monolignols through radical coupling reactions.[240−242]

Plants cells contain primary and secondary cell walls. The primary wall covers the outside of the membrane of a growing cell, and the secondary wall starts to accumulate once the growth has ceased. The extent of cellulose coalescence, namely, the bundling of elementary microfibrils, is significantly higher in the secondary cell wall, resulting in large bundles of up to tens of nanometers across.[243] The primary cell-wall hemicellulose is xyloglucan in dicots, such as *Arabidopsis thaliana*, but is made of GAX and MLG in grasses (a type of commelinid monocots), such as *Zea mays*.[244] In the secondary cell wall, xylan becomes the dominant form of hemicellulose, although mannan and mixed-linkage glucans are occasionally found in certain plants. While pectin is negligible in the secondary cell wall, it is abundant in the primary one. Pectin is also the major component of the middle lamella that joins adjacent cells together, and where the lignification occurs. From the middle lamella, lignification will progressively reach and dominate the secondary cell wall.[245] Its chemistry relies on three basic phenylpropanoid monomers, *p*-hydroxyphenyl (H), guaiacyl (G), and syringyl (S), differentiated by their number of methoxy groups (Figure 2). They are heterogeneously cross-linked to form a polymer network that strengthens and waterproofs the cell wall and increases biomass recalcitrance.[246,247]

It is a formidable challenge to understand the structural arrangement of a polymer composite as heterogeneous and complex as the cell wall using conventional analytical methods. Therefore, the following section will briefly summarize the past decades of ssNMR efforts in characterizing cellulose structure and then present the more recent breakthroughs in understanding polymer interactions using intact cell walls and whole-cell materials.

3.2. Structural Investigations of Cellulose

3.2.1. Cellulose: A Chemically Simple but Structurally Complex Polymer. The assembly and crystallization of cellulose microfibrils, as well as their coalescence into fibrils on a larger scale, are structurally stabilized by numerous intra- and intermolecular hydrogen bonds that chemically involve the hydroxide groups attached to C_2, C_3, and C_6 carbon sites of β-D-glucose units.[248] Crystalline cellulose found in nature was generally considered to be a mixture of two allomorphs,[249] Iα and Iβ, evidenced with distinct ^{13}C CP ssNMR spectra (Figure 6A).[250,251] In higher plants, the thermodynamically more stable
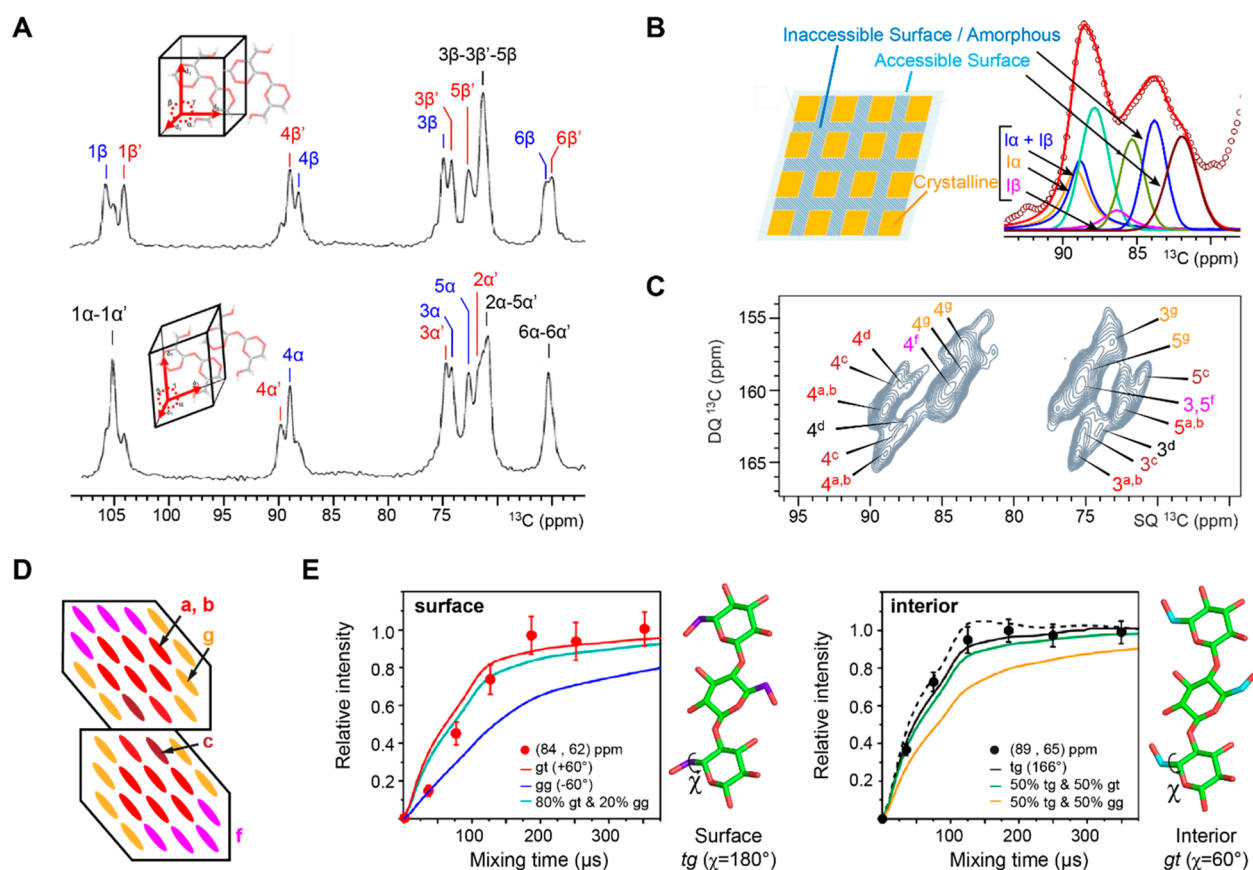
Figure 6. An evolving view of cellulose structure from ssNMR. (A) Reference ^{13}C spectra of two cellulose samples dominated by either Iβ (top) or Iα allomorphs (bottom). They both have two magnetically inequivalent carbon sites and the splitting of lines into doublets. Panel A is adapted with permission from refs 249 and 256. Copyright 2021 Elsevier and 2006 Springer Nature. (B) Core−shell model of cellulose fibrils with a crystalline interior enveloped by an amorphous inaccessible surface and then an accessible surface. Panel B is adapted with permission from refs 258 and 259. Copyrights 2020 Springer Nature and 2019 Elsevier. (C) 2D ^{13}C INADEQUATE spectrum (C$_4$−C$_{3/5}$ region) resolving a variety of glucose conformers (types a−g) in intact maize stems. Panel C is adapted with permission from ref 260. Copyright 2019 Springer Nature. (D) Scheme of two elementary microfibrils bundled together. Each microfibril has 18 glucan chains in a possible 2−3−4−4−3−2 hexagonal pattern. Bundling might lead to the embedded type c conformer.[260,261] (E) Hydroxymethyl conformation restrained by ^{1}H−^{1}H distance measurements. Interior cellulose and surface glucan chains feature different χ(O$_5$−C$_5$−C$_6$−O$_6$) torsion angles, as shown by the ^{1}H−^{1}H spin-diffusion curves obtained on the cellulose of intact *Brachypodium* primary cell walls. Panel E is adapted with permission from ref 262. Copyright 2018 American Chemical Society.

Iβ allomorph dominates, whereas Iα is preponderant in algae and bacteria. From diffractograms, it has been established that Iα has a one-chain triclinic unit cell (P1 space group), while Iβ has a two-chain monoclinic unit (P2$_1$ space group).[252−254] 2D ^{13}C−^{13}C ssNMR spectra fully resolved two magnetically inequivalent glucopyranose units in each of the two allomorphs: A and A′ units in Iα and B and B′ residues in Iβ.[255−257] Inter-residue cross peaks have been observed for A−A′, B−B, and B′−B′ linkages, which were estimated to be at least up to 3.6 Å due to the long recoupling time used to record 2D RFDR spectra.[256] Together, NMR and diffraction results have revealed that Iα has identical chains forming alternating A and A′ units, while Iβ has two types of chains arranged in alternating layers.[248]

In addition, ssNMR has been applied to distinguish multiple artificial crystalline forms, including cellulose-II irreversibly generated by cellulose-I mercerization (treatment with strong alkaline solutions) or regeneration procedures (solubilization and recrystallization) as well as metastable form III (obtained from evaporation of amines in an ammonia−cellulose complex) and form IV (following heat-treatment of cellulose III).[263−269]

Despite the well-defined crystallographic structures of model allomorphs, the structure of cellulose in the plant cell wall is not yet fully understood. For decades, a 36-chain model has been widely used to comprehend the organization of a microfibril, based on a hypothesized arrangement of cellulose synthase complex (CSC) as a hexamer of hexamer.[270,271] However, recent analyses of CSC and cellulose microfibrils support a hexamer of trimer organization where each elementary microfibril should contain 18 glucan chains.[272−275] Regarding the formation of larger fibrils, a simplistic model has proposed that the crystalline core may be wrapped by an outer amorphous layer (which can be either accessible or not), with the addition of an intermediate para-crystalline layer between the core and amorphous layers (Figure 6B).[276−278] This model was based on deconvolution procedures applied to the different C$_4$ signals and the paramagnetic relaxation enhancement (PRE) effect after adding 4-OH-TEMPO radical species, but the limited resolution could introduce significant uncertainty.[144,279]

Since 2016, the combination of 2D ^{13}C−^{13}C correlation spectra, isotopically enriched cell-wall samples, and high-field NMR magnets has provided unprecedented resolution and sensitivity for investigating cellulose structure. Four conceptual advances have thus been achieved. First, native cellulose microfibrils in intact plant cell walls are not a simple superposition of the Iα and Iβ allomorphs. Seven types of glucose units (types a−g) are resolved and consistently found in
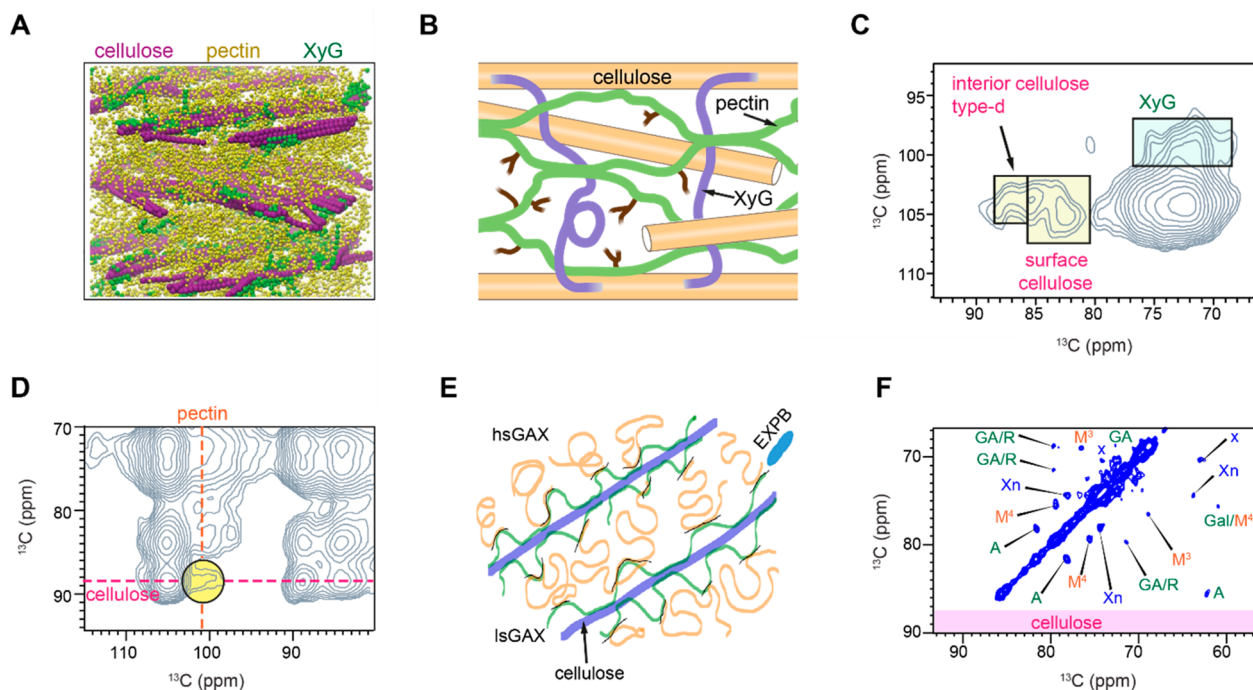
Figure 7. From macro- to microscale primary cell-wall models. (A) Coarse-grain model of the onion epidermal cell wall with multiple lamellae featured. Purple spheres represent cellulose, green for xyloglucan (XyG), and yellow for pectin. Panel A is adapted with permission from ref 292. Copyright 2021 The American Association for the Advancement of Science. (B) Scheme of primary cell walls with pectin−cellulose and XyG−cellulose interactions restrained by NMR data.[298] Panel B is adapted with permission from ref 298. Copyright 2021 Elsevier. (C) Expansin-bound region of carbohydrates viewed by MAS-DNP. In *Arabidopsis*, the protein-targeted molecules include XyG as well as the surface chain and interior type d chain of cellulose microfibrils. Panel C is adapted with permission from ref 297. Copyright 2013 United States National Academy of Sciences. (D) Representative pectin−cellulose ssNMR cross peak as highlighted using a yellow circle as observed in *Arabidopsis*. Panel D is adapted with permission from ref 299. Copyright 2015 Oxford University Press. (E) Model of β-expansin (EXPB) loosening the junctions between highly substituted GAX (hsGAX) and lowly substituted GAX (lsGAX). (F) A difference spectrum obtained from ^{13}C-labeled maize cell walls with and without paramagnetically tagged EXPB proteins. Only matrix polymers showed up and no cellulose signals were observed, revealing that EXPB does not bind cellulose. Panels E and F are adapted with permission from ref 145. Copyright 2016 Oxford University Press.

the 2D ^{13}C−^{13}C correlation spectra of a large variety of plant species (Figure 6C).[261,280] Their chemical shifts substantially deviate from those determined with highly crystalline and purified model cellulose samples. Second, the spatial organization of plant cellulose is more sophisticated than the crystallographic structures. These seven types of glucose units coexist in cellulose microfibrils (Figure 6D), with residues residing on the surface (types f and g), underneath the surface (types a and b), embedded in the core (type c), and on the interaction site with hemicellulose (type d). An increase in the number of embedded chains (type c) has been observed from primary to secondary cell-wall samples,[281] likely due to the enhanced coalescence of microfibrils, but we still lack a way to correlate it with microscopic observation for quantitatively assessing the organization of cellulose microfibrils in a large bundle, namely, the macrofibrils. Third, the surface and internal residues, which are important for the stability of the hydrogen-bonding network and the chemical reactivity of cellulose, were found to adapt *gauche−trans* (*gt*) and *trans−gauche* (*tg*) conformations, respectively (Figure 6E).[262] The hydroxymethyl conformation is restrained by $^1H_4$−$^1H_6$ distances. Fourth, the existence of Iα and Iβ structures was confirmed but only in the fibrils with large crystallites. Natural-abundance ^{13}C−^{13}C correlation DNP spectra collected on cotton cellulose have revealed chemical shift data that agree with the literature values collected on these model allomorphs.[281] These findings have exposed the unexpected complexity of cellulose. The improved spectroscopic resolution and sensitivity provided by the current

NMR technologies allow us to pursue many unresolved aspects of the microfibrils and macrofibrils.

3.2.2. Degree of Crystallization: A Well-Defined Parameter? The structural trait of cellulosic material is often presented by its degree of crystallization, also denoted as crystallinity index (CrI).[282−284] This key parameter can be correlated with the mechanical and structural properties as well as the chemical and enzymatical reactivity of cellulose.[285] Amorphous and crystalline phases coexist in cellulose, but their spatial organization is still debated, as they might be distributed longitudinally along the fibril axis or form the disordered surface and ordered core in the cross section of a fibril. ^{13}C ssNMR has provided a robust and efficient method to determine the CrI, which relies on either direct integration or spectral deconvolution of the C_4 chemical shift region, followed by calculating the ratio of intensities from the crystalline domain against the amorphous component. Spectral deconvolution partially alleviates the peak overlap issue; thus, it is considered to be more accurate than direct peak integration.[259,283] A recent protocol of CrI determination also includes the use of ^{13}C T_1 filters for differentiating amorphous and crystalline sites in cellulose.[285,286] Furthermore, by assuming a cross-sectional distribution of these phases, the NMR-measured CrI value can be converted to a surface-to-interior ratio that can be extrapolated to the fibril diameter or the number of glucan chains enclosed in a microfibril.[287−289] These straightforward protocols are well illustrated in the studies of cellulosic materials from different sources and processed with different procedures,
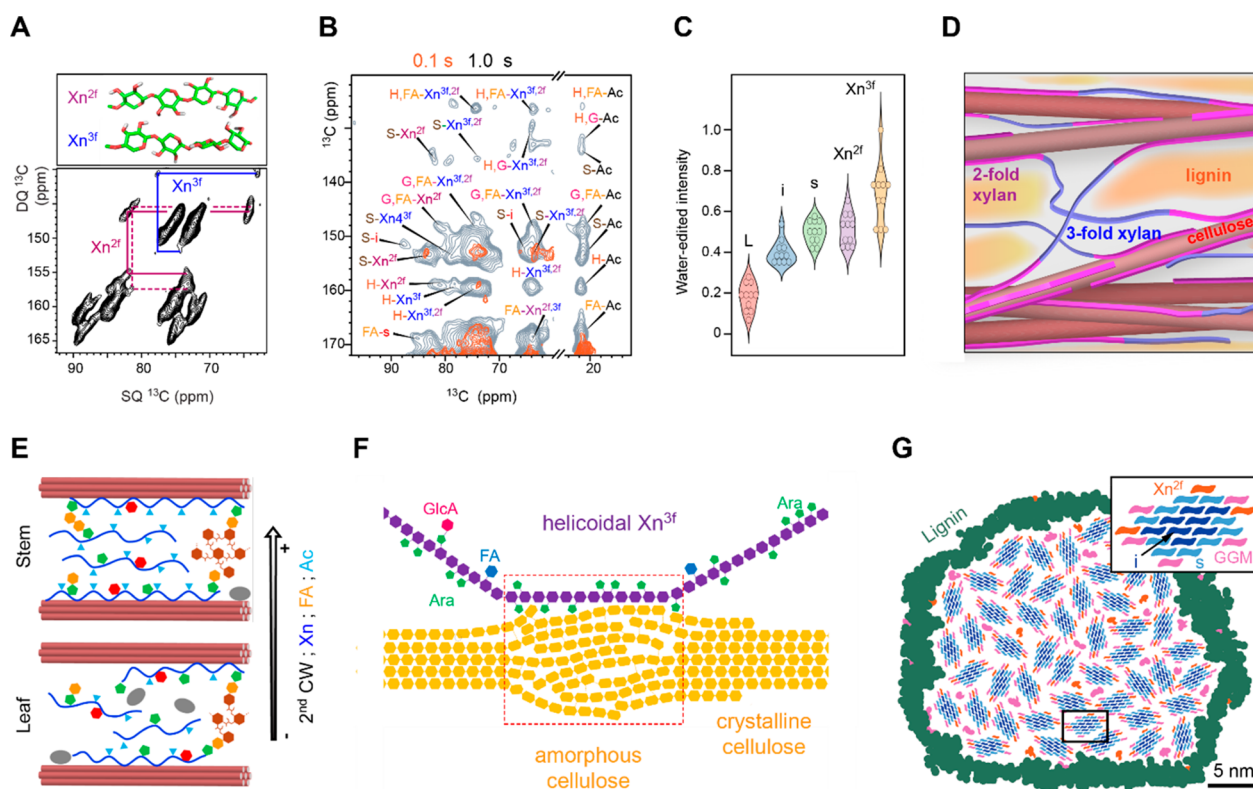
Figure 8. Polymer structure and interactions in secondary plant cell walls. (A) ^{13}C CP INADEQUATE spectrum of the maize stem resolving 2-fold (Xn^{2f}) and 3-fold (Xn^{3f}) xylan domains. (B) Intermolecular contacts between lignin units (H, S, G, and ferulate FA) and polysaccharides (xylan and cellulose) in maize. The overlay of dipolar-gated PDSD spectra collected using short (0.1 s) and long (1.0 s) mixing times showed numerous lignin—carbohydrate cross peaks. Abbreviations were also used for the internal (i) and surface (s) glucan chains and the acetyl group of xylan (Ac). (C) Polymer hydration level revealed by water-edited NMR intensities presented using violin plots. Lignin (L) has the lowest level of water retention in maize secondary cell walls. (D) Proposed model of secondary cell walls based on high-resolution ssNMR data collected using maize stems. Panels A, B, C, and D are adapted with permission from ref 260. Copyright 2019 Springer Nature. (E) Comparative models of *Brachypodium* stem and leaf secondary cell walls. A higher proportion of xylan functional groups (ferulic acid, FA, and acetyl, Ac) promotes its 2-fold conformation and contacts with cellulose fibrils. Panel E is adapted with permission from ref 306. Copyright 2021 American Chemical Society. (F) Limited interactions between 3-fold xylan and amorphous cellulose in *Sorghum* secondary cell walls. Panel F is adapted with permission from ref 307. Copyright 2020 Springer Nature. (G) A microfibril of spruce softwood formed by many 18-chain cellulose microfibrils and other associated molecules including GGM, xylan, and lignin. Panel G is adapted with permission from ref 308. Copyright 2019 Springer Nature.

for example, ball-milling, solvent treatment, and mutants for higher digestibility.[258,287,290]

Unfortunately, it is impossible to align the CrI values measured using ssNMR and other experimental methods such as X-ray diffraction, Fourier-transform infrared (FTIR), Raman, and vibrational sum frequency generation (SFG) spectroscopy.[291] Indeed, a single CrI value for a cellulosic sample cannot be provided due to the difference in the chemical motifs and physical arrangements being examined by different methods, which has recently been discussed using data collected on cotton cellulose.[255] We must better understand the connection between NMR chemical shifts and cellulose structure in order to precisely evaluate the crystallinity of cellulosic materials.

3.3. Interactions between Cellulose and Matrix Polysaccharides in Primary Cell Walls

As mentioned before, matrix polysaccharides include hemicellulose and pectin corresponding to the acidic polymers in the mobile gel-like matrix that can be extracted from primary cell walls by alkali treatments. Hemicellulose and pectin are produced in the Golgi apparatus and then secreted through the plasma membrane to the cell wall via vesicles.[236,237] This process happens concomitantly to cellulose synthesis and assembly, which might have contributed to the association of

matrix polysaccharides to cellulose by surface deposition or chain entrapment. Hemicellulose was long thought to cross-link multiple cellulose microfibrils and thus assumed a central role in load-bearing, while pectin was typically considered as phase-separated from the cellulose—hemicellulose network.[244] Our understanding of these polymers' interactions and their contributions to cell-wall mechanical properties has been revised following recent biophysical and biochemical studies.[232]

In 2021, a groundbreaking study of primary cell walls using mesoscale coarse-grained molecular dynamics (CGMD) simulations (Figure 7A)[292] allowed the establishment of a nanoscale-to-mesoscale correlation for the polymer assembly.[293,294] Demonstrated on onion epidermal cell walls, this work showed that tensile forces are mostly transmitted by cellulose microfibrils through sliding between microfibrils, thus contributing to the irreversible extension and regulating the plastic deformation of the cell walls. The role of hemicellulose and pectin in the cell-wall mechanical properties was proposed to be indirect, primarily by influencing the arrangement of cellulose microfibrils in the networks and affecting the accessibility of cellulose-modifying proteins. This latest model incorporates some key conceptual contributions from ssNMR studies, as will be briefly discussed below.

By applying ssNMR, the hemicellulose xyloglucan (XyG) was found to interact with cellulose at specific regions (Figure 7B), based on the limited XyG−cellulose cross peaks observed in a 3D ^{13}C correlation spectrum of *Arabidopsis* seedling cell walls—the first high-resolution ssNMR data set collected on intact primary cell-wall material.[295] This finding was supported by subsequent biomechanical studies[61,296] and field emission scanning electron microscope (FESEM) observations.[294] The "biomechanical hotspots" of *Arabidopsis* primary cell walls, where xyloglucan is entrapped in the type d conformer of cellulose, were also found to be the binding target of a wall-loosening protein named expansin (Figure 7C).[261,297] This result is in agreement with the equilibrated CGMD model, in which XyG exists as either an extended chain or a locally clustered coil and is attached to cellulose microfibrils with very limited sites of contacts.[292]

Unexpectedly, many intense cross peaks have been observed between cellulose and pectin, more specifically, with the galacturonic acid (GalA) and rhamnose (Rha) residues that form HG and RG-I backbones (Figure 7D).[298−300] A quarter to half of the cellulose surface was estimated to be spatially proximal to pectic polymers based on the spin-diffusion buildup data.[300] Pectin−cellulose contacts were consistently observed in a large number of wild-type and mutant *Arabidopsis* samples and fully retained even when bulk portions of HG were extracted from the cell wall.[130,298,299,301−304] This suggests that some pectic backbones are physically entrapped between glucan chains in a cellulose microfibril or sandwiched between multiple microfibrils when they are being assembled and bundled in the cell wall. Notably, in a study of *Arabidopsis* inflorescence stems, pectic polymers in the top segments were found to have more branched structure, reduced interactions with cellulose, and increased molecular mobility (probed by measuring $^{13}C−^{1}H$ dipolar couplings) than in the bottom segments.[130] These NMR results are in good agreement with the observed apical-to-basal decrease in elongation rate as well as elastic and plastic compliances. This notable advance presents an effort to correlate the molecular-level structure and dynamics of polymers with the mechanical properties of cell walls and the plant growth.

The primary cell wall of grass (a commelinid monocot) has also been investigated. In *Brachypodium*, the major hemicellulose, glucuronoarabinoxylan (GAX), was shown to be partitioned into two dynamically distinct domains, as revealed by their different $^{13}C−T_1$ and $^{1}H−T_{1\rho}$ relaxation parameters.[305] The rigid domain is interacting with cellulose, while the mobile region may be filling the interfibrillar space. In a study of maize primary cell walls, the junctions between highly and weakly substituted GAX were identified as the binding target of β-expansins that are native to the grasses (Figure 7E). This study used extracted expansin proteins from the grass pollen that have been bound to paramagnetic Mn(II) tags to examine the transverse PRE effect on the carbohydrate signals in grass cell walls (Figure 7F).[145] The PRE method, together with the differential labeling and DNP approach, demonstrated its usefulness in the examination of the binding targets of many other proteins or enzymes containing carbohydrate-binding modules (CBM). The roles of other matrix polysaccharides, such as mixed-linkage glucan and pectin in grasses, were not evaluated using these simplistic model samples and require further investigation.

3.4. Polymer Contacts in Secondary Cell Walls

Recent efforts have been progressively shifted to the understanding of the spatial organization of cellulose, hemicellulose, and lignin in secondary plant cell walls. The first breakthrough is the identification of the conformational selectivity of xylan.[309,310] Complemented by density-functional-theory (DFT) calculation, the NMR-observed peak multiplicity was associated with the conformational heterogeneity of this hemicellulose.[309] As illustrated in Figure 8A for maize stem, two sets of xylan cross peaks could be identified, i.e., 2-fold xylan (Xn^{2f}) and 3-fold xylan (Xn^{3f}), with a 360° helical rotation occurring every two or three xylose units, respectively.[260] Xn^{2f} has a flat ribbon structure, while Xn^{3f} has a helical shape and is the one observed in solution and presumably in the more disordered matrix of the secondary cell walls. In the vicinity of cellulose, mutual interaction leads xylan to adapt a 2-fold conformation to match the conformation of cellulose—a form that is abolished in a cellulose-deficient mutant.[307] Quantification of adsorbed xylan on birch pulp kraft has validated the conformational selectivity of xylan in the presence of cellulose and demonstrated its reversibility after xylan removal or readsorption.[311]

Xylan also interacts with lignin, primarily through its 3-fold conformation. This is evidenced with maize stems by the xylan−lignin cross peaks observed in a set of spectral editing experiments that selectively detect signals of aromatic molecules and their associated components (Figure 8B).[16,260,312] Xylan−lignin interactions would occur through surface contacts between different polymer domains as each type of molecule efficiently retained its unique hydration and dynamics (Figure 8C). Altogether, these results led to a structural scheme of secondary cell walls where xylan uses its 2-fold and 3-fold conformations to respectively bridge the cellulose surface and lignin nanodomains (Figure 8D).[260]

The conformational dependence of xylan's function was also confirmed in a recent study on 7-week-old *Brachypodium* (a model grass).[306] The structure and interactions of xylans were compared between the leaves and the stems, with the latter containing more secondary cell walls. Xylan chains were found to have twice as much acetylation and 60% more ferulation in the stems than in the leaves. Also, a high content of 2-fold xylan was observed in the stems, as well as more extensive xylan−cellulose interactions (Figure 8E). Surprisingly, a ssNMR study of the grass species *Sorghum bicolor* revealed a unique and weak interaction between 3-fold xylan and cellulose. This grass sample lacks 2-fold xylan and relies on the 3-fold conformers to interact with cellulose, likely at the amorphous region of the microfibrils (Figure 8F).[307] A recent study on softwood conifer secondary cell walls further reports that galactoglucomannan (GGM), the major hemicellulose of softwood, binds the surface of cellulose microfibrils in a semicrystalline manner, with lignin in association with the cellulose-bound polysaccharides (Figure 8G).[308,313] In addition, the physical and mechanical properties of hemicellulose have been assessed by incorporating extracted softwood or hardwood hemicellulose into bacterial cellulose hydrogels to closely imitate plant secondary cell walls before lignification.[314] Despite these major advances, many structural aspects of the secondary cell walls, such as cellulose−lignin contacts and the covalent and physical interactions regulating polymer associations, still require in-depth investigations by ssNMR methods.

M
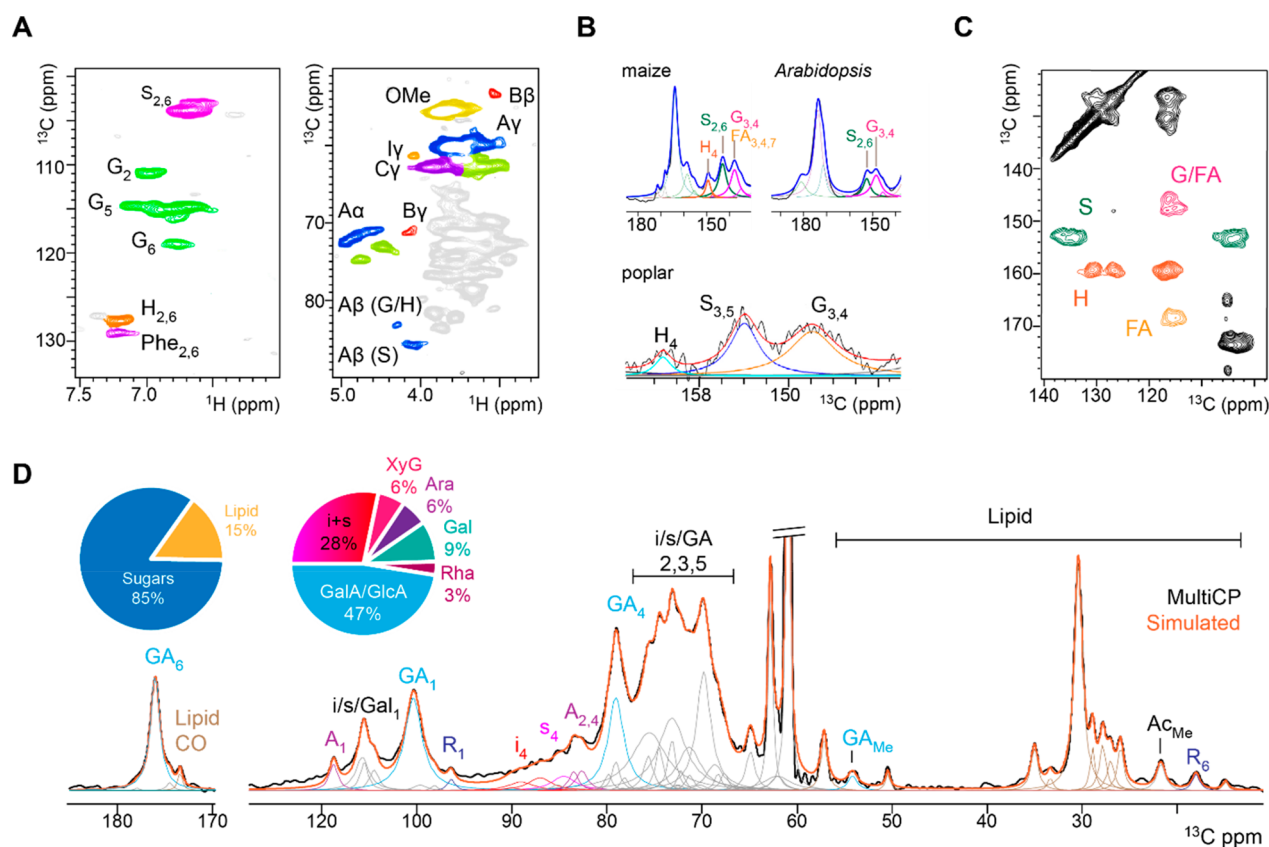
Figure 9. Difficulty of lignin ssNMR and compositional analysis. (A) Representative solution-state HSQC spectra with a high resolution of both monolignol units and linkages for poplar wood.[316] Panel A is adapted with permission from ref 316. Copyright 2020 American Chemical Society. (B) Representative 1D ^{13}C ssNMR spectra of various plants showing broad lignin signals. Panel B is adapted with permission from refs 260 and 327. Copyrights 2019 Springer Nature and 2020 Elsevier. (C) 2D ^{13}C ssNMR resolving the signals of lignin units. Panel C is adapted with permission from ref 260. Copyright 2019 Springer Nature. (D) Quantitative MultiCP spectrum of onion cell walls reconstructed from 59 deconvoluted peaks. Sugar-to-lipid ratio and carbohydrate composition are obtained but with considerable uncertainty. Panel D is adapted with permission from ref 331. Copyright 2021 Springer Nature.

3.5. Limitations and Perspectives of Solid-State NMR in Plant Research

3.5.1. Lignin Structure and Lignified Cell Walls.
Lignin is commonly found in the secondary cell walls of certain specialized plant cells, where it confers high rigidity and resistance to microbial degradation.[315] There is a paradox between the simplicity of monolignol basic units and the complexity of the polymerized network, which is a result of the variety of linkages present in lignin.[240,316] Solution NMR is the most employed analytical technique to characterize lignin (Figure 9A),[14,15,317,318] and only a few ssNMR experiments have been carried out to investigate the lignin structure. 1D ssNMR approaches have been used to determine how well lignin fractions were solubilized prior to solution NMR measurements and to avoid the chemically destructive acidic hydrolysis methods (like Klason lignin analysis) for quantification.[319–324] Efforts have also been made to estimate the ratio between the G and S units in poplar and other woody plants,[325–327] but insufficient resolution prevents accurate determination of the concentration of individual lignin units and linkage patterns.[328] In addition, all deconvolution procedures applied in the spectral analysis are affected by considerable uncertainty, especially when broad peaks overlap (Figure 9B). Lignin units can be better resolved in 2D [13]C–[13]C correlation spectra (Figure 9C).[260,324] DNP has also been applied to wild-type and mutant poplar samples to unravel the structural changes of lignin, and

the resolution enabled distinguishing the three types of fundamental units and partially probing their linkages.[329] More efforts are needed to improve the ssNMR capability for lignin structure characterization to par with solution NMR methods, with the additional merit of using native samples free of chemical treatment, ball-milling (which restructures biomolecules, as shown recently[281]), and solubilization procedures. The covalent linkers bridging monolignol units and the putative lignin−carbohydrate complex[313,330] are also of special interest for ssNMR investigations.

3.5.2. Quantification of Cell-Wall Composition.
To account for the diversity of plant species, their evolving traits during growth, and the development of genetically modified organisms, statistical analysis approaches, more commonly undertaken in metabolomics and ^{1}H HR-MAS studies of natural products, begin to extend to ssNMR research of lignocellulose. For example, such strategies have been applied to monitor water deficiency effects in order to better understand drought stress on plants.[332] Unfortunately, ssNMR lacks the time efficiency to survey a large number of samples—a mandatory step to match the success of metabolomics in solution NMR.[333,334]

Since NMR resolves differences in chemical environments, changes that occur on biomaterials after they are subjected to any form of exterior physical or chemical perturbation can be easily detected using well-established chemical shifts,[335–337] with the assistance of an online chemical shift database.[338]
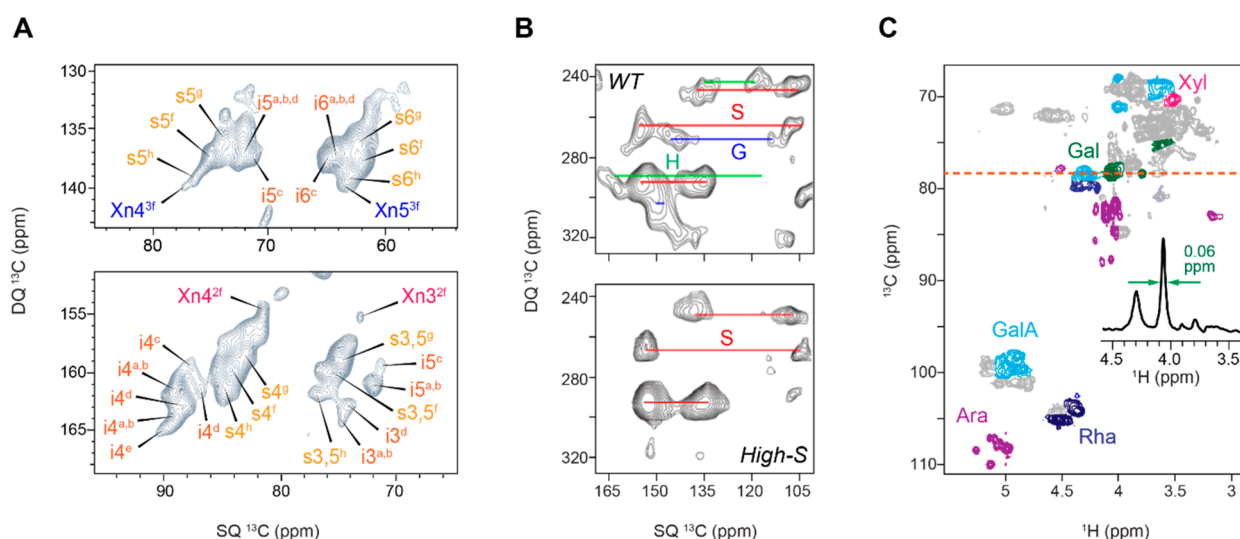
Figure 10. Natural-abundance MAS-DNP spectra and ^1H detection of plant cell walls. (A) Refocused-INADEQUATE spectra and assignment of polysaccharides and their conformers using unlabeled rice stems taken from the field.[221] The resolved carbohydrates include the 2-fold (Xn^{2f}) and 3-fold (Xn^{3f}) xylan and the many types of glucose units from surface (s) and interior (i) chains of cellulose. The top panel represents the non-reducing carbon (C_6/C_5 for cellulose/xylan, respectively) directly linked to the central carbon (C_5/C_4 for cellulose/xylan, respectively), while the bottom panel indicates the chemically similar central carbons. Panel A is adapted with permission from ref 221. Copyright 2021 Springer Nature. (B) Refocused-INADEQUATE spectrum of wild-type poplar and high-S mutant paving the way for assignment of lignin signals using unlabeled samples. Panel B is adapted with permission from ref 329. Copyright 2017 American Chemical Society. (C) Fast MAS (50 kHz) INEPT spectrum of ^{13}C-*Arabidopsis* primary cell walls resolving the signals of sugar units in the mobile matrix polysaccharides. The dashed line indicates the position of the ^1H cross section for highlighting the narrow line width. Panel C is adapted with permission from ref 89. Copyright 2019 Springer Nature.

Therefore, modifications of the plant cell-wall structure, composition, dynamical properties, and polymeric interactions during their development[130,302] or under external factors,[339] such as heat,[340] physical stress, enzymatic digestion,[259] chemical treatment,[341−343] or any combination of these, could be better understood.[339,344]

To bypass exceedingly long ^{13}C T_1 relaxation times, CP is preferred to DP, as it is well adapted for rigid cellulose and lignin, notably when internal references are used to quickly calibrate the polarization transfer efficiency between samples.[345] For example, celery is a model plant with two types of primary cell walls (parenchyma and collenchyma). This plant has been used in comparative NMR studies to elaborate 1D CP and DP methods for discriminating different sugars.[346−350] We recently delved into sugar quantification on a chemically similar system, i.e., the epidermal cell wall of onion, by combining quantitative Multi-CP spectrum and spectral deconvolution (Figure 9D).[331] The results were in relatively good agreement with chromatography techniques (±8% for major cellulose and homogalacturonan units and ±4% for minor sugars). However, quantifying the polymer composition in ECMs remains a challenging task.

3.5.3. Is Isotopic Labeling Still Mandatory? Multiple emerging approaches allow one to either entirely or partially alleviate the need for uniform isotopic enrichment using $^{13}CO_2$ or $^{13}C_6$-glucose.[86] The "natural-abundance DNP" approach[227,229,230] has been applied to a large variety of unlabeled plant samples. For example, MAS-DNP provided a 23-fold signal enhancement using cotton samples, with the line widths largely preserved (0.8−0.9 ppm) despite cryogenic temperature.[281] The 2D spectra assignment agreed with cellulose I references, but substantial modifications of cellulose structure by ball-milling procedures have been noticed. Recently, a DNP protocol for systematically investigating plant cell walls has been developed and demonstrated on the wild-type sample of *Oryza sativa* (rice) as well as a *ctl1 ctl2* double mutant showing

brittleness phenotypes.[221] A 22−57-fold signal enhancement allowed resolving different conformers of cellulose and xylan using unlabeled stems, with 2D INADEQUATE and CHHC spectra resembling those collected with classic ^{13}C-labeled samples (Figure 10A). The structural information provided by cryogenic temperature DNP (*circa* 100 K) was complemented by room-temperature natural-abundance relaxation measurements, revealing higher polysaccharide mobility in the mutant cell walls.[221] Since the samples used in this study were rice stems directly collected from the field, the toolbox is thus generally applicable to all lignocellulose materials.

Natural-abundance DNP has also been used to determine the extent of delignification in wood material subjected to pretreatment (lignin extraction)[351] and to analyze the monolignol units and linkages in wild-type poplar and a mutant with a high content of S-units (Figure 10B).[329] DNP has also been employed to characterize cellulose derivatives and understand the regioselectivity of cellulose methylation.[352] The DNP-enabled 2D $^{13}C−^{13}C$ INADEQUATE spectra of unlabeled cellulose derivatives provided sufficient resolution for identifying the methylation site. Alternatively, the unique mobility of CH_3 groups, which was retained at the DNP cryogenic temperature, was utilized to locate their closest neighbors in space, here cellulose C_3, by monitoring NOE polarization transfers.[352]

Another promising direction is the proton detection under ultrafast MAS. In 2019, a series of 2D and 3D $^1H−^{13}C$ correlation experiments were conducted on the model plant *Arabidopsis* under slow to moderately fast spinning frequencies (10−50 kHz).[89] With a ^1H line width of ~50 Hz (0.06 ppm on an 800 MHz spectrometer), resonance assignment has been successfully achieved for matrix polysaccharides (Figure 10C), and a good agreement was found between the ^1H chemical shifts of these mobile molecules measured in the solid and solution states. Long-range correlations between matrix polysaccharides
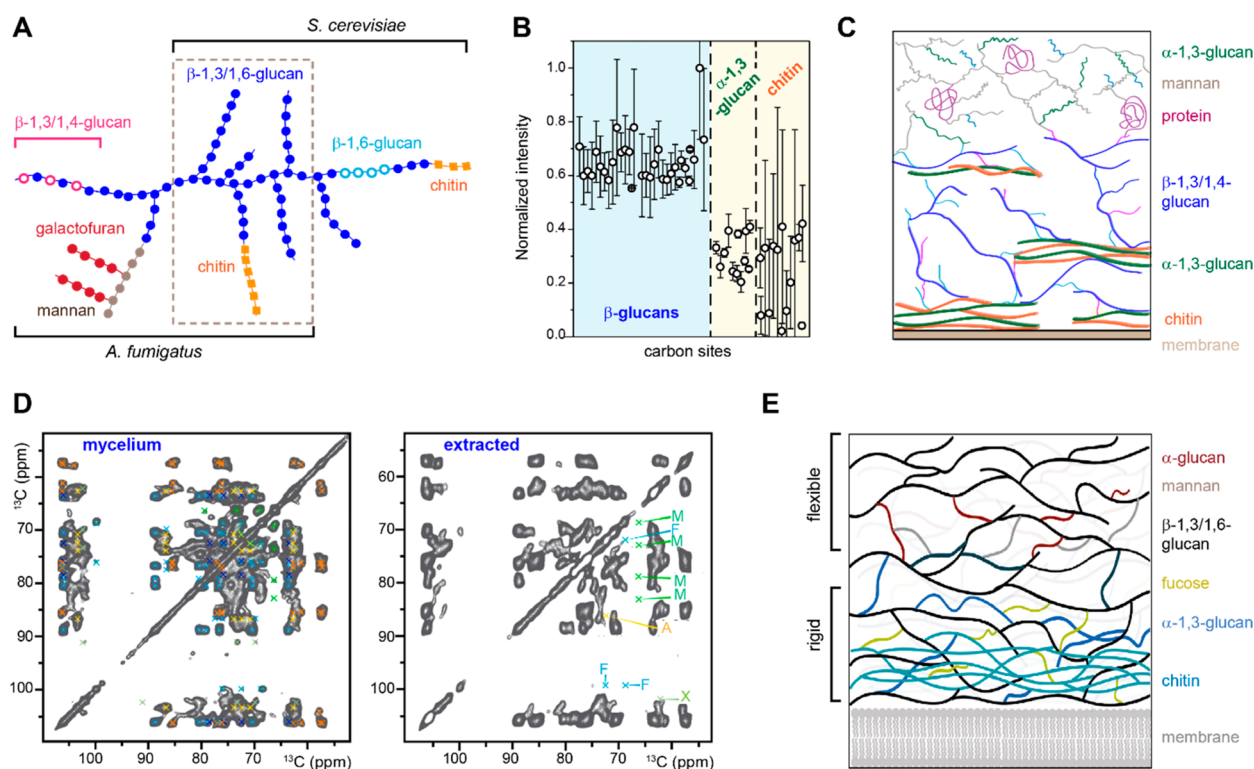
Figure 11. Fungal cell-wall architecture viewed by ssNMR. (A) Carbohydrate connectivity of the alkaline-insoluble core of fungal cell walls as reported using biochemical assays. The common module found in many fungal species is boxed using dashed lines. The structural features in *A. fumigatus* and *S. cerevisiae* are distinguished.[3] Panel A is adapted with permission from ref 3. Copyright 2007 John Wiley and Sons. (B) Water-edited intensity as an indicator of polymer hydration measured using *A. fumigatus* mycelium. For instance, chitin and *α*-1,3-glucan are poorly hydrated when compared to *β*-glucans. (C) Structural scheme proposed for *A. fumigatus*, emphasizing the packing between chitin and *α*-1,3-glucan to form the hydrophobic and rigid core. Panels B and C are adapted with permission from ref 49. Copyright 2018 Springer Nature. (D) 2D ^{13}C PARIS spectra collected on the hydrated mycelium of *S. commune* (left) and the same material after PBS washing, SDS extraction, and alkali extraction (right). Many carbohydrate components are missing after extractions. (E) Proposed model for cell walls in *S. commune* based on ssNMR combined with HPLC and GC−MS. Panels D and E are adapted with permission from ref 82. Copyright 2020 Elsevier.

and cellulose were also reported, based on ^{1}H−^{1}H spin diffusion instead of the more conventional ^{13}C−^{13}C polarization transfer. These experiments have been demonstrated using either ^{1}H or ^{13}C detection; however, it should be noted that the broad ^{1}H signals of cellulose are typically filtered out to ensure sufficient resolution, and cellulose is typically detected only using ^{13}C. Almost at the same time, another ^{1}H-detection study has been conducted on bacterial materials under 100 kHz MAS to investigate the structure of peptidoglycans.[88] The ^{1}H chemical shifts of polysaccharides reported by these studies certainly pave the way to investigate unlabeled plant materials exploiting the ^{1}H nucleus with high natural abundance (99.98%).

Another strategy worth mentioning is the selective or sparse labeling approach. It does not evade the demanding procedures involved in isotope labeling but can provide a way to tackle specific molecules of interest. For example, from ^{2}H-labeled UDP-glucose (precursor for cellulose synthesis) and ^{13}C-coniferin (a lignin precursor), cellulose and lignin have been tracked in the ginkgo tree to determine their mutual interactions and the linkages they form as well as follow where labeling occurs in newly formed xylem.[353] Selective labeling has also been coupled with ^{13}C{^{2}H} REDOR experiments to identify the tyrosine−tyrosine cross-linking occurring in plant cell walls and measure the strength of the associated dipolar coupling, whereas ^{13}C{^{15}N} REDOR enables exploring the steric hindrance from neighboring lysine peptides.[354]

At this stage, information on the polymorphic structure (with chemical shifts as a sensitive reporter of the linkages and conformations), dynamics, and hydration of polysaccharides can be efficiently obtained using unlabeled tissues.[221] Another structurally important aspect—intermolecular interactions—could possibly be addressed by the establishment of ^{1}H-detection techniques. Therefore, we expect a new era of research on unlabeled materials for addressing key biochemical questions related to ECMs. After sample optimization, each DNP-enhanced ^{13}C−^{13}C correlation spectrum can be recorded within tens of hours using unlabeled materials.[221] The experimental time, however, is still noticeably longer than the typical NMR experiment conducted on isotope-enriched samples. DNP and proton-detection approaches should primarily serve as enabling methods for samples that are either difficult to label or impractical to replicate. With constantly improving radicals and instrumentation, the combination of the natural-abundance MAS-DNP and ^{1}H-detection techniques and isotope labeling should substantially expand the ssNMR playground in biomolecular and biomaterial research.

4. RESOLVING THE MOLECULAR ARCHITECTURE OF FUNGAL CELL WALLS

4.1. Fungal Cell Wall as a Target for Drug Development

Fungi are a class of eukaryotic microorganisms widespread in nature where some of them cause invasive infections or systemic

diseases in humans.[5] *Candida*, *Aspergillus*, and *Cryptococcus* species are responsible for more than 1.6 million life-threatening infections annually, with 20−95% mortality.[355−362] Azoles and amphotericin B (AmB) are prevalent agents used in antifungal treatment, exhibiting a broad spectrum of activity against most clinically relevant unicellular non-sporous yeasts and multi-cellular sporous molds. These compounds either directly bind ergosterol molecules in fungal membranes or inhibit enzymes involved in the biosynthesis of ergosterol. Similarly, in human membranes, they can exhibit disadvantageous interactions with cholesterol and enzymes in human membranes, leading to severe side effects.[363−365] In addition, drug resistance has been growing significantly over the past decades.[357,364]

Since the fungal cell wall contains polysaccharides that are absent in human cells, significant attention has been devoted to the identification of antifungal compounds targeting fungal polysaccharides. Rewarding these efforts, a class of β-(1,3)-glucan synthase inhibitors named echinocandins have been clinically approved and are currently used to treat fungal infections.[366−368] Nevertheless, echinocandins have a limited spectrum of activities: these compounds have high efficacy against invasive candidiasis (infections caused by *Candida* species) but not for invasive aspergillosis, which is due to the adaptive mechanisms developed by *Aspergillus* species.[369−371] An in-depth understanding of the molecular organization of cell walls across fungal species and the structural effects from antifungal compounds could pave the way for developing wall-targeting drugs with higher efficacy and a broader spectrum of antifungal activities.

4.2. Incomplete Understanding of Fungal Cell-Wall Structure

The polymer composition of the fungal cell wall is highly heterogeneous, but chitin and β-glucans are two components commonly found in many species. Chitin is a highly elastic polymer of β-1,4-linked *N*-acetylglucosamine monomers (Figure 2), which can be stabilized through hydrogen bonds to form microfibrils.[372] Chitin accounts for 10−20% of the polysaccharides in *Aspergillus fumigatus* and *Candida albicans*[373,374] and becomes deacetylated chitosan in *Cryptococcus neoformans*. Glucans are the most abundant polysaccharides in fungal cell walls, accounting for 50−60% of the dry mass.[373] β-1,3-Glucans comprise 65−90% of all β-glucans in the cell walls, where their content varies from 25−30% in the filamentous fungus *Aspergillus fumigatus* to 50−55% in *Saccharomyces cerevisiae*.[373,375−377] β-1,6-Glucan is also important, with a proportion of 5−12% in *S. cerevisiae* cell walls and around 20% in *C. albicans* cell walls. There are no linear β-1,6- or β-1,4-glucans in *A. fumigatus*; however, branched β-1,3/1,6-glucans (with a β-1,6-linkage as the branching point) and linear β-1,3/1,4-glucans have been identified. Compared to β-glucans and chitin, mannans are less rigid and constitute ∼10−20% of the cell wall in *A. fumigatus* and *C. albicans*.[378] In *C. neoformans*, cell walls are embedded in a capsule that contains up to 90% of glucuronoxylomannan (GXM) and galactoxylomannan (GalXM).[379]

A conceptual understanding of the fungal cell wall includes an inner layer made up of branched β-1,3-glucans, which covalently connect to chitin and other glycan components, as well as an outer layer rich in glycoproteins.[380−382] Such supramolecular organization was based on biochemical assays that include initial chemical/enzymatic digestion, fractional solubilization, and isolation of cell-wall components followed by sugar composi-

tional and linkage analysis.[381,383] This method allows for the assessment of biopolymers' susceptibility to chemicals (such as alkali) and enables the identification of key connections between different cell-wall components. The cumulative results lead to the structural scheme in which the chitin−β-glucan center (and further complexed with mannan), an alkali-resistant fraction stabilized by intermolecular covalent bonds, is proposed as the mechanical core (Figure 11A).[3,384] Mass spectrometry techniques, with a focus on the surface layer, have identified the presence of mannans, proteins, α-glucans, and GAGs.[385,386] These molecules are often proposed to regulate fungal virulence by covering the inner cell-wall components and evading the detection of immune receptors.

However, most biochemical techniques are detrimental to the sample, and the imaging methods lack sufficient resolution for precisely disclosing polymer interactions in this complex biomaterial. Therefore, ssNMR methods have been recently developed to investigate polymer composites or whole-cell samples of major fungal pathogens, thus complementing the information collected using conventional methods to advance our understanding of cell-wall architecture.

4.3. Function and Assembly of Biopolymers in Fungal Cell Walls

Recently, we combined ssNMR with MAS-DNP to disclose the cell-wall organization of uniformly ^{13}C,^{15}N-labeled *A. fumigatus* mycelia.[49,80,387] Different from the conventional vision of biochemical assays, which are mostly focused on covalent linkages and the resistance of polymer assembly to chemicals, now we are considering the mobility, hydration, and physical packing of these molecules. Structural polymorphism is found to be a conserved feature of polysaccharides in the native cellular environment. This insight is enabled by the high resolution, typically within 0.7 ppm ^{13}C line width, provided by high-field NMR (800 MHz or above) at room temperature.[49] With the unprecedented resolution, it was found that α-1,3-glucan molecules in *A. fumigatus* mycelia have a structural function beyond expectation. Water-editing and relaxation-based experiments revealed its hydrophobicity and rigidity, respectively, just like chitin (Figure 11B), while 2D ^{13}C−^{13}C/^{15}N intermolecular cross peaks, many of which were enabled by the sensitivity enhancement of DNP, directly revealed the sub-nanometer association of α-1,3-glucan and chitin. This concept had never been reported before because the bulk of α-1,3-glucan can be easily digested by alkali treatment, thus lacking the covalent linkages to the chitin-β-glucan core. However, physical associations allow for the coexistence of α-glucans and chitin to form a rigid and waterproof scaffold around the cell, protecting it from external stresses. These results provide a picture in which the β-glucans serve as tethers between multiple chitin−α-1,3-glucan domains underneath the outer layer of proteins and mannans (Figure 11C).[49]

Ehren et al. investigated the cell-wall organization in the basidiomycete *Schizophyllum commune*,[82] which is one of the most commonly found fungi and can be a pathogen.[388] In this work, they extracted cell-wall components from uniformly ^{13}C, ^{15}N-labeled mycelia by sequentially subjecting the mycelia to PBS washing to remove the cytoplasm, SDS extraction to deplete hot-SDS-soluble components such as β-1,3/1,6-glucans, and alkali extraction treatment to remove α-1,3-glucan. Over the course of these steps, an increasing number of molecules have been removed from the cell wall, as shown by the 2D ^{13}C−^{13}C INEPT-TOBSY and PARIS spectra (Figure 11D). The mobile
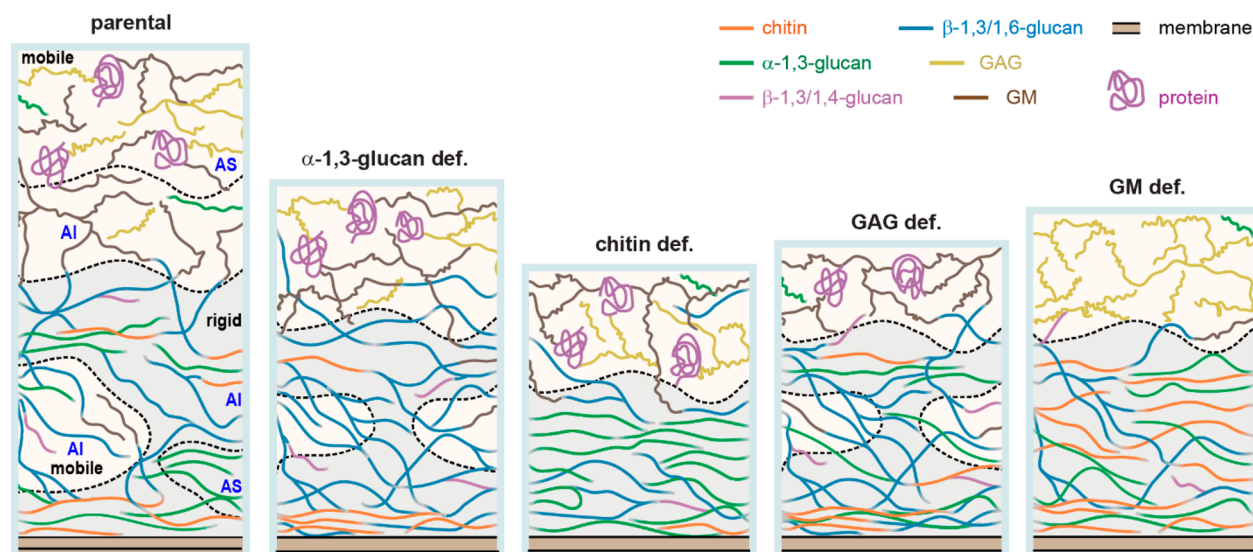
Figure 12. Restructuring of cell walls in the mutant strains of *A. fumigatus*. The mobile and rigid domains are shown as pale yellow and pale blue regions, respectively. The alkali-soluble (AS) and alkali-insoluble (AI) parts are labeled for the parental strain. The molar fractions of polymers in each phase and the average cell-wall thickness observed by TEM were taken into consideration for depicting the schemes. Adapted with permission from ref 387. Copyright 2021 Springer Nature.
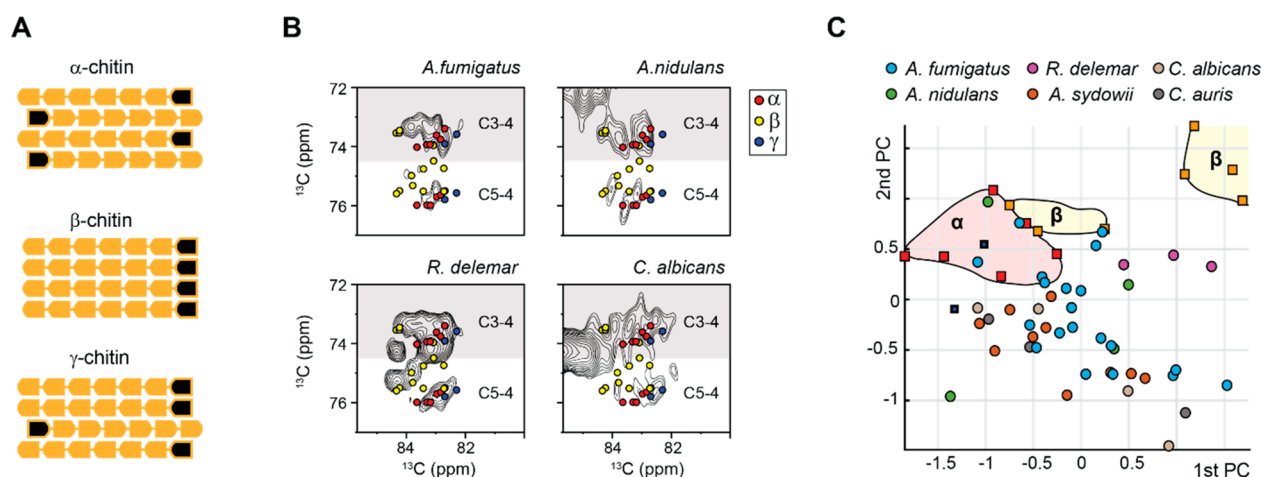
Figure 13. Chitin structure analyzed by ssNMR and PCA. (A) Chitin allomorphs (α, β, and γ) showing different chain arrangements. Black marks represent the non-reducing ends. (B) Comparison of chitin signals in different fungi. Colored dots denote the data from three crystalline forms of chitin: α-chitin (red), β-chitin (yellow), and γ-chitin (blue). (C) PCA scores for chitin NMR chemical shifts projected onto two principal components (PCs). Model chitin allomorphs (α-, β-, and γ-types) are illustrated using squares, while chitin forms identified in the fungi cell walls are displayed by circles. Data from different species are color-coded. The figure is adapted with permission from ref 394. Copyright 2021 Frontiers Media S. A.

part of β-1,3/1,6-glucan is left behind as the primary molecule found in the *J*-based spectra of the final, alkali-treated sample. Signals from lipids and amino acids were exclusively found in the hydrated mycelium but not the treated samples, indicating that they are not part of the cell wall but rather the inside of the cell. ssNMR analysis showed that various forms of glucans, mannose, chitin, and surprisingly fucose constitute the primary components of *S. commune* cell walls (Figure 11E). The rigid part of the cell wall is made of chitin that is likely branched to glucans, while the mobile part comprises the terminal hexoses included in α- and β-linked glucans. Distinct types of mannose species were observed in the mobile region, indicating mannose as being part of an extended, mobile component that is either branched or integrated into mannosylated proteins. These findings confirmed the previously reported arrangement of the cell wall[389−391] and further provided new insights that the rigid

part of the *S. commune* cell wall contains α-(1,3)-glucan and polymeric fucose.[82] In contrast to what has been reported for *S. commune*,[392] Ehren et al. found no evidence of peptides engaging in polysaccharide cross-linkage.[82]

4.4. Reorganization of Fungal Cell Walls in Mutants

It is noteworthy that ssNMR and biochemical analysis have remarkable synergism. Molecules are distinguished by their distribution in the mobile and rigid phase using ssNMR, which complements the view of their covalent linkages and alkali solubility as probed by chemical approaches. In a recent study, the functional diversity of α-1,3-glucan, the molecule overlooked in biochemical assays, was confirmed through its heterogeneous distribution in the alkali-soluble (AS) and alkali-insoluble (AI) portions of the inner and outer domains of cell walls (Figure 12).[387] This study also evaluated the function of GM and GAG, two molecules not discussed in the previous study,[49] and both
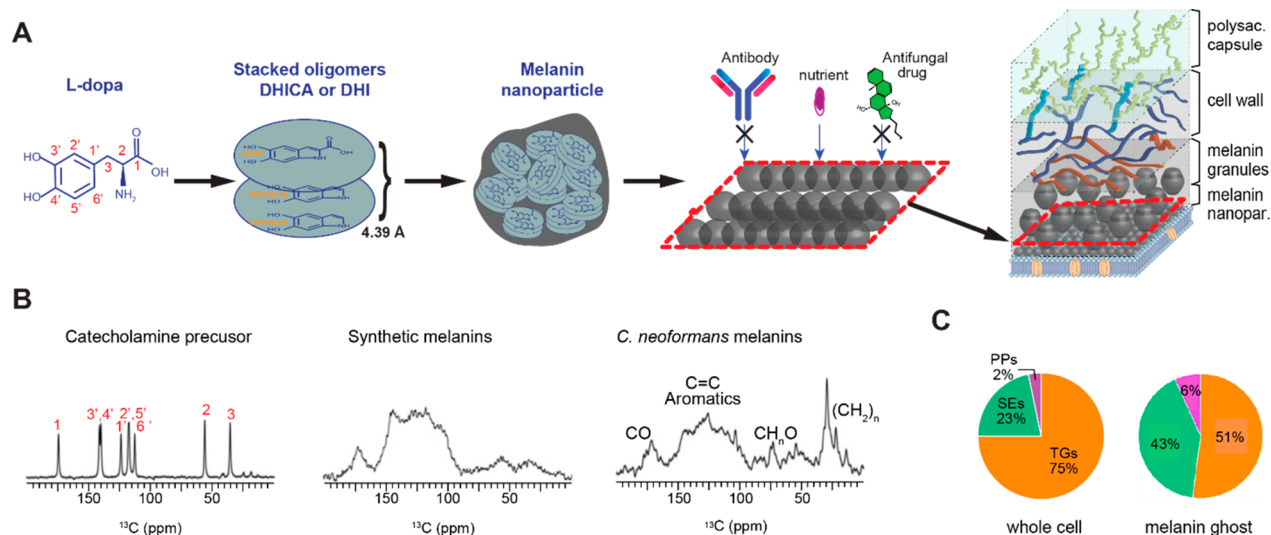
Figure 14. Melaninization of *C. neoformans* cell walls viewed by ssNMR. (A) L-DOPA precursors oxidized by laccase to make dopaquinone; then, 5,6-dihydroxyindol (DHI) or 5,6-dihydroxyindole-2-carboxylic acid (DHICA) is formed by further oxidation. This expanding process continues when DHI/DHICA builds locally ordered oligomers.[402] The accumulation of these smaller units results in the creation of the melanin granular; these melanin granules in turn interact with lipids, proteins, and polysaccharide components in the cell membrane and cell wall. Panel A is adapted with permission from ref 401. Copyright 2005 American Chemical Society. (B) ^{13}C spectra of the catecholamine precursor (L-dopa here; left), corresponding melanins from cell-free autopolymerization (middle), and melanin ghosts produced by fungal biosynthesis (right). Panel B is adapted with permission from ref 404. Copyright 2018 Elsevier. (C) Lipid composition in whole cell and melanin ghost. Panel C is adapted with permission from ref 50. Copyright 2020 Elsevier.

were found to mainly reside in the mobile phase of the cell wall. An unexpected finding is the co-localization of valine and the alkali-insoluble core of the cell wall. The resistance of valine to hot alkali extraction suggested a putative role of this amino acid in stabilizing the macromolecular complex of cell walls.

The combination of ssNMR with functional genomics allowed us to compare the cell-wall organization in a widely used strain (ΔakuB^{KU80}) of *A. fumigatus* and four mutants constructed based on this parental strain.[387] Each mutant selectively eliminates a major structural polysaccharide, including chitin, α-1,3-glucan, galactomannan (GM), and GAG. Using this strategy, we evaluated the structural function of each polysaccharide and monitored the compensatory changes of the cell wall in response to internal stresses. Comparison of different strains indicated that gene deletion significantly reshuffled the molecular composition and spatial organization of cell-wall polysaccharides (Figure 12). These changes were correlated with the sophisticated modification of polymer dynamics and the decreased water retention of cell-wall polysaccharides to rationalize the reorganization of macromolecules in each mutant. The results suggest that fungi tend to produce denser and more hydrophobic cell walls as a mechanism to address structural defects, and further studies are ongoing to validate if this is a generally applicable compensatory mechanism for different fungal species and internal and external stresses.

4.5. Structural Polymorphism of Chitin and Chitosan in Different Fungal Species

Chitin is one of the most important carbohydrate components of fungal cell walls and has a prominent role in protecting and supporting the cell wall.[3] Widely found in almost all fungal species, chitin naturally serves as a promising target for novel antifungal agents.[393] Three model allomorphs (α, β, and γ) of chitin, with major variations in the chain orientation and the hydrogen-bonding pattern, have already been reported by crystallographic studies.[372] In these allomorphs, adjacent chains

are positioned in an antiparallel or parallel arrangement, namely, the α- and β-forms, respectively (Figure 13A). Recently, high-resolution ssNMR was combined with statistical methods, such as principal component analysis (PCA) and linear discriminant analysis (LDA), to compare the ^{13}C chemical shifts of chitin using uniformly ^{13}C-labeled cells of six fungal strains from *Aspergillus*, *Rhizopus*, and *Candida* species.[394] The structure of chitin was found to be intrinsically heterogeneous, with peak multiplicity observed in each sample and with distinct features across fungal species (Figure 13B). Partial similarity was found between fungal chitin and the model structures of α- and γ-allomorphs (Figure 13C). It was also shown that the addition of salt and commercially available antifungal drugs did not significantly perturb chitin's structure, emphasizing the structural resistance of chitin to external stresses. In the same study, the structure of fungal chitosan, a deacetylated form of chitin, was found to resemble a relaxed 2-fold helix conformation. This study provided a promising strategy for analyzing the structure of many other polysaccharides and their numerous conformers across a broad spectrum of fungal species.

4.6. Melanization of Fungal Cell Walls

Another important feature of fungus cell walls that can be described by ssNMR is the pigment deposition in *C. neoformans*, which is both a pathogen and a key model system for understanding fungal virulence.[395] This basidiomycete fungus is a cause of meningoencephalitis, inflammation of the brain and associated tissues, in immunodeficient individuals.[396] *C. neoformans* grown in a nutrient-deficient medium will polymerize and oxidize external phenolic compounds (such as catecholamines), depositing a group of structurally different pigments into cell walls.[397] For example, 3,4-dihydroxyphenylalanine (DOPA) melanin, also called eumelanin, can be synthesized using external precursors.[398] Despite its contribution to cell-wall integrity and microbial pathogenesis,[399,400] the molecular organization of
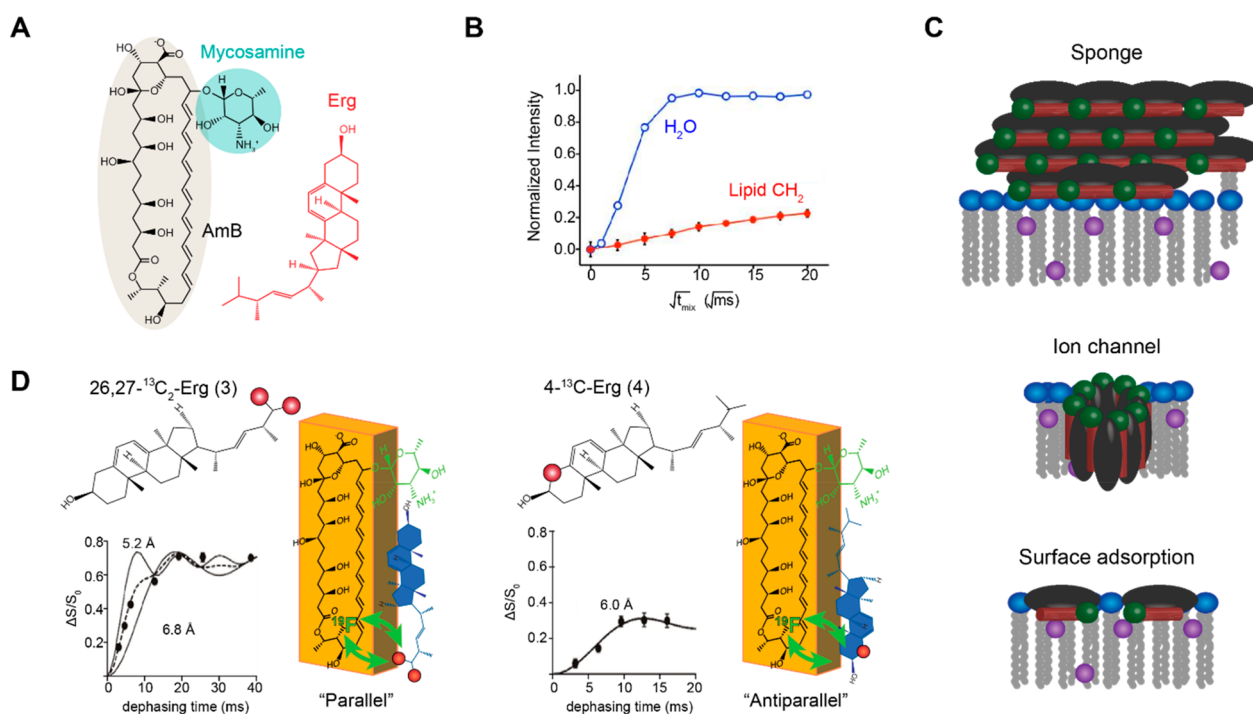
Figure 15. Structure and function of antifungal compound AmB in lipid bilayers. (A) Representative structures of AmB and ergosterol (Erg). (B) ^{1}H spin-diffusion buildup curves revealing slow polarization transfer from the lipid acyl chain to AmBs but fast equilibrium from water to AmBs. (C) The new sterol sponge model based on ssNMR data, disagreeing with the ion channel and the surface adoption models. Purple dots indicate the positions where paramagnetic tags (DOXYL) were covalently linked to lipids to check the PRE effects on AmBs. Panels A, B, and C are adapted with permission from ref 415. Copyright 2014 Springer Nature. (D) ^{13}C$\{^{19}$F$\}$ REDOR data for restraining the parallel and antiparallel orientations between AmB (yellow) and Erg. Left panel: Dephasing values for the Erg $C_{26/27}$ signal at a 32-F-AmB:26,27-^{13}C$_2$-Erg ratio of 1:1. The dashed line is an average of the two solid lines simulated for ^{13}C−^{19}F distances of 5.2 and 6.8 Å. Right panel: dephasing of the Erg C_4 signal at a 14-F-AmB:4-^{13}C-Erg ratio of 1:1, with a fit to a ^{13}C−^{19}F distance of 6.0 Å. Panel D is adapted with permission from ref 425. Copyright 2016 American Chemical Society.

melanin and its association with carbohydrates are still not well understood.

Isolating melanins from the fungi preserves the morphology of the cells, causing hollow spheres called melanin "ghosts". Using NMR cryoporometry on *C. neoformans* melanin extract, Eisenman et al. determined that this assembly is porous, with pore diameters mainly ranging from 1 to 4 nm in diameter, with only a few larger particles around 30 nm.[401] Interestingly, the available volume inside the pore was reduced once antibodies were attached to melanin. This observation led to a proposed antifungal mechanism. Melanin granules are held together in layers, and small nutrient molecules, such as sugars and amino acids, can pass through the pores between the granules, while larger antifungal molecules get blocked (Figure 14A).[401] Camacho et al. further combined ssNMR with EPR, microscopy, and proteomics to determine whether the melanin granules are also associated with non-pigment cellular constituents. In this study, melanin is found to accumulate into much larger spheres of ~200 nm in diameter, called melanin granules, each of which is made up of nanospheres with diameters ~30 nm.[402] Therefore, they uncovered the connection of crude melanin granules to polysaccharides and provided evidence that melanin granules are also connected to proteins.

The biosynthesis of melanin was investigated using the catecholamine precursors, with significant differences observed between the synthetic and isolated melanins due to the requirement of exogenous substrates for melanization (Figure 14B).[403] As revealed by 2D ^{13}C−^{13}C ssNMR and DNP-assisted ^{15}N−^{13}C correlation spectra of *C. neoformans* cell walls, different precursors not only yield distinct melanins but also alter the

structural scaffold of melanized cell walls.[404] Chatterjee et al. applied a set of 1D ^{13}C CP/MAS and 2D ^{13}C−^{13}C correlation techniques to elucidate the mechanism of melanin deposition in *C. neoformans*.[398,405] They studied the development of melanin conformation over time in the cell wall and identified an early stage developing aliphatic scaffold comprised of polysaccharides and acylglycerides and a late-developing aromatic pigment together with indole and pyrrole structural moieties. They were also able to observe a structural network that contains close indole−indole connections and pyrrole−chitin covalent bonds. The observed development of multicomponent melanized assemblies confirmed and substantiated an interlayer deposition model that was proposed previously,[406,407] which will practically guide the therapeutic drug delivery targeting melanoma fungi.[398,408,409]

Zhong et al. developed labeling protocols to enable more detailed investigations of *C. neoformans* melanin using CP-MAS and HR-MAS methods.[410−412] Briefly, implementation of 2,3-^{13}C$_2$-L-dopa and ring-^{13}C$_6$-L-dopa precursors resulted in an indole structure formed from an L-dopa side chain, which revealed the site and structural modification involved in the cross-linking and polymer chain elongation of melanin. With the use of 1-^{13}C-mannoses, it was further demonstrated that purified melanin ghosts contain mannose as β-pyranose, which indicates the integration of 1-^{13}C-mannoses into the pigment-linked fraction of polysaccharides. In addition to mannose, D-glucose-^{13}C$_6$ was found to be integrated into the polysaccharide and aliphatic groups that may be linked to melanin.[412]

The presence of lipid components in *C. neoformans* melanin ghosts was discovered using *J*-coupling-based 2D ^{13}C−^{1}H

INEPT and ^{13}C−^{13}C INADEQUATE experiments, which resolved the signals from triglycerides (TGs), sterol esters (SEs), and polyisoprenoids (PPs). Although the polymer composition (quantified using 1D ^{13}C DP spectra) is comparable in the melanized and non-melanized cells, the melanized cells are particularly rich in SEs and PPs (Figure 14C). Also, the identification of these lipids in the non-melanized cells prepared in nutrient-limited media for a long time period (10−14 days) indicates that they could be produced even under nutrient stress, likely in anticipation of melanin synthesis.

Chrissian et al. compared two *Cryptococcus* species, *Cryptococcus neoformans* and *Cryptococcus gattii*, that share some phenotypic traits. They found that the high content of chitosan in *C. gattii* is associated with the distribution of melanin across the cell walls.[413] It was also shown that lipids and polysaccharides, especially chitosan, play important roles in attaching and layering melanin across the cell walls of *C. gattii* and *C. neoformans*.[413] Interestingly, the spore cell wall from a different fungus, *S. cerevisiae*, which lacks melanin,[414] bears a composition similar to the melanized cells in *C. neoformans*.[397] Indeed, both species use chitosan as a backbone to host either dityrosine or melanin. Similarities observed in these two evolutionarily separated species indicate that chitosan, poly-aromatics, and triglycerides are basic elements in the formation of cell walls. These observations indicate that the composition and architecture of fungal cell walls are crucial factors in hosting and organizing pigments.

4.7. Understanding Structural Dynamics and the Antifungal Mechanism

Solid-state NMR has been and is currently being employed to understand the mechanisms of actions of antifungal drugs. Recently, Anderson et al. proposed a new vision of the functional mechanism of amphotericin B (AmB), which is one of the mainstay agents in the antifungal armamentarium (Figure 15A).[415] In this study, the long ^{13}C−T_1 relaxation times of AmB suggest the formation of rigid aggregates. AmB is also far from lipids, as shown by the slow ^{1}H polarization transfer from the lipid acyl chains of phospholipid membrane (Figure 15B) and the lack of a PRE effect from the paramagnetic DOXYL motifs covalently linked to the C_5 and C_{16} of the lipids. These results lead to a structural model where AmBs dwell mainly in the form of large extramembranous accumulations (sponges), which extract ergosterol from the membranes and eventually lead to cell death (Figure 15C). The extraction of this polyfunctional lipid underlies the resistance-refractory anti-fungal action of AmB and opens a new perspective for describing its cytocidal and membrane-permeabilizing activities.[415] These structural findings revised the prevailing hypotheses that AmB forms ion channels for permeabilizing the membrane and deforming the fungal cell.[416−423] The results also challenge the models where AmB deposits in the intermediate/headgroup region of membranes for sequestering ergosterols.[419,424]

AmBs also exhibited considerable toxicity to human cells, which originates from the binding of this molecule to undesired sterols due to the similarity between fungal ergosterols and human cholesterols.[426,427] Nakagawa et al. used two labeled ergosterols (on the methyl end-group carbons 26/27 or on carbon 4) and two labeled AmB molecules (on carbon 32 or carbon 14) to study AmB−ergosterol and AmB−AmB interactions using ^{13}C{^{19}F} REDOR measurements.[425] The data revealed that AmB attaches to ergosterols in both parallel

and antiparallel orientations at a ratio of 7:3 (Figure 15D). Intermolecular distances showed that the mycosamine part of the macrolide of AmB and the flat α-face of ergosterol directly interact, promoting a face-to-face van der Waals interaction in both parallel and antiparallel alignments. The described van der Waals interaction might help us better understand the sterol recognition mechanism and develop ways to reduce the undesired interaction with human cholesterols.

The exploratory studies discussed in section 4 have demonstrated the capability of ssNMR for deciphering the supramolecular organization of biopolymers in native-state fungal cell walls. Interestingly, the unexpected function of α-1,3-glucan in *A. fumigatus* echoes with the omitted role of pectin in plant primary cell walls, as discussed in section 3.3. Despite the dramatic difference in their dynamics, both molecules are partially extractable by alkali, and therefore, their structural contributions have been overlooked in biochemical analysis. Besides cell walls, ssNMR was also used to characterize the biofilms formed by fungi, for example, in *A. fumigatus*[428] by quantifying different carbon pools inside the extracted ECM. We expect that the methods will result in a wide range of applications, from the systematic assessment of antifungal compounds targeting the cell walls to the structural principles underlying pathogenesis and the emerging drug resistance.[429,430]

5. THE HIGHLY DIVERSE CELL-WALL COMPLEXES OF UBIQUITOUS ALGAE

5.1. Algal Cell Walls Are Structurally Diverse but Under-Investigated

Alga is an informal term regrouping different representatives in the *Eukarya* as well as in the *Bacteria* domains (Figure 1). They are a puzzlingly varied group of species, including multicellular and unicellular organisms, which are usually categorized primarily based on their photosynthetic pigment used for light harvesting during photosynthesis. The 70,000 species of microalgae (small and unicellular aquatic photosynthetic organisms) and 20,000 types of macroalgae (large multicellular aquatic photosynthetic plant-like organisms) include, among others, 8000 green-blue algae, 14,000 red algae, 2000 brown algae, and 10,000−30,000 diatoms.[431,432] They are ubiquitously found in almost all biomes and are adapted to different environments. Algae have a size ranging from less than a micron in diameter (e.g., microalga *Prochlorococcus*) to ~60 m long (e.g., macroalga *Macrosystis*).[433,434] Strong from their 2.5 billion years of evolution, microalgae not only populate shallow oceans but are also found as deep as 300 m (e.g., *Navicula pennata* diatom), in polar ice, and even in aerial environments.[435−438] Due to the extremely high diversity of algae, most studies only focus on the production of molecules of biotechnological interest, usually by microalgae because of their rapid growth, rather than the structural principles of cell-wall assembly, for example. Indeed, some natural or artificially designed algae can be optimized to overproduce fatty acids for biofuels,[439,440] or minerals, proteins, vitamins, and polysaccharides for human health and nutrition.[441]

The morphology of algal cell walls can also be very different, with assemblies being simple "scales" coating the cell surface, more organized organic assemblies, or even almost purely crystalline mineral phases such as the silicon or bicarbonate crystals found in diatoms.[442] As for the composition, the main structural elements are polysaccharides, although highly rigid
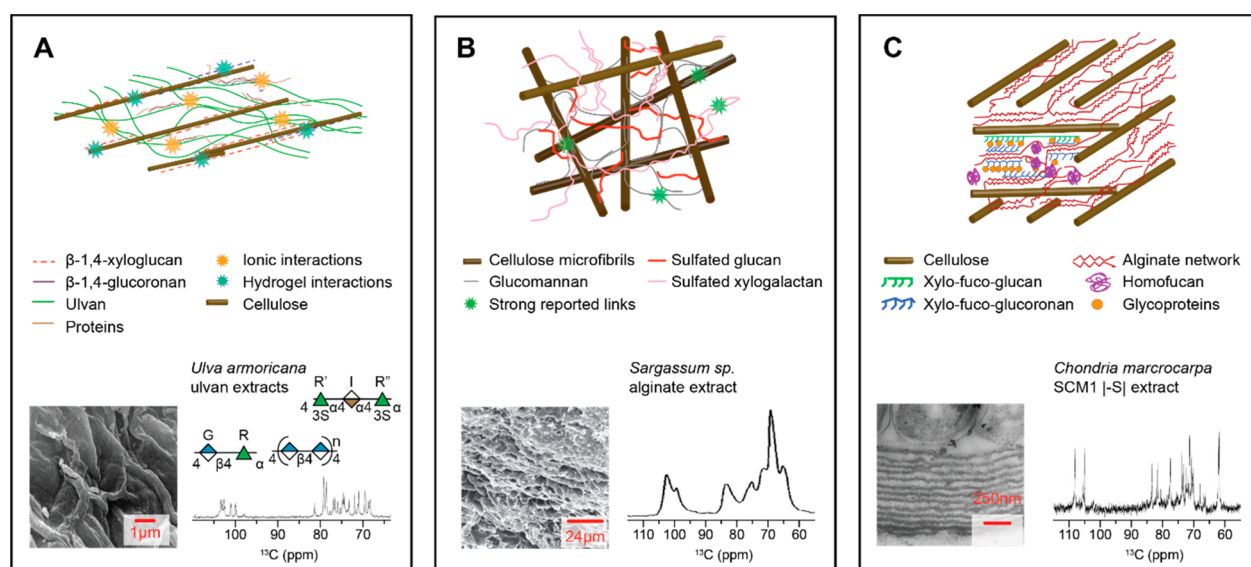
Figure 16. Cell-wall architecture of three major types of algae. On the top of each panel, structural models were proposed for the cell walls of (A) green, (B) red, and (C) brown algae.[455,456] At the bottom of each panel, ^{13}C NMR spectra (right) and SEM/TEM images (left) were shown for (A) *Ulva armoricana*,[457] (B) *Sargassum sp.*,[458] and (C) *Chondria macropcarpa*.[459] Panel A is adapted with permission from refs 455 and 460. Copyright 2007 American Chemical Society and Copyright 2020 Egyptian Society for the Development of Fisheries and Human Health. Panel B is adapted with permission from refs 458 and 461. Copyright 1997 Canadian Science Publishing and Copyright 2015 Springer Nature. Panel C is adapted with permission from refs 456, 459, and 462. Copyright 2010 John Wiley and Sons, Copyright 2002 Walter/De Gruyter GmbH & Co. KG, and 2015 Springer Nature.

glycoprotein granules and biosilica shells are also found (Figure 2).[4] Typically, algal-cell-wall polysaccharides include cellulose, mannan, xylan, alginic acid, chitin, sulfated glycans,[443,444] agar, keto sugars, extensin, lignin, and homogalacturonan.[4] Research on algal-cell-wall composition and structure started as early as in the 1950s using enzymatic reactions and chemical titration, with a focus on the chain length and branching of xylan in red algae and polysaccharide metabolism in marine species.[445−447]

Structural models have been proposed for some algal cell walls, although a considerable variation should exist within each specific group (Figure 16). Most related studies focus on polymer cross-linking and cation complexation.[448−450] Water molecules are important to the organization of cell walls, where hydrogel binding and ion interactions play key roles in maintaining the wall integrity. Green algae are the most studied systems due to their rapid growth and universal availability in nature. They usually have a fibrous cell wall, sometimes including cellulose fibrils associated with more dynamic xyloglucan and glucoronan (Figure 16A). Green algae also contain long polymers called ulvans and a higher protein content compared to plant cell walls. Compared to green algae, red algae contain more sulfated glycans including glucans and xyloga-lactans and usually have more and thicker cellulose (Figure 16B). Red algae also have mannan-rich polymers cross-linking with other glucomannan or cellulose fibrils. As for brown algae, they have a thicker cell wall with cellulose microfibrils and a hydrated complex formed by alginate, in which glycoproteins can be found associated with other xylan/glucan-rich poly-saccharides and fucans (Figure 16C).

The complexity of the algal cell wall requires a variety of solution and ssNMR methods as well as nuclei to characterize its different organic and inorganic components. Solution ^{1}H NMR was employed to detect the cell-wall components of several brown algae including *Fucales* and *Himanthalia elongata*, which revealed the interaction between fucose-containing sulfated

polysaccharides, proteins, and cellulose in the cell wall and the association of alginate with phenolic compounds in the surrounding matrix.[451] They also managed to track the modification of glycan linkages and metabolomic dynamics of *H. elongata*, in response to a changing habitat. Besides the ^{13}C methods for identifying carbohydrate components (Figure 16), ssNMR has also exploited ^{15}N signals to track the cellular degradation of *Botryococcus barunii* green algae,[452] ^{31}P to study phosphate−calcium complexes in *Ulva lactuca* cell walls,[453] and ^{29}Si to characterize the mineral components in diatoms.[454] However, the algal cell wall remains substantially under-investigated (Figure 1). Solid-state NMR has been mostly used to identify algal-cell-wall components but never as intensively as for plants or even the fungal or bacterial cell walls.

5.2. Plant-Like Extracellular Matrixes

Most NMR publications dedicated to algal cell walls report organisms whose constituents are similar to the carbohydrates found in higher plants.[463] Cellulose is an important poly-saccharide found in almost all types of algae, and its structure, degree of polymerization, production, and extraction have been especially studied in green algae, mostly *Cladophorales* and *Siphonocladales* orders.[464,465] For example, *Valonia ventricosa* has been investigated because this large unicellular organism (diameter up to 5 cm) produces square-shaped cellulose crystallites,[466−468] which allowed the identification of the biphasic character of type I cellulose (Iα and Iβ) by ^{13}C CP-MAS data.[469]

A plant/liverwort-like[470] mannose-rich cell surface and cell walls have been reported in *Codium fragile*—the giant-cell alga—based on ^{13}C ssNMR data.[471] This work identified two types of 1,4-linked β-D-mannans in the cell wall replacing cellulose fibrils: mannan type I alkali-soluble fibrils and mannan type II alkali-resistant fibrils. Similar to cellulose, ssNMR has also been used to describe the coexistence of crystalline and non-crystalline mannan and orientational order/dynamics in the cell
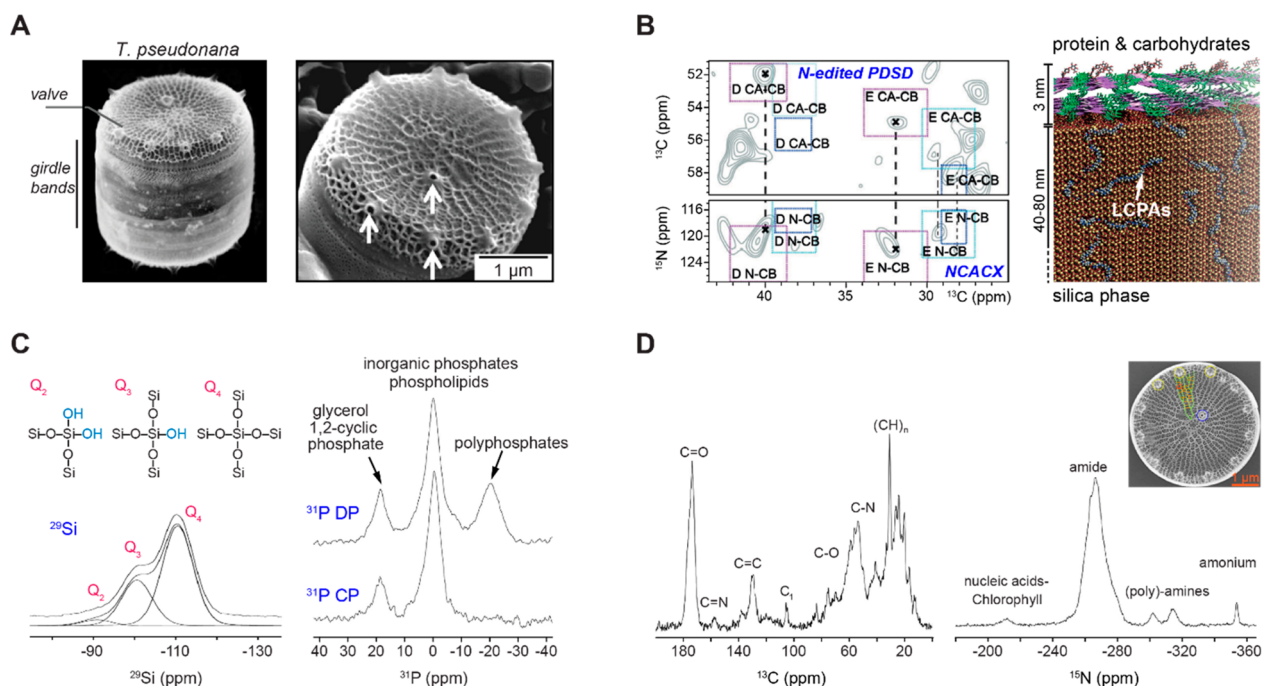
Figure 17. Characterization of the diatom cell wall and frustule using ssNMR. (A) SEM images of the diatom showing valve biosilica that have organic threads (white arrows).[505] Panel A is adapted with permission from refs 505 and 506. Copyright 2018 Frontiers Media S.A and copyright 2010 Springer Nature. (B) DNP-assisted ^{15}N-edited [13]C−[13]C PDSD correlation (top) and N(CA)CX experiments (bottom) detecting amino acid signals as mostly in the β-sheet conformation in *S. turris*.[220] The structural model contains a 3 nm layer of carbohydrates and proteins covering the 40−80 nm silica domain with LCPAs enclosed. Organic matter and silicon can be detected within (C) whole cell and (D) extracted diatom shells (frustule), as adapted from Tesson et al.[507] (C) ^{31}P NMR detects lipids, glycerol 1,2-cyclic phosphate, and polyphosphates, while [29]Si data reports Q2, Q3, and Q4 silicon environments. (D) ^{13}C ssNMR reporting organic molecules including proteins and carbohydrates. Extracted shells with SDS conserve their overall native structure as seen by SEM.[508] The valve costa (green line), cross-connections (orange lines), areola pore (red circle), and fultoportula (yellow/blue circles, tube-like structures) can be observed. Panel B is adapted with permission from ref 220. Copyright 2015 John Wiley and Sons. Panel C is adapted with permission from ref 507. Copyright 2008 Springer Nature. Panel D is adapted with permission from refs 507 and 508. Copyright 2008 Springer Nature and Copyright 2019 Springer Nature.

wall of the alga *Acetabularia*, known as mannan weed.[472] Specifically, the transition of the less-crystalline mannan-rich cell wall in diplophase to the cellulose-dominant cell wall in haplophase has been examined, which goes with mannan being the scaffold for the early stage of alga prior to cellulose. In this work, other molecules have also been identified in these flexible assemblies, including xyloglucan, pectic polysaccharides, as well as a small number of homorhamnan, galactomannan, glucogalactomannan, and also xylan.

Similar to the plant counterpart, algal cellulose is perceived as stiff fibrils mixed with other polysaccharides such as the insoluble portion of xylan.[473,474] This insoluble complex coexists with soluble fractions mostly containing other types of xylan, sulfated carbohydrates, and xyloglucan, as identified by ^{13}C ssNMR in *Nemaliales*, *Palmariales*, and *Caulerpa* species.[475−479] Some algal species (such as *Charophyceae*) even contain HG, RG-I, and hemicellulosic polymers, as well as MLG and lignin-like molecules.[4] Finally, another important constituent found in algae is arabinogalactan-rich proteins called AGPs, which are usually found in the extensin-like portion of photosynthetic organism cell walls[480] including in plants.[481] In algae, AGPs are typically associated with hydroxyproline-rich glycoproteins (HRGPs) or N-glycosylation.

5.3. Sulfated Polysaccharide and Other Aliphatic Components

Other glycans have been reported in algal cell walls, most notably a wide range of sulfated saccharides.[470] Sulfate moieties are often described in soluble extracts and therefore

characterized using solution NMR, and these molecules are found decorating cell-wall polysaccharides in native samples, mainly on galactans in red algae (Rhodophyta)[482,483] and on fucans of brown algae (Phaeophyta).[484] Oceanic green algae of the genus *Codium* have also been demonstrated to have a large amount of sulfated galactan. In a study of *Codium isthmocladum*, Farias et al.[485] extracted and characterized 4-sulfated 3-β-D-galactopyranosyl units using solution NMR. Sulfated fucans cross-link different elements in the brown alga *Fucales*, leading to complex NMR spectra. Therefore, cell-wall extraction and purification are necessary to recover the structural information and, for example, to confirm the presence of sulfated fucans and unique α-1,3-L-fucans.[451]

Several fucose-containing sulfated polysaccharides called *fucoidans* have been reported in brown algae and exhibited antioxidant or anti-inflammatory activities.[486,487] Agar units can also be sulfated or methylated at different positions, giving furcellaran, funoran, porphyran, and carrageaenan, which have been differentiated using ^{13}C ssNMR.[488−490] Solid-state NMR has also been conducted to separate agars and carrageenans extracted from red algae.[488]

Alginate is the most abundant gel-forming molecule in the cell walls of brown algae and is considered as the main component for the control of ECM rigidity. The regulation of the gel strength is based on the frequency of polyguluronate blocks in the polymeric chains of alginate through the enzymatic conversion of β-(1−4)-mannuronate to α-(1−4)-guluronate.[491] Ulvan is a water-soluble sulfated polysaccharide found in green

seaweeds and is the only one predominantly rich in rhamnose. Ulvan has been identified in different seaweeds using ^{13}C NMR, together with other polysaccharides such as xyloglucan, cellulose, and glucoronan.[492]

Algaenan is a highly aliphatic molecule widely distributed in unicellular algae cell walls.[493] This biopolymer coexists with polysaccharides in many algal cell walls. For example, ^{13}C CP/ MAS characterization of cell-wall extracts revealed the coexistence of algaenan with proteins and other polysaccharides such as cellulose and β-1,4-mannan in *Coelastrum sphaericum* green algae.[494] Algaenan is thought to induce local heterogeneity by creating gaps in crystalline materials, thus providing the flexibility needed for cell division.[495] Furthermore, this work reports the assignment of ^{13}C signals from algaenan and fibrillar polysaccharides as well as the linkages within algaenan or between algaenan and cellulose. More recently, HR-MAS NMR and ESI-MS have been used to describe the structural features of the *Botryoccocu braunii* algaenan-rich cell wall, where hexane-insoluble botryals is found to reticulate and form algaenan.[496]

5.4. A Dilemma of Non-Cellulosic, Fungi-Like Cell Walls

Chitin is the second most available polysaccharide in the biosphere but is far less studied compared to cellulose. Usually, chitin is found in arthropods, nematodes, and fungi, but it has been reported in some microalgae, mostly diatoms. The studies of chitin using XRD and FTIR[497,498] are typically associated with biomineralization happening in diatoms.[497,499] NMR studies of diatoms will be reported below in section 5.5. Nonetheless, ^{1}H NMR data has also reported chitin in the freshwater green microalgae *Chlorella*;[56] however, chitin is also associated with algal pathogens, which might explain the presence of chitinases in many microalgae. Chitinase from *Volvox carteri* has been isolated, and its crystal structure was determined by X-ray crystallography. Solution ^{1}H and ^{15}N NMR, in combination with isothermal titration calorymetry (ITC), allowed the interaction strength of chitinase with chitin oligosaccharide to be determined.[500] Therefore, caution is needed when referring to older publications mentioning chitin as an algal-cell-wall component. However, microalgae can be genetically modified to produce chitin, as shown with *Chlorella* using chloroviruses.[501] Solid-state NMR might be a suitable tool for exploring this type of algal cell walls, as it can resolve the signals of chitin and related cell-wall molecules using intact cells.[49,82]

5.5. The Diatom Mineral Shell

Diatoms include over 20,000 species[431,432] and are among the most common form of phytoplankton, being responsible for more than 25% of the world's net primary production (NPP). These microorganisms are primary producers mostly found in fresh water and oceans, where they support the survival of most higher organisms. Diatoms are covered with a silicified skeleton (frustule), which is a natural hybrid of organic and mineral material. Its external shell is made of two distinct regions, i.e., the valves (on top) separated by the girdle bands (on the side) (Figure 17A). The valves are the nanoscale-sculpted parts of the diatom shell that allow molecular transport and efflux, while the girdle bands are the structural elements holding the valves together. Diatom cell walls are rich in silica and also contain organic components such as proteins, long chains of polyamines, and polysaccharides.[502] Silica production in diatoms has been proposed to be initiated in silica deposit vesicles (SDVs) where the valves and girdle bands are built. However, mobilization and trafficking precursors, exocytosis, and even associated protein are still either poorly understood or unknown.[503] Current

knowledge on the synthesis mechanisms involved in diatom cell division and cell-wall building is summarized by Shrestha et al.[504]

Baldus, Brunner, and co-workers have employed MAS-DNP methods to characterize [^{13}C, ^{15}N, [29]Si]-enriched biosilica from *Stephanopyxis turris*[220] and *T. pseudonana*.[509] 2D [13]C—[13]C/^{15}N experiments distinguish the secondary structure of the proteins involved in the diatom cell wall of *Stephanopyxis turris*,[220] showing mainly a β-sheet structure (Figure 17B). The low DNP enhancement observed on LCPA suggests these molecules as being included in the thick (40–80 nm) biosilica matrix instead of the thin (3 nm) protein layer in which the polarizing agent should penetrate and diffuse easily.

Little is known about the frustule biosynthesis, but our understanding of the cell-wall architecture and association of organic molecules has been improving. Two major proteins, namely, silaffins/silacidins and long-chain polyamines (LCPAs), have been identified in the organic phase of the diatom cell wall,[510] while cingulins were found to be associated with the girdle bands and involved in the 3D organization of the frustule in *Thalassiosira pseudonana*.[511] Interestingly, chitin has also been described in *T. pseudonana* cell walls, where it would be associated with valve formation,[512] suggesting that the architecture of the biosilica cell wall is solidified with a chitin network. In addition to these soluble materials, insoluble microtubule and actin microfilament networks were found in the cell. These insoluble regions were found to be associated with the SDVs during valve formation and were important for SDV positioning and mesoscale organization of silica.[513,514]

Silica is the most abundant component in the diatom matrix; therefore, the [29]Si spin $^1/_2$ nucleus is of interest for ssNMR characterization despite their ~5% natural abundance (Figure 3). The ensuing low sensitivity makes it difficult to characterize silica in cellular systems. Using isotopically enriched [29]SiO_2, NaH[13]CO_3, and Na[15]NO_3, Tesson et al.[507] and Kolbe et al.[515] produced labeled samples of *T. pseudonana* and *Cyclotella cryptica* diatoms. The combination of ^{31}P, ^{13}C, ^{15}N, and ^{29}Si ssNMR methods allowed the identification of signals from carbohydrates, nucleic acids, biosilica, lipids, and proteins using a single sample (Figure 17C,D). Three [29]Si broad peaks were detected, namely, Q^2, Q^3, and Q^4, corresponding to different levels of condensation of SiOH moieties, referring to different numbers of hydroxyl groups converted to Si groups in the building block of biosilica (Figure 2). Therefore, 1D [29]Si spectra are sufficient for determining the degree of condensation of SiOH using the Q^4/Q^3 ratio (Figure 17C).[516] Tesson et al.,[507] together with other groups,[517] further showed that changing the medium salinity modifies the material density and packing and increases the amount of organic component in the frustule, even if the organic phase is made of the same elements. ^{13}C and ^{29}Si ssNMR results confirmed the presence of proteins[220] and polysaccharides within the silica network.[507] Comparison between ^{31}P DP and CP differentiated the mobile polyphosphates from the more rigid inorganic phosphates, phospholipids, and glycerol-1,2-cyclic phosphates (20–30% of the diatom's phosphorus).

Tesson and Hildebrand also reported the cell-wall composition of many other diatoms,[518] such as *Amphora salinam*, *Stephanopyxis turris*, or *Navicula cryptocephala*, in which glucans were identified. The major form contains β-1,3-linkages and is called *chrysolaminarin* as an energy storage molecule or *callose* when in a fibrillar form associated with the cell wall. Mannan-rich carbohydrates and more recently chitin have also been
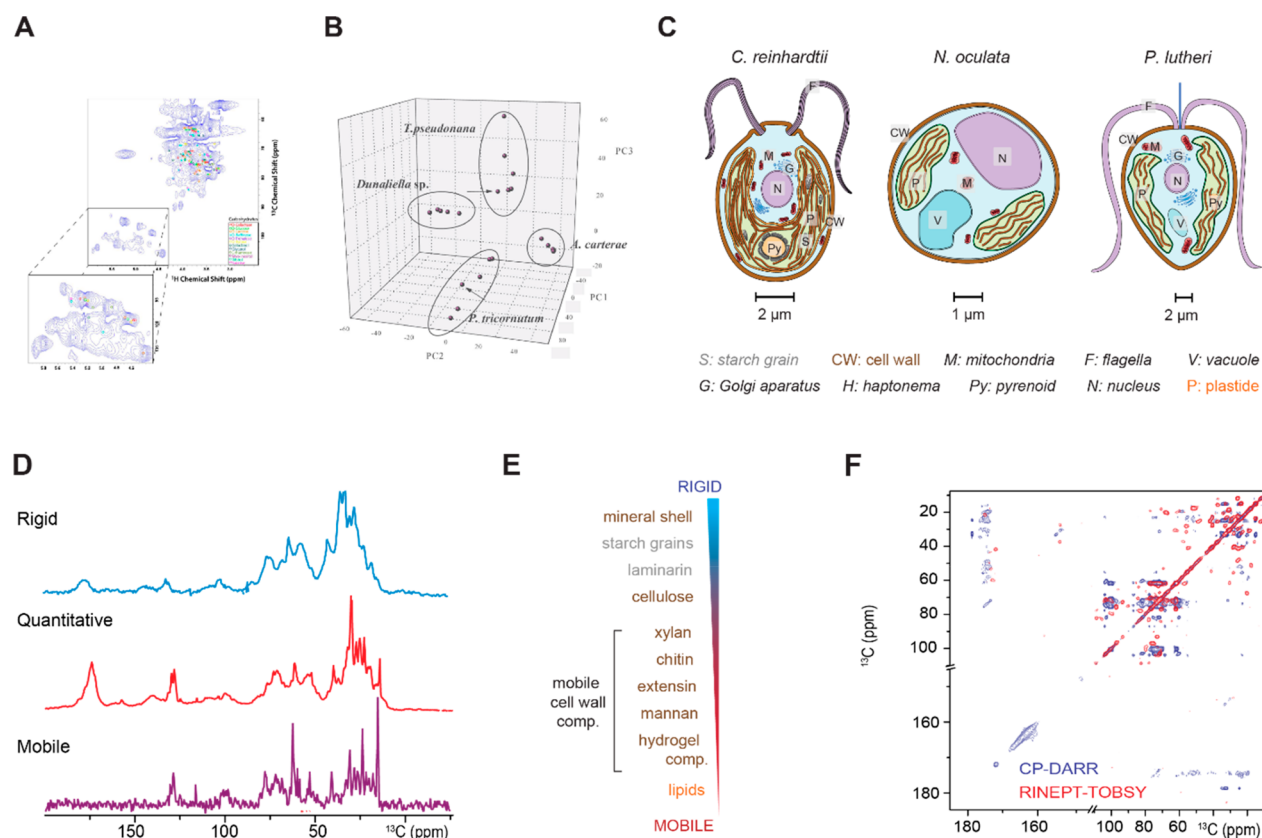
Figure 18. High-resolution solution and solid-state NMR on whole-cell samples of algae. (A) Solution NMR of whole-cell *C. reinhardtii* resolving carbohydrate and amino acid signals. Panel A is adapted with permission from references.[523] Copyright 2016 Springer Nature. (B) HR-MAS allowing to make principal component analysis to distinguish algal species based on the metabolite composition. Panel B is adapted with permission from references.[528] Copyright 2018 Springer Nature. (C) Morphological diversity in multiple green microalgae recently studied by ssNMR. Differences are mostly based on cell-wall type, lipid head groups, and storage molecules. (D) 1D ^{13}C ssNMR spectra probing polymers in different regimes of dynamics in *C. reinhardtii*. The dynamic and rigid molecules were probed using RINEPT and CP, respectively. Quantitative detection was achieved using DP with long recycle delays. Panel D is adapted with permission from references.[532] Copyright 2015 Elsevier. (E) Summary of glycosylated components in different regimes of dynamics. (F) 2D ^{13}C spectra of *C. reinhardtii* showing rigid carbohydrates and proteins in CP-DARR and mobile lipids and proteins in a RINEPT-TOBSY spectrum. Panel F is adapted with permission from references.[533] Copyright 2018 Springer Nature.

reported. Chitin occurs in numerous calcium-based biominerals[519] where it forms insoluble compartments within the cell wall that is associated with mineralization. This phenomenon has been studied in detail only recently using ssNMR,[512] although it was reported almost 60 years ago.[520] Indeed, most recent works report both surface[507] and interior[512] chitin molecules that can be important within the cell wall of *T. pseudonana*. ^{13}C labeling allowed the identification of α- and β-chitin allomorphs in *C. cryptica*[515] and *T. pseudonana*,[512] respectively associated with silica and structural chitin. Finally, glucoronomannan was found to be of high significance to cell-wall biogenesis in some diatoms. In *Phaeodactylum tricornutum*,[521] ^{1}H and ^{13}C NMR allowed the resonance assignment of the α-1,3-mannans that are decorated with sulfate ester groups and β-D-glucuronic residues.[442]

The contacts between biosilica and organic molecules in *Thalassoria pseudonana* and *Cyclotella cryptica* cell walls have been assessed using both {^{1}H}−^{13}C−^{29}Si double CP-based HETCOR and ^{13}C{^{29}Si} REDOR expriments.[515,522] Contacts were observed between the ^{29}Si in silica and the ^{13}C sites of long-chain polyamine (LPA) and chitin.

5.6. Trends in Whole-Cell Investigations of Microalgae

Multiple solution NMR methods have been developed to allow the use of whole-cell samples for characterizing the dissolved components or gels made of very mobile aquatically available molecules.[523] This has been achieved using suspensions of intact ^{13}C-labeled cells of *Chlamydomonas reinhardtii*, *Chlorella vulgaris*, and *Synechocystis sp.* green microalgae placed in solution NMR tubes or through more complex setups. For example, Farjon and co-workers have flown a microalgae suspension through a benchtop solution NMR spectrometer to allow live-cell metabolomic studies focusing on lipid metabolism.[524,525] Based on a more solid-like method, Simpson and co-workers are developing comprehensive multiphase NMR (CMP-NMR) to probe the dynamically distinct phases in intact cells. Indeed, MAS can be combined with magnetic field gradients and also lock andfull susceptibility matching, all of which can be built with a solid-state circuitry to allow high power pulses needed for characterizing gel/solid samples.[526] Application of this method to microalgae led to the identification of several cell elements in native *Hyalella azteca*, such as different amino acids, glucosamine, glucose, and trehalose.[526] Using these methods, multidimensional NMR experiments reported the signals of polysaccharides from the very mobile, gel-like, and even rigid fractions of cell walls as well as metabolites. It should be noted that the same multiphase NMR approach has also been applied to higher organisms such as *Daphnia magna*.[527]

Figure 19. Structure and packing of microalgal carbohydrates resolved by 2D ssNMR of whole cells. (A) ^{13}C refocused DP-based J-INADEQUATE spectrum of uniformly ^{13}C-labeled *P. beijerinckii* cells with a 2 s recycle delay selecting the mobile polysaccharides. (B) Difference spectrum obtained from two parental spectra (PAR and CORD) showing only long-range intermolecular or inter-residue contacts. A representation of identified inter-residue contacts of starch is illustrated on the top. (C) 1D ^{13}C cross sections of the 2D INADEQUATE spectrum showing splittings based on $^1J_{CC}$ couplings for the S[a] residue. Carbon numbers are labeled on the sides of each panel. The deconvoluted (blue) peaks are plotted underneath the simulated (magenta) and measured (black) spectra. Adapted with permission from ref 534. Copyright 2021 American Chemical Society.

Precursors and degradation products can be analyzed using multidimensional solution NMR, which allowed one to assign amino acids and glycans released by microalgae in the medium after natural enzymatic hydrolysis (Figure 18A).[523] HR-MAS data have been associated with statistical tools such as PCA to differentiate microalgal species (Figure 18B).[528] In fact, HR-MAS is of interest for gel-like materials, even for those included in whole-cell samples. Chauton et al. focused on the characterization of *P. tricornutum*, *Chaetoceros muelleri*, *T. pseudomona*, *Dunaliella sp.*, and many other marine microalgae using both ssNMR and HR-MAS techniques.[529−531] PCA results of the ^{1}H and ^{13}C data of a large number of metabolites and middle-sized molecules provided reproducible differences between strains and species, which are further linked to the nutritional values of those samples.

Systematic ssNMR characterization of whole microalgae has been conducted recently.[74,532,533] In 2015 and 2018, Arnold et al. employed spectral editing methods to selectively detect cell constituents based on their overall dynamics. Three organisms have been investigated including the freshwater *C. reinhardtii* (wild-type and cell-wall depleted strains) and marine microalgae *Nannochloropsis oculata* and *Pavlova lutheri* (Figure 18C). Combination of dynamic filters and 1D ^{13}C ssNMR spectra proved a valuable strategy for differentiating cell compartments (Figure 18D) with sequentially increasing dynamics: the rigid energy-storing starch grains, the intermediately dynamic polysaccharides in the cell wall, and the very mobile saccharides in the galactolipids found in membranes (Figure 18D,E). A range of different magnetization transfer techniques and spin-diffusion filters (i.e., long PDSD mixing time) have been combined to highlight starch, the most abundant and most crystalline element of microalgae (Figure 18F). In *C. reinhardtii*, the rigid fraction is dominated by starch, whose crystal type has been determined directly in the cell,[79] while the mobile fraction includes lipids and several polysaccharides. 2D ssNMR experiments, such as TOBSY, DARR, and PDSD, enabled the

unambiguous identification of galactofuranose and arabinofuranose, which are likely associated with cell-wall glycoproteins.

Recently, we have introduced a broadly applicable protocol for quantifying the content and linkages of glycans in microalgae using ssNMR spectroscopy.[534] The method was demonstrated on a naturally cellulose-deficient strain (CK-5) of the green microalga *Parachlorella beijerinckii*, which is a promising candidate for producing high-value fermentable carbohydrates. 2D [13]C−[13]C correlation spectra of uniformly ^{13}C-labeled cells revealed that most of the carbohydrates in the glycolipids and cell walls are highly mobile; therefore, we can use 2D ^{13}C DP INADEQUATE with short recycle delays (Figure 19A), an experimental scheme preferentially detecting mobile molecules, to quantify the glycan composition. Starch was found to dominate the rigid phase of this microalga, and its content was separately calibrated using a calibration factor, which was obtained by comparing the starch intensities in two 1D ^{13}C spectra with either selective detection of mobile components or quantitative detection of all molecules. This nondestructive method provides accurate quantification of the amount and linkage of glycans using whole-cell samples, as verified by the good agreement with MS results.

In addition, starch was found to adopt a well-organized structure in the cell, as shown by the extensive intermolecular contacts between its constituent molecules (Figure 19B).[534] Some xyloses were found to exist in both the mobile and rigid regions of the cell wall, with their chemical shifts partially aligned with the flat-ribbon 2-fold xylan that was initially recognized in plants. Therefore, some structural components of algal cell walls, probably the glycoproteins, provide the even surface required for accommodating the flat-ribbon structure of 2-fold xylan. For the first time, one-bond scalar couplings ($^1J_{CC}$) were systematically observed for almost all carbohydrate components in cellular samples, enabling future explorations using J-coupling in ssNMR to facilitate structural determination (Figure 19C).

In conclusion, the ssNMR studies reported the remarkable complexity of the architecture and synthesis of microalgal cells.

Figure 20. Composition and architecture of PG and teichoic acids in Gram-positive bacteria. (A) AFM images of PG in *S. aureus* cells revealing the ring architecture made of concentric peptidoglycan fibers. The strand width and inner-strand distances of PG were also shown. Panel A is adapted with permission from ref 550. Copyright 2020 Springer Nature. (B) Representative structures of PGs in *S. aureus* and *B. subtilis*, with different stems and bridges. (C) ^{1}H-detection ssNMR of PG amino acids under ultrafast MAS of 100 kHz. Overlay of ^{1}H$-^{13}$C correlation (red) and 2D hHcH-TOCSY correlation (black) spectra showed through-bond correlations, as indicated using dashed lines. Panel C is adapted with permission from ref 88. Copyright 2019 Elsevier. (D) WTA was another important component of the Gram-positive cell wall. ^{31}P and ^{13}C spectra detect the different structural motifs in WTA. Panel D is adapted with permission from refs 552 and 553. Copyright 2009 American Chemical Society and Copyright 2018 American Chemical Society.

Due to the incredible diversity of microalgae, only a small fraction of these organisms has been studied in detail so far. Further developments are to be expected, with interesting insights from a variety of nuclei that can be detected and incorporated into this kind of organism.

6. SOLID-STATE NMR INVESTIGATIONS OF BACTERIAL EXTRACELLULAR MATRIXES

6.1. Bacterial Cell Walls and Biofilms

Bacteria are universal species found in all biomes and can survive extreme conditions.[535] Commonly considered as the simplest living organisms, bacteria may closely resemble the Earth's original living organisms due to their prokaryotic cellular organization. Bacteria play key roles in atmospheric nitrogen capture and degradation of organic matter.[536] They are also associated with toxic or contaminated environments where uncontrolled bacterial growth can be devastating as well as with many diseases found in humans, animals, or plants. Exposure to antibiotics has been dated back to 350−550 Common Era, as revealed by traces of tetracycline found in human skeletal remains.[537,538] Today, antibiotics target a broad spectrum of metabolic pathways in bacteria, such as depolarizing cell membranes and inhibiting the synthesis of specific proteins, nucleic acids, and cell-wall components.[539] However, bacteria readily adapt to antibiotics and develop resistance mechanisms,[540] the timeline of which can be as short as 1 year as seen with daptomycin.[541] The resistance mechanisms developed by bacteria include efflux pumps, limitation of drug uptake by cell surface modification, modification of cell-wall precursors or target molecules, and direct degradation of antibiotics.[542,543]

This is why bacterial infection and multidrug resistance will continue their significant impacts on all living organisms.[31,32]

Nowadays, most antibiotics are targeting bacterial cell walls. From a structural point of view, Gram-positive bacteria have a thick peptidoglycan (PG) cell wall, with lipoteichoic acid (LTA) cross-linking different PG layers and outer components such as the glycoprotein-rich S-layer and the polysaccharide capsule (Figure 2). Gram-negative bacteria have a thinner peptidoglycan layer protected by a second outer membrane mainly made of lipopolysaccharides (LPS), with further coverage by entangled S-layer and capsule components. Bacteria can also be found in a highly organized multicellular arrangement called biofilms.[34] Once bacteria adhere to a surface, they can adopt a sedentary behavior and grow in a complex organic viscoelastic material. This extracellular polymer substance (EPS) consists of an assembly of curli amyloids and different polysaccharides such as cellulosic derivatives. The carbohydrate components facilitate surface adherence and act like glue to help curli association and coherence. Biofilms protect the microorganisms from chemical and mechanical clearance processes, making bacterial communities a threat to human health, as seen with medical devices and implants.[544,545] It has been estimated that 60−80% of chronic human microbial infections are associated with bacterial biofilms.[546] Understanding the overall architecture, synthesis, and remodeling of cell walls and biofilms is thus of great interest.

An increasing number of research groups have been using ssNMR to elucidate cell-wall architecture and the structural factors driving cell adherence and biofilm assembly.[19,547−549] We will highlight the recent advances in understanding bacterial ECMs using bacterial cells or extracts. We will also briefly
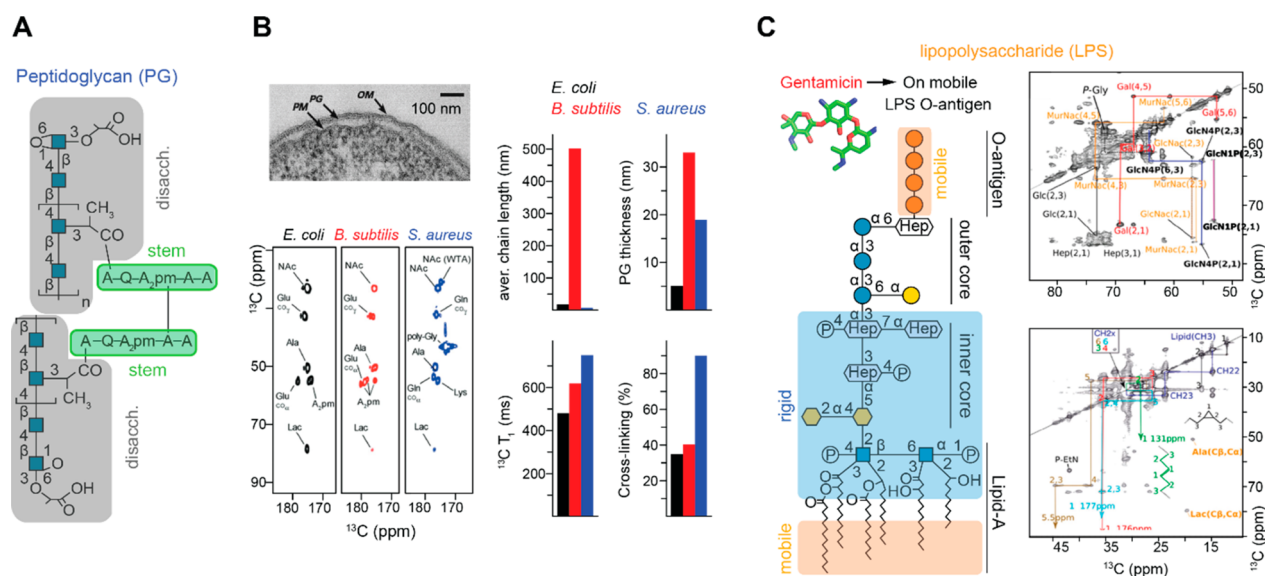
Figure 21. Peptidoglycan and lipopolysaccharide in Gram-negative bacterial cell walls. (A) Representative *E. coli* PG architecture with a non-protein amino acid A$_2$pm. (B) Solid-state NMR spectra (bottom left) resolving the different amino acid composition in the PG stems of *E. coli* (Gram-negative) and two Gram-positive bacteria (*B. subtilis* and *S. aureus*).[549] Chain length, PG average thickness, ^{13}C$-T_1$ relaxation, and cross-linking were compared across the three species (right). The PG layer can be resolved from the outer membrane (OM) and plasma membrane (PM) using TEM (top left). Panel B is adapted with permission from refs 549 and 569. Copyright 2010 American Chemical Society and Copyright 1999 American Society for Microbiology. (C) LPS as another cell-wall component in Gram-negative bacteria. Its lipid A (bottom) and glycan (top) regions were assigned using ssNMR ^{13}C$-^{13}$C DARR spectra (right). This figure is adapted with permission from ref 570. Copyright 2018 American Society for Microbiology.

describe the remodeling process of ECMs in response to antibiotics or other bioactive molecules.

6.2. Bacterial Cell Architecture and Antibiotics

6.2.1. Structural Components of Bacterial Cell Walls.
Since the cell wall is a relatively rigid surface presenting many microscopic elevations, its ultrastructure has been examined by atomic force microscopy (AFM) and other imaging techniques. For example, AFM 3D reconstitution and other imaging techniques[550,551] have been used to identify the surface pores formed by loosely packed peptidoglycans (PGs) and make a comparison with the much denser material of the inner cell wall where polysaccharide strands are only apart by less than 7 nm (Figure 20A).[550] Such microscopic arrangements can be substantiated by the atomistic description of polymer structure and packing provided by ssNMR of extracts and even intact cells.

Bacterial cell walls are mainly made of PG, which contains a linear polymer of two alternating sugars: *N*-acetylglucosamine (GlcNAc or NAG) and *N*-acetylmuramic acid (MurNAc or NAM). NAM units from different chains are linked via short oligopeptide bridges (3−5 amino acids), creating a compact and strong material covering the bacteria surface. Variations exist in the bridge structure and the amino acid sequence of the stem (Figure 20B). For example, a penta-glycine bridge is present in *S. aureus* but absent in *Bacillus subtilis* where diaminopimelic acid (DAP), a non-protein amino acid, is found in the stem. Our current ssNMR methods for PG characterization are mainly designed for ^{13}C- and ^{15}N-labeled materials. However, the recent development of ultrafast MAS and ^{1}H detection might have paved the way for rapidly and cost-effectively investigating the structure of multi-gigadalton PGs using unlabeled bacterial cells (Figure 20C).[88]

The building blocks of PGs are synthesized on the external region of the cytoplasm and involve a precursor called lipid II—a lipid covalently linked with a disaccharide connected to a pentapeptide. It is therefore not surprising that lipid II also serves as a target of antimicrobial drugs.[554] To initiate PG building, from the inner membrane leaflet, lipid II is translocated outside of the cell by flipases, where the PG building blocks are progressively encapsulating the cell with the assistance of the well-known penicillin-binding proteins and other partners.[555−557]

PGs can be covalently bound to other cell-wall molecules. Depending on the bacteria species, they can bind to a polysaccharide capsule (the glycocalyx) or to the glycoprotein-rich S-layer (Figure 2).[558−561] In Gram-positive bacteria, the polyphosphate-rich LTA and wall teichoic acid (WTA) (Figure 20D) are associated with the thick PG layers (more than 30 layers corresponding to tens of nanometer thickness).[562] In Gram-negative strains, thinner PG sheets (less than 10 layers) are covered with an outer membrane made of O-glycosylated lipids called lipid-A, giving the well-known LPS.[2,563] These components make both types of assemblies harder for antibiotics to penetrate[564] and provide the mechanical properties needed for handling external and osmotic stresses and accommodating cell growth, communication, and multiplication.[565]

6.2.2. Investigations of Bacterial Cell Walls.
Simorre and colleagues have compared the organization, metal coordination, cross-linking, and flexibility of PGs across Gram-negative (*E. coli*) and Gram-positive (*B. subtilis* and *S. aureus*) strains.[219,549] In *E. coli* strains, a tetrapeptide is linked to the NAM residue of the PG with the sequence of D-Ala-X-D-Glu-L-Ala-MurNAc, where X is a non-protein amino acid (e.g., meso-A$_2$pm in many Gram-negative bacteria and mycobacteria) (Figure 21A).[30] This structural scheme differs notably from that of PGs in Gram-positive bacteria presented in Figure 20B. Overall, the dynamics in PG, associated with the degree of peptide cross-linking, is the highest in *S. aureus*, followed by *B. subtilis* and then *E. coli*

(Figure 21B). Therefore, *E. coli* has a thin PG made of short chains, with reduced cross-linking and therefore more pronounced dynamics.

The 3D arrangement of *S. aureus* PG has also been discussed for a long time, and ssNMR identified a 4-fold helical glycan symmetry that allows PG stems to organize into parallel and antiparallel orientations in the PG mesh.[566] In *S. aureus*, the PG architecture and the cell-wall morphology were found to be modulated by the variations in medium composition and growth stage, highlighting the plasticity of bacterial cell walls.[567] Based on high-resolution ssNMR data, Schanda et al. also proposed a model of PG complexed with a transpeptidase enzyme that is responsible for PG synthesis in *B. subtilis*.[568] Chemical shift perturbation was used to identify the region of interaction between this enzyme and PG.[568]

Gram-negative bacteria also have LPS that decorates the surface of the outer membrane.[571] This molecule is made of different sections, as shown in Figure 21C. Jachymek et al.[572] reported 1D ^{13}C/^{1}H HR-MAS and 2D HSQC/HMBC results, assisted by MALDI-TOF MS, to assign the glycan component of LPS. They showed that the O-glycan pattern of LPS called the antigen remains identical in different strains of the Gram-negative bacterium *Yokenella regensburgei*, even if the level and position of acetylation can vary. Simorre, Schanda, and co-workers applied ssNMR on extracted or reconstituted LPS endotoxin in *E. coli* and *P. aeruginosa*,[570] proving that the LPS O-antigen is the structural domain for interacting with antibiotic gentamicin (Figure 21C). Other components were also identified in this extract, mainly PGs or enzymes involved in PG synthesis found in the outer membrane.[573]

The negatively charged teichoic acids are crucial to surface adhesion and metal binding in Gram-positive strains.[574] ^{31}P ssNMR spectra and $T_{1\rho}$ relaxation have been used to detect the binding of the LTA to different surfaces. For example, the LTA from *S. aureus* could use its glucosamine and alanine groups to bind PGs and the solid surface, respectively.[575,576] This organization can help localize water molecules between the PG and the surface. At high metal concentrations, ^{31}P chemical shift anisotropy (CSA) data suggested a bidentate coordination model for both *S. aureus* LTA and *B. subtilis* WTA with magnesium.[552] However, at a low concentration of metal, ^{111}Cd−^{31}P distances measured by REDOR experiments suggested inequivalent monodentate P−Cd interactions that lead to a linear Cd−P−Cd arrangement.[577]

Notably, cell-associated components such as the lipoproteins found in *E. coli* cell envelopes have also been studied by ssNMR.[578] Using mostly INEPT-based methods, they examined the structure of the recombinant outer membrane protein (PagL) and other inner components of the cell envelope such as lipids, PGs, and lipoproteins. They emphasized the effect of the surrounding compartment on the molecular arrangement of PagL and established ssNMR protocols for investigating cell-associated molecules.

Nordmark et al. identified exopolysaccharides and acidic polysaccharides from *Pseudoalteromonas aliena* cell walls.[579] Using ^{13}C and ^{31}P ssNMR, Bui et al. have examined *Streptococcus pneumoniae*, revealing glycan chains with approximately 25 disaccharide units in the water-insoluble fraction (probably from PG fractions). ^{31}P resonances allowed the assignment of WTA ribitol and phosphocholine lipid head groups, while 2D ^{13}C ssNMR assigned protein side chains and resolved glycan configurations.[580] The structure of the S-layer was also examined, which was found to be sensitive to the temperature and pH.[581]

Many studies used HR-MAS methods to examine oligosaccharides in the bacterial cell-wall assembly. For example, signals of arabinogalactan (AG) and lipoarabinomannan (LAM) were assigned using ^{1}H−^{13}C HR-MAS HSQC and 3D HCCH-TOCSY experiments. Also, a bottom-up approach was used to reconstitute the signals, where the spectra of a whole-cell sample were reconstructed from the signals of isolated fractions.[582] 2D and 3D HR-MAS methods were also used to monitor the cell composition and characterize the abundant osmoregulated periplasmic glucans in *Ralstonia solanacearum*.[583,584]

6.2.3. Interactions of Peptidoglycans and Other Molecules with Antimicrobial Agents.
Schaefer, Cegelski, Kim, and colleagues have immensely contributed to the development of ssNMR methods, involving the versatile use of ^{15}N, ^{13}C, ^{19}F, and ^{31}P nuclei in the REDOR technique to understand the bacterial cell-wall and biofilm architecture as well as the effects of antibiotics.[548,585−588] The modes of action of many different antibiotics have been examined, including lipoglycopeptides such as vancomycin and its derivatives.[548,585−588] In these studies, bacteria were typically labeled using site-specifically labeled ^{13}C-alanine and ^{15}N-glycine or ^{13}C-glycine and ^{15}N-lysine and treated with specifically ^{19}F-labeled antibiotics, thus enabling the use of the REDOR pulse sequence for probing PG structure and drug binding.[585,587,589] For example, a vancomycin derivative named amphomycin was found to cause thinner cell walls in *S. aureus*.[590] Also, the observed inhibition of WTA synthesis is consistent with Park's nucleotide accumulation. The added lipoglycopeptide binds the mature PG template to reduce the cross-linking in the cell walls and deconstruct the PG template.[566,591] Fighting against resistance, another derivative (DFPBV) was found to use its hydrophobic side chain to stabilize the binding to PGs in a vancomycin-resistant strain of *S. aureus*.[592]

Similar approaches have been applied to *Enterococcus faecium* and were further coupled with LC/MS analysis.[587,593] MAS-DNP was also employed to detect interactions between antibiotics and lipid II *in situ*.[594] The mechanism of antibiotic resistance involving the cell walls of several bacteria such as *B. subtilis*, *S. aureus*, *E. coli*, and *Pseudomonas aeruginosa* has also been described.[88,549,568,595] In addition, antimicrobial peptides (AMPs) often interact with the PG and other cell-wall components, although they are not the final target of AMPs. AMPs, such as the human cationic polypeptide ECP, have been proved to interact strongly with the PG layer and indirectly interfere with cell replication by interacting with genetic materials.[596−598]

6.3. The Biofilm: An Organized Complex Supporting Bacterial Communities

6.3.1. The Formation of Biofilms.
Biofilms ensure a safe environment in which bacterial communities can cooperate (such as synergistic microconsortia), evolve, and resist chemical and physiological reactions. The density of cells in these communities is high, ranging from 10^8 to 10^{10} cells/g of biofilm,[599] with possible mixing of different species. To form biofilms, microorganisms need to switch from individual cells (planktonic) to a multicellular form (sessile) where micro-colonies can be clustered.[600] This process involves several metabolism transitions[601,602] and leads to the production of very different biofilms. For example, to protect the internal material of bacteria from desiccation, *E. coli* and *B. subtilis* can form a dry
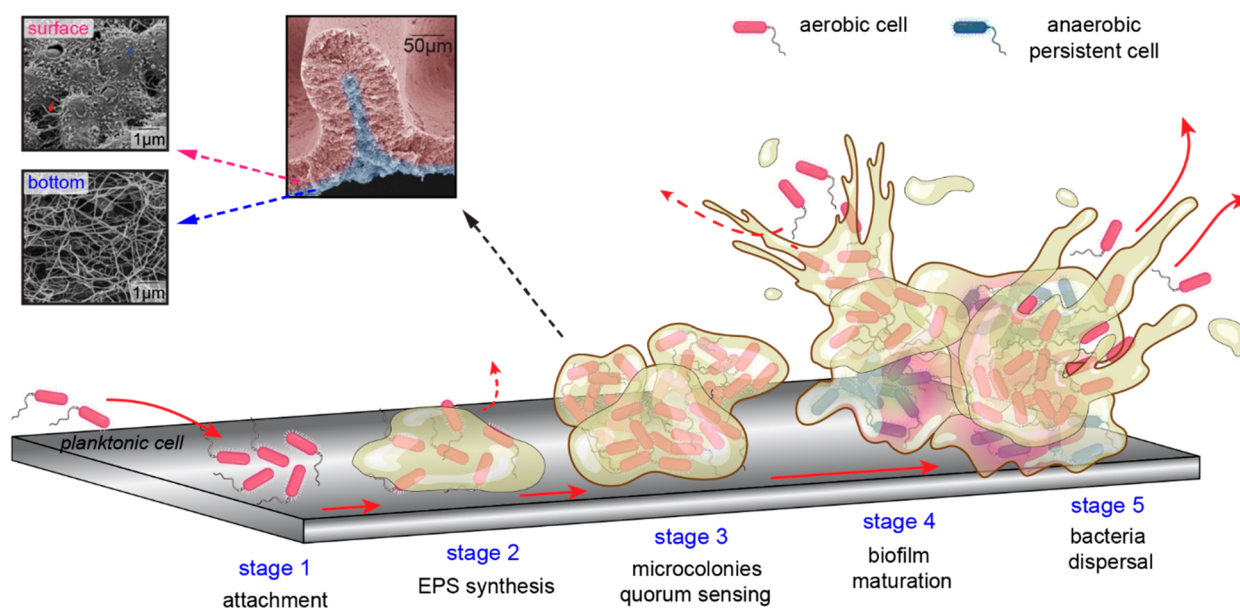
Figure 22. Schematic model of biofilm formation and maturation. Cells in solution first attach to a surface (stage 1) where it will grow (stage 2) and produce EPS if conditions are favorable (stage 3). The bacteria microcolonies will mature (stage 3) and slowly develop a complex communication system through the organized, spatially heterogeneous, and multilayered cell biofilm (stage 4). Bacteria colonies can then be released and dispersed in the medium to colonize other space and repeat the cycle (stage 5). Representative SEM images of biofilms are also shown. Colorized low-magnification perspective view SEM image of the *E. coli* macrocolony. Higher magnification showed that the biofilm consists of bacteria covered with cellulose and curli fibers on the surface (magenta), while all of the bacteria flagella form a dense mesh at the bottom (blue). SEM images are taken from Serra et al.[603] The SEM images are adapted with permission from ref 603. Copyright 2013 American Society for Microbiology.
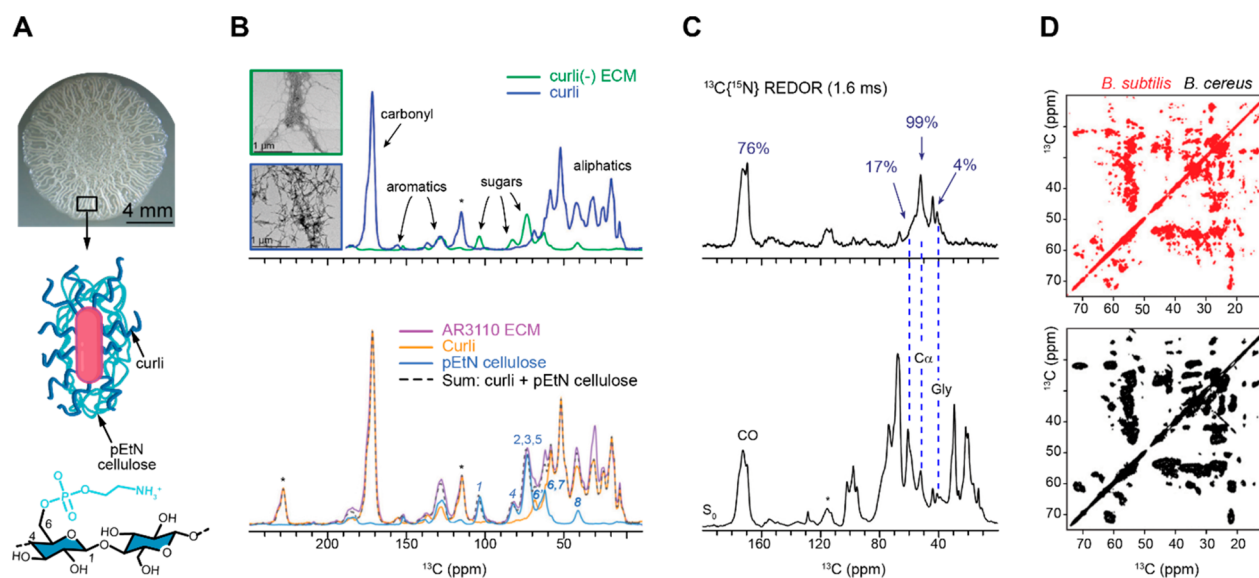
Figure 23. Investigations of bacterial biofilms by ssNMR. (A) *E. coli* growing on YESCA nutrient agar has a biofilm with the hallmark wrinkled colony morphology. Phosphoethanolamine (pEtN) cellulose enhances the adhesion of *E. coli* on surfaces and also packs with curli amyloid. Panel A is adapted with permission from ref 620. Copyright 2015 Elsevier. (B) *E. coli* biofilm mutants monitored by TEM and ssNMR[621] (top). Reconstitution of whole-cell spectra from the individual spectra collected on cell extracts (curli or pEtN cellulose) to enable compositional analysis with a bottom-up approach (bottom). Panel B is adapted with permission from refs 621 and 622. Copyright 2013 Elsevier and Copyright 2021 John Wiley and Sons. (C) $^{13}C\{^{15}N\}$ REDOR spectrum (top) of *Vibrio cholerae* specifically detecting the one-bond C−N pairs, allowing simplification over the control spectrum (bottom). The selected signals are from the carbon alpha of amino acids, phospholipids, or glycine modified from lipid A. Panel C is adapted with permission from ref 623. Copyright 2015 Elsevier. (D) Amyloid component of *Bacillus* biofilm investigated using 50 ms PDSD spectra, differentiating TasA proteins from *B. cereus* (black) and *B. subtilis* (red). Panel D is adapted with permission from ref 624. Copyright 2019 John Wiley and Sons.

surface layer,[603,604] while *P. aeruginosa* produces a liquid-crystal sponge structure to maintain internal moisture.[605]

Biofilm formation can be divided into five main stages, through which it becomes progressively more differentiated and more strongly attached to the surface (Figure 22).[606,607] First,

individual planktonic cells settle and adhere to a substrate. Then, under favorable conditions, bacteria are still capable of some motion using pilus motility and start secreting EPS, resulting in more tightly attached cells to their substrate. Third, the biofilm maturation begins: microcolonies start to appear, connected

through water channels that allow communication, nutrient flow, transversal gene exchange, and quorum sensing.[608] Simultaneously, bacteria are creating a multilayered assembly and a heterogeneous matrix with gradients of small molecules or oxygen availability between the cells' surface and interior.[609] Stage four consists of a mature biofilm where many coherent layers of cells form a 3D assembly. *Quorum sensing* orchestrates the overall biofilm development, mainly using water channels that irrigate the colonies. Lastly, microcolonies from the biofilm—that can be 50 (aerobic) to 400 (anaerobic) μm thick[610]—are released in the medium to colonize other surfaces and start a new biofilm when physiological conditions are optimal, for example, when an excess of nutrients is available.[611]

For a long time, ssNMR methods, together with EM, AFM, and solution NMR techniques, have been combined to address the composition and architecture of mature biofilms, to understand the transition between the single cell and the community, and to identify the response to antibiotics.

6.3.2. Determination of the Composition and Architecture of Biofilms.
Biofilms are made of cells immobilized in EPS made of proteins, polysaccharides, lipids, and nucleic acids. The EPS is the backbone of a biofilm.[612] It provides mechanical stability and has a significant role in retaining water, absorbing nutrients, and protecting from external stress. Water represents up to 97% of the biofilm material, while polysaccharides (including modified cellulose), proteins (including enzymes and curli amyloids), DNA, and lipids each represents only 1−2% or less.[613]

Despite their biomedical significance, there are few reliable quantitative methods to determine the composition and structure of a biofilm matrix.[547] Quantitative analyses of EPS are typically achieved using HPLC and MS methods, while Fourier transform infrared (FTIR) and Raman spectroscopy can qualitatively probe their chemical composition. Interactions and affinity of EPS with other molecules have been probed with surface plasmon resonance and small-angle X-ray scattering, while spatial architecture can be imaged using confocal scanning light, electron, or atomic force microscopy. Solution NMR studies of soluble extracts were used to quantify the metabolites present in the biofilm.[614] The interactions between EPS and cerium oxide nanoparticles have been examined by ^{31}P NMR, since these particles create metabolic stress that leads to phosphorus ejection.[615] Phosphorus integration was also monitored as a function of temperature and oxygen availability by detecting DNA and poly/pyro-phosphate within the EPS.[616] Unfortunately, extraction and purification procedures, such as filtration, heating, blending, and sonication, are often required when characterizing biofilms, which might perturb the structure and state of the biomaterial.[617−619]

The biofilm of *E. coli* contains curli functional amyloid fibrils and phosphoethanolamine (pEtN) cellulose, as shown by ssNMR (Figure 23A).[625,626] This intriguing type of cellulose has initially been described by Cegelski and colleagues using a combination of ssNMR and EM imaging (refs 19, 547, 548, 620, 621, 625, 627, and 628). This modified cellulose is key to the formation of long cellulose chains and helps the biofilm packing. This likely confers resistance of this biofilm to cellulose-degrading enzymes and might prevent amyloid curli fibers from overstimulating an immune response when invading a living organism. The fractions of cellulose and amyloids in whole-cell samples of *E. coli* were also examined using ssNMR in combination with EM and biochemical titration. Inhibition of curli synthesis led to the production of a purely cellulosic biofilm

(top of Figure 23B).[621] Later, Jeffries et al.[622] employed ^{13}C ssNMR to assign, quantify, and characterize both the cellulose and curli amyloids from biofilms of several strains of *E. coli* (bottom of Figure 23B). They proposed that curli amyloids were associated with adhesion, while pEtN cellulose favors cohesion. They also studied how biofilm formation could be affected by the surface where bacteria settle, and the data revealed that curli became dominant in the biofilm formed on a plastic surface. Other groups also reported interactions between amyloidogenic fragments and the cell surface during the bacteria virulence phase.[629−631]

^{13}C−CP along with REDOR methods involving ^{13}C, ^{15}N, ^{31}P, and ^{19}F nuclei were applied to another biofilm extracted from *Vibrio cholerae*[623] (Figure 23C). A top-down approach was used to describe the complex carbon pool of this bacterium, with quantification of the carbohydrates (58%), lipids (33%), and proteins (9%). They observed many amine moieties originating from the lysine side chains and phospholipids and from molecular modification of the free amine groups associated with glucosamine, as shown by the REDOR results. They also described possible modifications of amino acids and lipids that can be glycosylated when involved in cell walls.

Biofilms in *P. aeruginosa* are mainly composed of alginate, a polysaccharide made of 1,4-linked α-guluronate and β-mannuronate residues, with acetyl groups on the mannuronate residues. The T_1 relaxation and spectral lineshapes of the EPS isolated from *P. aeruginosa* have been monitored using ^{13}C ssNMR, which has revealed two different mechanisms for binding of Ca^{2+} and Mg^{2+}: calcium ions would create a specifically chelated complex with mannuronate−guluronate blocks in alginate, while the binding of magnesium is much weaker and nonspecific.[632] Lithium chloride was also found to strongly interact with alginate of the cell external matrix.[633] Mobility measurements using relaxometry revealed a very mobile assembly, where alginate undergoes molecular tumbling comparable to molecules in solution.

Bacillus subtilis is another important bacterium, studied by Loquet and co-workers, with exopolysaccharides, hydrophobins, and several functional amyloid proteins identified. A recent model proposed that a major protein called TasA is surrounded by polysaccharides in the biofilm. The TasA protein is a soluble monomer with different oligomers characterized by X-ray, EM, and solution NMR. Surprisingly, ssNMR on live biofilms gave different structural insights. Once in biofilms, the TasA protein has only one form that is protease-resistant with several β-sheet fibrils.[634] El Mammeri et al. also characterized the structure of functional amyloids in both *B. subtilis* and *B. cereus* (Figure 23D).[624] Their data revealed both β-sheet and α-helical conformations in the TasA protein, consistent with the functional amyloid structure that is different from the commonly reported β-sheet disease-associated amyloids. Although these two *Bacillus* bacteria shared a largely conserved TasA architecture, minor differences were detected using ssNMR and FTIR in terms of conformation and polymorphism. The data also led to a model where the two bacteria have different synthesis pathways for biofilm amyloids.[624]

6.3.3. Metabolism Flexibility and Remodeling of Biofilm in Response to Stress.
Solid-state NMR has been used to describe the viscoelasticity of the biofilm under different conditions including sublethal concentrations of vitamin C or inactivation of the *eps* operon responsible for EPS synthesis.[635] Jiao et al.[636] reported the use of FTIR, MS, and ssNMR, among others, to characterize the EPS of bacteria found in acid mine

drainage and proved that the growth stage affects the EPS composition. They showed that mature biofilms have more carbohydrates and metals but fewer proteins and almost no DNA. The insufficient resolution could not differentiate β-O-4 and β-O-3 linkages, which are important in PG, but the problem was partially resolved in another study using extracted material from *V. cholerae*.[623] It was also shown that DMSO in the growth media enhances the amount of curli amyloids in *E. coli* biofilm.[637]

Interestingly, magnetic resonance imaging (MRI) methods have been employed to investigate bacterial biofilms. Using high-resolution spectroscopy/microscopy, with MRI combined to confocal laser scanning microscopy (NMR/CLSM), McLean et al.[638] managed to build a 3D model of the biofilms of *Shewanella oneidensis* strain and *Streptococcus* mutants, which are associated with dissimilatory metal-reduction and caries disease, respectively. NMR and MRI techniques have also been employed to study biofilms in porous environments and flow cells to investigate water dynamics and biofilm expansion on various time and length scales. For example, ^{1}H T_2 and velocity MRI imaging were used in porous media that can be invaded by biofilms, which gave information with spatiotemporal resolution on this kind of assembly. This can be applied to mass transfer and flow abnormalities in porous materials.[639]

Caudill et al. used ssNMR to examine the interactions of biofilms with external molecules.[640,641] Using ^{31}P and ^{13}C ssNMR, they showed that gold nanoparticles decorated with cationic branched polyethylenimines interact electrostatically with biofilms and form hydrogen bonds with the oxygen atoms of phosphate groups of the teichoic acid residues in LPS. Such interactions will be altered by variation in teichoic acid composition (modification of the glucose or alanine quantities in LPS), suggesting the important function of these moieties.

Magnetic resonance techniques were also used to reveal the function of biofilms in preventing invasion of other bacterial species. MRI and ssNMR data on *B. subtilis* mutants showed that the absence of EPS in this bacterium leads to the production of less dense colonies, thus favoring the invasion by *Pseudomonas chlororaphis*.[642] Transcriptomics and genomics helped identify the main participants of the interactions between these two bacteria: a lipopeptide surfactin in *B. subtilis* and T6SS components in *P. chlororaphis*. This interaction between the two bacteria has also been monitored on melon leaves and seeds to understand the molecular phenomena orchestrating the concomitant invasion of both bacteria on plant materials.

Righi et al. used HR-MAS and transcriptomics to describe the metabolomics of biofilm, assigning and quantifying several amino acids and comparing biofilms before and after treatment by 2-aminoacetophenone.[643] Solution NMR has been used to characterize other soluble fractions and monitor metabolites in medically relevant bacterial biofilms.[546] Although with improved resolution compared to ssNMR, 1D ^{1}H HR-MAS spectra were still insufficient for differentiating *P. aeruginosa* biofilms or planktonic cells using PCA analysis.[644]

6.4. Other Bacterial Parts Exposed to the Medium

Other appendices can be found on the surface of bacterial cells. These extracellular assemblies include flagella, fimbriae, needles, and pili, which are essential for bacterial infection and adhesion. Associated with cell motility, the cytoplasmic protein FliK is the main protein of flagella. Solution NMR experiments[645] showed that FliK is mainly a disordered protein in which only the C- and N-termini are structured. The needles in *P. aeruginosa* have been

examined by ^{13}C ssNMR.[646] As for pili, they have rod-like polymeric structures and can be categorized by the secretion and adherence mechanisms: type I for surface attachment that can be associated with adhesion,[647] type III for secretion of toxin outside of the cytoplasm, and type IV for another kind of secretion and attachment system. The type II secretion system is often associated with toxins, degradative enzymes, proteases, or lipases.[648] Unfortunately, the pilus secretion has only been reported in a few NMR publications, such as the work of López-Castilla et al., which used solution NMR to examine interactions between calcium and the type II secretion system from *Klebsiella oxytoca*.[649] NMR combined with other techniques, such as X-ray, provided information on the orientation and structure of these extracellular protein assemblies.[650,651] The type I helical pilus in *E. coli* was characterized using ssNMR, detailing the interfaces between their FimA subunits.[652] Similar approaches were also used to characterize other extracellular fractions, such as the type III secretion systems purified from different strains including *Salmonella*.[646,653−656]

6.5. Probing the Cell Surface Using DNP

Starting from 2012, MAS-DNP has been applied by Baldus, Hediger, Simorre, and others[219,657] to investigate *E. coli* and *B. subtilis*. It was shown that radicals tend to accumulate in the cell wall, therefore improving the signal of the cell envelope only and simplifying the overall spectra. Nevertheless, internal elements seemed to be detected to some extent, including RNAs by ^{15}N or lipids by ^{13}C approaches. The preferential partitioning and nonuniform distribution of radicals in bacterial cell walls are probably attributable to their strong interactions with the PG layer likely via hydrogen bonding. On the contrary, the carbohydrate-dominant cell walls of plants typically have uniform polarization under MAS-DNP, as evidenced by identical spectral patterns with and without microwave irradiation.[221] In bacteria, PG signals can be selectively increased or suppressed in a whole-cell sample by changing the radical concentration. This selectivity allows for specifically monitoring certain components of interest using intact bacterial cells.

7. CONCLUDING REMARKS AND PERSPECTIVES

Undoubtedly, ssNMR has demonstrated its unique capability to investigate carbohydrates and associated biomolecules from the ECM materials (including cell walls) in physically relevant and chemically unperturbed states. Spanning across the plants, fungi, algae, and bacteria, the identified structural principles underlying the construction of ECMs should guide the development of technology for better using their constituent molecules for the production of biofuel, functionalized materials, nutrition, and high-value bioproducts. In-depth knowledge of microbial cell walls also serves as the basis for developing efficient antibiotics and antifungals.

Despite the recent landmark studies highlighted in this review, many structural aspects of ECMs remain unexplored, as discussed in previous sections. There are promising opportunities in the characterization of algal cell walls (section 5.1) and plant secondary cell walls (section 3.4), the supramolecular organization of which have not been extensively investigated using ssNMR. High-resolution methods need to be developed to analyze the lignin structure, quantify molecular composition, and screen unlabeled materials (section 3.5). ssNMR could also emerge as a standard strategy for assessing the action mechanism of antifungal drugs and antibiotics on bacteria or fungi, especially

for those compounds targeting the ECM components (section 4.7).

Projecting forward, numerous grand challenges are awaiting our efforts. What computational, statistical, and machine learning techniques should we use to promptly convert ssNMR observables to averaged structures of polymer complexes? Are we prepared for high-throughput and automatic analyses of unlabeled ECMs and carbohydrate-rich biomaterials? Could we obtain high-resolution views of the sugar components in mammalian and human cells?[81,658] How should we handle cellular mixtures like the communication and interface between microbes and plants/humans? When could we completely get rid of isotope labeling? The recent development of high- and ultrahigh-field magnets, ssNMR cryoprobes, MAS-DNP approaches and biradicals, proton detection in solids, and database-oriented tools might be the key to addressing these questions. Uniquely placed in this rapidly evolving era of ssNMR and DNP technology, we are eager to explore the many under-investigated research directions related to ECMs and cellular carbohydrates.

AUTHOR INFORMATION

Corresponding Author

Tuo Wang — *Department of Chemistry, Louisiana State University, Baton Rouge, Louisiana 70803, United States;* orcid.org/0000-0002-1801-924X; Email: tuowang@lsu.edu

Authors

Nader Ghassemi — *Department of Chemistry, Louisiana State University, Baton Rouge, Louisiana 70803, United States*

Alexandre Poulhazan — *Department of Chemistry, Louisiana State University, Baton Rouge, Louisiana 70803, United States; Department of Chemistry, Université du Québec à Montréal, Montreal H2X 2J6, Canada;* orcid.org/0000-0001-5217-5070

Fabien Deligey — *Department of Chemistry, Louisiana State University, Baton Rouge, Louisiana 70803, United States*

Frederic Mentink-Vigier — *National High Magnetic Field Laboratory, Tallahassee, Florida 32310, United States;* orcid.org/0000-0002-3570-9787

Isabelle Marcotte — *Department of Chemistry, Université du Québec à Montréal, Montreal H2X 2J6, Canada;* orcid.org/0000-0001-7467-7119

Complete contact information is available at:
https://pubs.acs.org/10.1021/acs.chemrev.1c00669

Author Contributions

N.G. and A.P. contributed equally. The manuscript was written through the contributions of all authors.

Notes

The authors declare no competing financial interest.

Biographies

Nader Ghassemi obtained his B.S. (2011) and M.Sc. (2013) degrees in Physics from Sharif University of Technology, Iran. In 2020, he received his Ph.D. degree in Physics under the supervision of Dr. Joseph Ross at Texas A&M University where his research was focused on applying NMR spectroscopy to study electronic materials. Shortly after, he joined Dr. Tuo Wang's group at Louisiana State University as a postdoctoral researcher. His current research focuses on applying ssNMR to understand cell-wall structure in biological systems.

Alexandre Poulhazan obtained a double diploma from AgroParisTech and the Pierre and Marie Curie University in Paris in 2017. After a 6-month internship at the University of Melbourne where he studied antimicrobial peptide synergy by ssNMR, he became a biochemistry Ph.D. candidate at the Université du Québec à Montréal under the supervision of Drs. Isabelle Marcotte and Dror Warschawski. His research focuses on *in situ* ssNMR studies of microalgae and other systems such as velvet worm slime and carbon dots. In 2020, he had a 6-month visit at Louisiana State University (Dr. Tuo Wang) to collaborate on the characterization of microalgae cells and extracts.

Fabien Deligey received his Ph.D. degree in 2019 from Université de Lorraine. Under the supervision of Drs. Bouguet-Bonnet and Gansmüller, he characterized nanosystems engineered for drug delivery with solid-state NMR. Since 2020, he has been a postdoctoral associate in Dr. Tuo Wang's group at Louisiana State University, where he is investigating plant-based biomaterials under natural-abundance DNP methods.

Frederic Mentink-Vigier received his M.Sc. in 2008 and Ph.D. in 2011 from Ecole Nationale Supérieure de Chimie ParisTech, France, under the supervision of Dr. L. Binet, working on paramagnetic materials for quantum computing. He undertook two postdoctoral stays, first at the Weizmann Institute, Israel, with Drs. D. Goldfarb and S. Vega and then back in France at CEA Grenoble (Dr. Gaël De Paëpe). In 2016, he joined the National High Magnetic Field Laboratory as a research faculty to continue his research in MAS-DNP and high-field EPR methodology, which includes the design of new radicals using numerical simulations.

Isabelle Marcotte obtained her M.Sc. in chemistry at the Université de Montréal in Canada and Ph.D. at the Université Laval (with Dr. Michèle Auger) in 2003. She did her postdoctoral research on spider silk at the ETH-Zurich in Switzerland between 2003 and 2006 (with Dr. Beat Meier). She came back to Canada in 2006 at the Université du Québec à Montréal (UQAM) in the Department of Chemistry as a faculty member. Since 2017, she has been serving as Associate-Dean of research of the faculty of sciences at UQAM. Her biomolecular research covers a large variety of systems including mussel byssus, model membranes, as well as living organisms such as red blood cells, bacteria, and microalgae.

Tuo Wang received his B.S. from Nankai University (China) in 2010 and started his graduate research at Iowa State University. He moved to Massachusetts Institute of Technology (MIT) in 2014 and received his Ph.D. in Physical Chemistry from MIT in 2016 under the supervision of Dr. Mei Hong. After doing his postdoctoral training in the Hong lab, he joined the Department of Chemistry at Louisiana State University as an assistant professor in 2017 and became an associate professor in 2021. His research focuses on the structural elucidation of carbohydrate-rich biosystems.

ABBREVIATIONS

AFM	atomic force microscope
AG	arabinogalactan
AmB	amphotericin B
AMP	antimicrobial peptide
AX	arabinoxylan
CBM	carbohydrate-binding module
CE	cross effect
CesA	cellulose synthase
CGMD	coarse-grained molecular dynamics
CLSM	confocal laser scanning microscopy
CMP-NMR	comprehensive multiphase NMR
CORD	combined $R2_n^v$-driven
CP	cross-polarization
CrI	crystallinity index
CSA	chemical shift anisotropy
cw	continuous wave
DARR	dipolar assisted rotational resonance
DD	dipolar decoupling
DFT	density-functional theory
DNP	dynamic nuclear polarization
DOPA	dihydroxyphenylalanine
DP	direct polarization
ECM	extracellular matrix
ECMs	extracellular matrixes
EPS	extracellular polymer substances
EXPB	β-expansin
FESEM	field emission scanning electron microscope
FTIR	Fourier transform infrared
GAG	galactosaminogalactan
GalA	galacturonic acid
GalXM	galactoxylomannan
GAX	glucuronoarabinoxylan
GGM	galactoglucomannan
GM	galactomannan
gt	gauche—trans
GXM	glucuronoxylomannan
HG	homogalacturonan
HRGP	hydroxyproline-rich glycoprotein
INADEQUATE	incredible natural-abundance double quantum transfer experiment
INEPT	insensitive nuclei enhanced by polarization transfer
LAM	lipoarabinomannan
LCPA	long chain polyamine
LDA	linear discriminant analysis
LPS	lipopolysaccharide
LTA	lipoteichoic acid
MAS	magic-angle spinning
MD	molecular dynamics
MLG	mixed-linkage glucan
NMR	nuclear magnetic resonance
OM	outer membrane
PA	polarizing agent
PAR	proton assisted recoupling
PARIS	phase-alternated recoupling irradiation scheme
PASS	phase-adjusted spinning sidebands
PCA	principal component analysis
PDSD	proton-driven spin diffusion
pEtN	phosphoethanolamine
PG	peptidoglycan
PM	plasma membrane
PRE	paramagnetic relaxation enhancement
PPs	polyisoprenoids
REDOR	rotational echo double-resonance
RFDR	radiofrequency-driven dipolar recoupling
RG-I	rhamnogalacturonan-I
Rha	rhamnose
SDV	silica deposit vesicle
SE	solid effect
SEs	sterol esters
SFG	sum frequency generation
S/N	signal-to-noise
ssNMR	solid-state nuclear magnetic resonance
TEM	transmission electron microscopy
TGs	triglycerides
tg	trans—gauche
TSAR	third-spin assisted recoupling
WTA	wall teichoic acids
XyG	xyloglucan

REFERENCES

(1) Cosgrove, D. J. Growth of the plant cell wall. *Nat. Rev. Mol. Cell Biol.* **2005**, *6*, 850−961.

(2) Silhavy, T. J.; Kahne, D.; Walker, S. The bacterial cell envelope. *Cold Spring Harbor Perspect. Biol.* **2010**, *2*, a000414.

(3) Latgé, J.-P. The cell wall: a carbohydrate armour for the fungal cell. *Mol. Microbiol.* **2007**, *66*, 279−290.

(4) Domozych, D. S.; Ciancia, M.; Fangel, J. U.; Mikkelsen, M. D.; Ulvskov, P.; Willats, W. G. T. The cell walls of green algae: a journey through evolution and diversity. *Front. Plant Sci.* **2012**, *3*, 82−82.

(5) Brown, G. D.; Denning, D. W.; Gow, N. A. R.; Levitz, S. M.; Netea, M. G.; White, T. C. Hidden killers: human fungal infections. *Sci. Transl. Med.* **2012**, *4*, 165rv13.

(6) Roy, R.; Tiwari, M.; Donelli, G.; Tiwari, V. Strategies for combating bacterial biofilms: a focus on anti-biofilm agents and their mechanisms of action. *Virulence* **2018**, *9*, 522−554.

(7) Kohanski, M. A.; Dwyer, D. J.; Collins, J. J. How antibiotics kill bacteria: from targets to networks. *Nat. Rev. Microbiol.* **2010**, *8*, 423−435.

(8) York, W. S.; Darvill, A. G.; McNeil, M.; Stevenson, T. T.; Albersheim, P. Isolation and characterization of plant cell walls and cell wall components. *Methods Enzymol.* **1986**, *118*, 3−40.

(9) François, J. M. A simple method for quantitative determination of polysaccharides in fungal cell walls. *Nat. Protoc.* **2006**, *1*, 2995−3000.

(10) Mouille, G.; Robin, S.; Lecomte, M.; Pagant, S.; Höfte, H. Classification and identification of *Arabidopsis* cell wall mutants using Fourier-Transform InfraRed (FT-IR) microspectroscopy. *Plant J.* **2003**, *35*, 393−404.

(11) Martinez-Sanz, M.; Gidley, M. J.; Gilbert, E. P. Application of X-ray and neutron small angle scattering techniques to study the hierarchical structure of plant cell walls: A review. *Carbohydr. Polym.* **2015**, *125*, 120−134.

(12) Desmarais, S. M.; De Pedro, M. A.; Cava, F.; Huang, K. C. Peptidoglycan at its peaks: how chromatographic analyses can reveal bacterial cell wall structure and assembly. *Mol. Microbiol.* **2013**, *89*, 1−13.

(13) Reif, B.; Ashbrook, S. E.; Emsley, L.; Hong, M. Solid-state NMR spectroscopy. *Nat. Rev. Methods Primers* **2021**, *1*, 2.

(14) Mansfield, S. D.; Kim, H.; Lu, F.; Ralph, J. Whole plant cell wall characterization using solution-state 2D NMR. *Nat. Protoc.* **2012**, *7*, 1579−1589.

(15) Foston, M.; Samuel, R.; He, J.; Ragauskas, A. J. A review of whole cell wall NMR by the direct-dissolution of biomass. *Green Chem.* **2016**, *18*, 608−621.

(16) Zhao, W.; Fernando, L. D.; Kirui, A.; Deligey, F.; Wang, T. Solid-state NMR of plant and fungal cell walls: a critical review. *Solid State Nucl. Magn. Reson.* **2020**, *107*, 101660.

(17) Wang, T.; Phyo, P.; Hong, M. Multidimensional solid-state NMR spectroscopy of plant cell walls. *Solid State Nucl. Magn. Reson.* **2016**, *78*, 56−63.

(18) Kelly, J. E.; Chrissian, C.; Stark, R. E. Tailoring NMR experiments for structural characterization of amorphous biological solids: A practical guide. *Solid State Nucl. Magn. Reson.* **2020**, *109*, 101686.

(19) Reichhardt, C.; Cegelski, L. Solid-state NMR for bacterial biofilms. *Mol. Phys.* **2014**, *112*, 887−894.

(20) Poulhazan, A.; Arnold, A. A.; Warschawski, D. E.; Marcotte, I. Solid-state NMR study of microalgal membranes and cell walls. *Solid-State NMR*; IOP Publishing: 2020; pp 1−23.

(21) Rossini, A. J.; Zagdoun, A.; Lelli, M.; Lesage, A.; Copéret, C.; Emsley, L. Dynamic nuclear polarization surface enhanced NMR spectroscopy. *Acc. Chem. Res.* **2013**, *46*, 1942−1951.

(22) Corzilius, B. High-field dynamic nuclear polarization. *Annu. Rev. Phys. Chem.* **2020**, *71*, 143−170.

(23) Su, Y.; Andreas, L.; Griffin, R. G. Magic angle spinning NMR of proteins: high-frequency dynamic nuclear polarization and ^{1}H detection. *Annu. Rev. Biochem.* **2015**, *84*, 465−497.

(24) Gan, Z.; Hung, I.; Wang, X.; Paulino, J.; Wu, G.; Litvak, I. M.; Gor'kov, P. L.; Brey, W. W.; Lendi, P.; Schiano, J. L.; et al. NMR spectroscopy up to 35.2T using a series-connected hybrid magnet. *J. Magn. Reson.* **2017**, *284*, 125−136.

(25) Ciccarelli, F. D.; Doerks, T.; von Mering, C.; Creevey, C. J.; Snel, B.; Bork, P. Toward automatic reconstruction of a highly resolved tree of life. *Science* **2006**, *311*, 1283−1287.

(26) Letunic, I.; Bork, P. Interactive Tree Of Life (iTOL): an online tool for phylogenetic tree display and annotation. *Bioinformatics* **2007**, *23*, 127−128.

(27) Takahashi, H.; Lee, D.; Dubois, L.; Bardet, M.; Hediger, S.; De Paëpe, G. Rapid natural-abundance 2D ^{13}C−^{13}C correlation spectroscopy using dynamic nuclear polarization enhanced solid-state NMR and matrix-free sample preparation. *Angew. Chem., Int. Ed.* **2012**, *51*, 11766−11769.

(28) Zhou, D. H.; Shah, G.; Mullen, C.; Sandoz, D.; Rienstra, C. M. Proton-detected solid-state NMR spectroscopy of natural-abundance peptide and protein pharmaceuticals. *Angew. Chem., Int. Ed.* **2009**, *48*, 1253−1256.

(29) Sohlenkamp, C.; Geiger, O. Bacterial membrane lipids: diversity in structures and pathways. *FEMS Microbiol. Rev.* **2016**, *40*, 133−159.

(30) Vollmer, W.; Blanot, D.; De Pedro, M. A. Peptidoglycan structure and architecture. *FEMS Microbiol. Rev.* **2008**, *32*, 149−167.

(31) Li, B.; Webster, T. J. Bacteria antibiotic resistance: New challenges and opportunities for implant-associated orthopedic infections. *J. Orthop. Res.* **2018**, *36*, 22−32.

(32) Del Pozo, J.; Patel, R. The challenge of treating biofilm-associated bacterial infections. *Clin. Pharmacol. Ther.* **2007**, *82*, 204−209.

(33) Flemming, H.-C. Biofouling in water systems−cases, causes and countermeasures. *Appl. Microbiol. Biotechnol.* **2002**, *59*, 629−640.

(34) Hall-Stoodley, L.; Costerton, J. W.; Stoodley, P. Bacterial biofilms: from the natural environment to infectious diseases. *Nat. Rev. Microbiol.* **2004**, *2*, 95−108.

(35) Sand, W.; Gehrke, T. Extracellular polymeric substances mediate bioleaching/biocorrosion via interfacial processes involving iron(III) ions and acidophilic bacteria. *Res. Microbiol.* **2006**, *157*, 49−56.

(36) Benamara, H.; Rihouey, C.; Jouenne, T.; Alexandre, S. Impact of the biofilm mode of growth on the inner membrane phospholipid composition and lipid domains in *Pseudomonas aeruginosa*. *Biochim. Biophys. Acta, Biomembr.* **2011**, *1808*, 98−105.

(37) Armstrong-James, D.; Meintjes, G.; Brown, G. D. A neglected epidemic: fungal infections in HIV/AIDS. *Trends Microbiol.* **2014**, *22*, 120−127.

(38) Beardsley, J.; Halliday, C. L.; Chen, S. C.-A.; Sorrell, T. C. Responding to the emergence of antifungal drug resistance:

perspectives from the bench and the bedside. *Future Microbiol.* **2018**, *13*, 1175−1191.

(39) Fekkar, A.; Lampros, A.; Mayaux, J.; Poigon, C.; Demeret, S.; Constantin, J.-M.; Marcelin, A.-G.; Monsel, A.; Luyt, C.-E.; Blaize, M. Occurrence of invasive pulmonary fungal infections in patients with severe COVID-19 admitted to the ICU *Am. Am. J. Respir. Crit. Care Med.* **2021**, *203*, 307−317.

(40) Eades, C. P.; Armstrong-James, D. P. H. Invasive fungal infections in the immunocompromised host: Mechanistic insights in an era of changing immunotherapeutics. *Med. Mycol.* **2019**, *57*, S307−S317.

(41) Agustinho, D. P.; Miller, L. C.; Li, L. X.; Doering, T. L. Peeling the onion: the outer layers of *Cryptococcus neoformans*. *Mem. Inst. Oswaldo Cruz* **2018**, *113*, No. e180040.

(42) Gow, N. A. R.; Latge, J. P.; Munro, C. A. The fungal cell wall: structure, biosynthesis, and function. *Microbiol. Spectrum* **2017**, *5*, 1−25.

(43) Pazos, C.; Moragues, M.-D.; Quindós, G.; Pontón, J.; del Palacio, A. Diagnostic potential of (1→3)-β-D-glucan and anti-*Candida albicans* germ tube antibodies for the diagnosis and therapeutic monitoring of invasive candidiasis in neutropenic adult patients. *Rev. Iberoam. Micol.* **2006**, *23*, 209−215.

(44) Perlin, D. S. Mechanisms of echinocandin antifungal drug resistance. *Ann. N. Y. Acad. Sci.* **2015**, *1354*, 1−11.

(45) Denning, D. W. Echinocandin antifungal drugs. *Lancet* **2003**, *362*, 1142−1151.

(46) Erwig, L. P.; Gow, N. A. R. Interactions of fungal pathogens with phagocytes. *Nat. Rev. Microbiol.* **2016**, *14*, 163−176.

(47) Latgé, J.-P.; Beauvais, A.; Chamilos, G. The cell wall of the human fungal pathogen *Aspergillus fumigatus*: biosynthesis, organization, immune response, and virulence. *Annu. Rev. Microbiol.* **2017**, *71*, 99−116.

(48) Briard, B.; Fontaine, T.; Samir, P.; Place, D. E.; Muszkieta, L.; Malireddi, R. K. S.; Karki, R.; Christgen, S.; Bomme, P.; Vogel, P.; et al. Galactosaminogalactan activates the inflammasome to provide host protection. *Nature* **2020**, *588*, 688−692.

(49) Kang, X.; Kirui, A.; Muszynski, A.; Widanage, M. C. D.; Chen, A.; Azadi, P.; Wang, P.; Mentink-Vigier, F.; Wang, T. Molecular architecture of fungal cell walls revealed by solid-state NMR. *Nat. Commun.* **2018**, *9*, 2747.

(50) Chrissian, C.; Camacho, E.; Kelly, J. E.; Wang, H.; Casadevall, A.; Stark, R. E. Solid-state NMR spectroscopy identifies three classes of lipids in *Cryptococcus neoformans* melanized cell walls and whole fungal cells. *J. Biol. Chem.* **2020**, *295*, 15083−15096.

(51) Engel, A.; Shewmaker, F.; Edskes, H. K.; Dyda, F.; Wickner, R. B. Amyloid of the *Candida albicans* Ure2p prion domain is infectious and has an in-register parallel β-sheet structure. *Biochemistry* **2011**, *50*, 5971−5978.

(52) Fernando, L. D.; Zhao, W. C.; Widanage, M. C. D.; Mentink-Vigier, F.; Wang, T. Solid-state NMR and DNP investigations of carbohydrates and cell-wall biomaterials. *eMagRes* **2020**, *9*, 251−258.

(53) Lewis, L. A.; McCourt, R. M. Green algae and the origin of land plants. *Am. J. Bot.* **2004**, *91*, 1535−1556.

(54) LeDuff, P.; Rorrer, G. L. Formation of extracellular β-chitin nanofibers during batch cultivation of marine diatom *Cyclotella* sp. at silicon limitation. *J. Appl. Phycol.* **2019**, *31*, 3479−3490.

(55) Wustmann, M.; Poulsen, N.; Kröger, N.; van Pée, K.-H. Chitin synthase localization in the diatom *Thalassiosira pseudonana*. *BMC Materials* **2020**, *2*, 10.

(56) Kapaun, E.; Reisser, W. A chitin-like glycan in the cell wall of a *Chlorella* sp. *Planta* **1995**, *197*, 577−582.

(57) Lee, J.-H.; Waffenschmidt, S.; Small, L.; Goodenough, U. Between-species analysis of short-repeat modules in cell wall and sex-related hydroxyproline-rich glycoproteins of *Chlamydomonas*. *Plant Physiol.* **2007**, *144*, 1813−1826.

(58) Popper, Z. A.; Michel, G.; Hervé, C.; Domozych, D. S.; Willats, W. G.; Tuohy, M. G.; Kloareg, B.; Stengel, D. B. Evolution and diversity of plant cell walls: from algae to flowering plants. *Annu. Rev. Plant Biol.* **2011**, *62*, 567−590.

(59) Popper, Z. A. Evolution and diversity of green plant cell walls. *Curr. Opin. Plant Biol.* **2008**, *11*, 286−292.

(60) Höfte, H.; Voxeur, A. Plant cell walls. *Curr. Biol.* **2017**, *27*, R865−R870.

(61) Cosgrove, D. J. Plant cell wall extensibility: connecting plant cell growth with cell wall structure, mechanics, and the action of wall-modifying enzymes. *J. Exp. Bot.* **2016**, *67*, 463−476.

(62) Cosgrove, D. J. Diffuse growth of plant cell walls. *Plant Physiol.* **2018**, *176*, 16−27.

(63) Zhong, R.; Cui, D.; Ye, Z. H. Secondary cell wall biosynthesis. *New Phytol.* **2019**, *221*, 1703−1723.

(64) Somerville, C.; Bauer, S.; Brininstool, G.; Facette, M.; Hamann, T.; Milne, J.; Osborne, E.; Paredez, A.; Persson, S.; Raab, T. Toward a systems approach to understanding plant cell walls. *Science* **2004**, *306*, 2206−2211.

(65) Lampugnani, E. R.; Khan, G. A.; Somssich, M.; Persson, S. Building a plant cell wall at a glance. *J. Cell Sci.* **2018**, *131*, jcs207373.

(66) Petridis, L.; Smith, J. C. Molecular-level driving forces in lignocellulosic biomass deconstruction for bioenergy. *Nat. Rev. Chem.* **2018**, *2*, 382−389.

(67) Cosgrove, D. J.; Jarvis, M. C. Comparative structure and biomechanics of plant primary and secondary cell walls. *Front. Plant Sci.* **2012**, *3*, 204.

(68) Somerville, C.; Youngs, H.; Taylor, C.; Davis, S. C.; Long, S. P. Feedstocks for lignocellulosic biofuels. *Science* **2010**, *329*, 790−792.

(69) Carroll, A.; Somerville, C. Cellulosic biofuels. *Annu. Rev. Plant Biol.* **2009**, *60*, 165−182.

(70) Pauly, M.; Keegstra, K. Cell-wall carbohydrates and their modification as a resource for biofuels. *Plant J.* **2008**, *54*, 559−568.

(71) Levitt, M. *Spin dynamics: Basics of Nuclear Magnetic Resonance*, 2nd ed.; Wiley-Blackwell: 2008; pp 1−744.

(72) Schmidt-Rohr, K.; Spiess, H. W. *Multidimensional Solid-State NMR and Polymers*; Academic Press: San Diego, CA, 1994; pp 1−496.

(73) McDermott, A. E.; Polenova, T. *Solid state NMR studies of biopolymers*; John Wiley & Sons: 2010; pp 1−592.

(74) Warnet, X. L.; Arnold, A. A.; Marcotte, I.; Warschawski, D. E. In-cell solid-state NMR: an emerging technique for the study of biological membranes. *Biophys. J.* **2015**, *109*, 2461−2466.

(75) Sarou-Kanian, V.; Joudiou, N.; Louat, F.; Yon, M.; Szeremeta, F.; Meme, S.; Massiot, D.; Decoville, M.; Fayon, F.; Beloeil, J.-C. Metabolite localization in living drosophila using high resolution magic angle spinning NMR. *Sci. Rep.* **2015**, *5*, 9872.

(76) Zandomeneghi, G.; Ilg, K.; Aebi, M.; Meier, B. H. On-cell MAS NMR: physiological clues from living cells. *J. Am. Chem. Soc.* **2012**, *134*, 17513−17519.

(77) Warnet, X. L.; Laadhari, M.; Arnold, A. A.; Marcotte, I.; Warschawski, D. E. A ^{2}H magic-angle spinning solid-state NMR characterisation of lipid membranes in intact bacteria. *Biochim. Biophys. Acta, Biomembr.* **2016**, *1858*, 146−152.

(78) Ghosh, R.; Xiao, Y.; Kragelj, J.; Frederick, K. K. In-cell sensitivity-enhanced NMR of intact living mammalian cells. *J. Am. Chem. Soc.* **2021**, *143*, 18454.

(79) Poulhazan, A.; Arnold, A. A.; Warschawski, D. E.; Marcotte, I. Unambiguous *ex situ* and in cell 2D ^{13}C solid-state NMR character-ization of starch and its constituents. *Int. J. Mol. Sci.* **2018**, *19*, 3817.

(80) Kirui, A.; Dickwella Widanage, M. C.; Mentink-Vigier, F.; Wang, P.; Kang, X.; Wang, T. Preparation of fungal and plant materials for structural elucidation using dynamic nuclear polarization solid-state NMR. *J. Visualized Exp.* **2019**, No. e59152.

(81) Albert, B. J.; Gao, C.; Sesti, E. L.; Saliba, E. P.; Alaniva, N.; Scott, F. J.; Sigurdsson, S. T.; Barnes, A. B. Dynamic nuclear polarization nuclear magnetic resonance in human cells using fluorescent polarizing agents. *Biochemistry* **2018**, *57*, 4741−4746.

(82) Ehren, H. L.; Appels, F. V. W.; Houben, K.; Renault, M. A. M.; Wösten, H. A. B.; Baldus, M. Characterization of the cell wall of a mushroom forming fungus at atomic resolution using solid-state NMR spectroscopy. *Cell Surface* **2020**, *6*, 100046.

(83) Ghosh, R.; Kragelj, J.; Xiao, Y.; Frederick, K. K. Cryogenic sample loading into a magic angle spinning nuclear magnetic resonance

spectrometer that preserves cellular viability. *J. Visualized Exp.* **2020**, *163*, No. e61733.

(84) Laws, D. D.; Bitter, H. M. L.; Jerschow, A. Solid-state NMR spectroscopic methods in chemistry. *Angew. Chem., Int. Ed.* **2002**, *41*, 3096−3129.

(85) Damman, R.; Narasimhan, S.; Weingarth, M.; Baldus, M. Cellular solid-state NMR spectroscopy. *In-cell NMR spectroscopy: from molecular sciences to cell biology*; The Royal Society of Chemistry: 2020; pp 131−151.

(86) Gao, Y.; Mortimer, J. C. Unlocking the architecture of native plant cell walls via solid-state nuclear magnetic resonance. *Methods Cell Biol.* **2020**, *160*, 121−143.

(87) Sefzik, T. H.; Houseknecht, J. B.; Clark, T. M.; Prasad, S.; Lowary, T. L.; Gan, Z.; Grandinetti, P. J. Solid-state ^{17}O NMR in carbohydrates. *Chem. Phys. Lett.* **2007**, *434*, 312−315.

(88) Bougault, C.; Ayala, I.; Vollmer, W.; Simorre, J. P.; Schanda, P. Studying intact bacterial peptidoglycan by proton-detected NMR spectroscopy at 100 kHz MAS frequency. *J. Struct. Biol.* **2019**, *206*, 66−72.

(89) Phyo, P.; Hong, M. Fast MAS ^{1}H−^{13}C correlation NMR for structural investigations of plant cell walls. *J. Biomol. NMR* **2019**, *73*, 661−674.

(90) Haya, K.; Makino, Y.; Kikuchi-Kinoshita, A.; Kawamura, I.; Naito, A. ^{31}P and ^{13}C solid-state NMR analysis of morphological changes of phospholipid bilayers containing glucagon during fibril formation of glucagon under neutral condition. *Biochim. Biophys. Acta, Biomembr.* **2020**, *1862*, 183290.

(91) Molugu, T. R.; Lee, S.; Brown, M. F. Concepts and methods of solid-state NMR spectroscopy applied to biomembranes. *Chem. Rev.* **2017**, *117*, 12087−12132.

(92) Tardy-Laporte, C.; Arnold, A. A.; Genard, B.; Gastineau, R.; Morançais, M.; Mouget, J.-L.; Tremblay, R.; Marcotte, I. A 2H solid-state NMR study of the effect of antimicrobial agents on intact Escherichia coli without mutating. *Biochim. Biophys. Acta, Biomembr.* **2013**, *1828*, 614−622.

(93) Lu, M.; Sarkar, S.; Wang, M.; Kraus, J.; Fritz, M.; Quinn, C. M.; Bai, S.; Holmes, S. T.; Dybowski, C.; Yap, G. P. A.; et al. ^{19}F magic angle spinning NMR spectroscopy and density functional theory calculations of fluorosubstituted tryptophans: integrating experiment and theory for accurate determination of chemical shift tensors. *J. Phys. Chem. B* **2018**, *122*, 6148−6155.

(94) Lu, M.; Wang, M.; Sergeyev, I. V.; Quinn, C. M.; Struppe, J.; Rosay, M.; Maas, W.; Gronenborn, A. M.; Polenova, T. ^{19}F dynamic nuclear polarization at fast magic angle spinning for NMR of HIV-1 capsid protein assemblies. *J. Am. Chem. Soc.* **2019**, *141*, 5681−5691.

(95) Lane Gilchrist, M.; Monde, K.; Tomita, Y.; Iwashita, T.; Nakanishi, K.; McDermott, A. E. Measurement of interfluorine distances in solids. *J. Magn. Reson.* **2001**, *152*, 1−6.

(96) Roos, M.; Wang, T.; Shcherbakov, A. A.; Hong, M. Fast magic-angle-spinning ^{19}F spin exchange NMR for determining nanometer ^{19}F−^{19}F distances in proteins and pharmaceutical compounds. *J. Phys. Chem. B* **2018**, *122*, 2900−2911.

(97) Gelenter, M. D.; Wang, T.; Liao, S.-Y.; O'Neill, H.; Hong, M. ^{2}H−^{13}C correlation solid-state NMR for investigating dynamics and water accessibilities of proteins and carbohydrates. *J. Biomol. NMR* **2017**, *68*, 257−270.

(98) Nishiyama, Y. Fast magic-angle sample spinning solid-state NMR at 60−100 kHz for natural abundance samples. *Solid State Nucl. Magn. Reson.* **2016**, *78*, 24−36.

(99) Andrew, E. R.; Bradbury, A.; Eades, R. G. Nuclear magnetic resonance spectra from a crystal rotated at high speed. *Nature* **1958**, *182*, 1659−1659.

(100) Lowe, I. J. Free induction decays of rotating solids. *Phys. Rev. Lett.* **1959**, *2*, 285−287.

(101) Andreas, L. B.; Jaudzems, K.; Stanek, J.; Lalli, D.; Bertarello, A.; Le Marchand, T.; Cala-De Paepe, D.; Kotelovica, S.; Akopjana, I.; Knott, B.; et al. Structure of fully protonated proteins by proton-detected magic-angle spinning NMR. *Proc. Natl. Acad. Sci. U. S. A.* **2016**, *113*, 9187−9192.

(102) Struppe, J.; Quinn, C. M.; Lu, M.; Wang, M.; Hou, G.; Lu, X.; Kraus, J.; Andreas, L. B.; Stanek, J.; Lalli, D.; et al. Expanding the horizons for structural analysis of fully protonated protein assemblies by NMR spectroscopy at MAS frequencies above 100 kHz. *Solid State Nucl. Magn. Reson.* **2017**, *87*, 117−125.

(103) Zhang, R.; Mroue, K. H.; Ramamoorthy, A. Proton-based ultrafast magic angle spinning solid-state NMR spectroscopy. *Acc. Chem. Res.* **2017**, *50*, 1105−1113.

(104) Ishii, Y.; Tycko, R. Sensitivity enhancement in solid state ^{15}N NMR by indirect detection with high-speed magic angle spinning. *J. Magn. Reson.* **2000**, *142*, 199−204.

(105) Webb, A. Increasing the sensitivity of magnetic resonance spectroscopy and imaging. *Anal. Chem.* **2012**, *84*, 9−16.

(106) Elena, B.; Lesage, A.; Steuernagel, S.; Böckmann, A.; Emsley, L. Proton to carbon-13 INEPT in solid-state NMR spectroscopy. *J. Am. Chem. Soc.* **2005**, *127*, 17296−17302.

(107) Kolodziejski, W.; Klinowski, J. Kinetics of cross-polarization in solid-state NMR: a guide for chemists. *Chem. Rev.* **2002**, *102*, 613−628.

(108) Johnson, R. L.; Schmidt-Rohr, K. Quantitative solid-state ^{13}C NMR with signal enhancement by multiple cross polarization. *J. Magn. Reson.* **2014**, *239*, 44−49.

(109) Duan, P.; Schmidt-Rohr, K. Composite-pulse and partially dipolar dephased multiCP for improved quantitative solid-state 13C NMR. *J. Magn. Reson.* **2017**, *285*, 68−78.

(110) Cadars, S.; Lesage, A.; Emsley, L. Chemical shift correlations in disordered solids. *J. Am. Chem. Soc.* **2005**, *127*, 4466−4476.

(111) Cadars, S.; Sein, J.; Duma, L.; Lesage, A.; Pham, T. N.; Baltisberger, J. H.; Brown, S. P.; Emsley, L. The refocused INADEQUATE MAS NMR experiment in multiple spin-systems: Interpreting observed correlation peaks and optimizing lineshapes. *J. Magn. Reson.* **2007**, *188*, 24−34.

(112) Chen, L.; Kaiser, J. M.; Lai, J.; Polenova, T.; Yang, J.; Rienstra, C. M.; Mueller, L. J. J-based 2D homonuclear and heteronuclear correlation in solid-state proteins. *Magn. Reson. Chem.* **2007**, *45*, S84−S92.

(113) Chen, L.; Olsen, R. A.; Elliott, D. W.; Boettcher, J. M.; Zhou, D. H.; Rienstra, C. M.; Mueller, L. J. Constant-time through-bond ^{13}C correlation spectroscopy for assigning protein resonances with solid-state NMR spectroscopy. *J. Am. Chem. Soc.* **2006**, *128*, 9992−9993.

(114) Bayro, M. J.; Ramachandran, R.; Caporini, M. A.; Eddy, M. T.; Griffin, R. G. Radio frequency-driven recoupling at high magic-angle spinning frequencies: homonuclear recoupling sans heteronuclear decoupling. *J. Chem. Phys.* **2008**, *128*, No. 052321.

(115) Hughes, C. E.; Luca, S.; Baldus, M. Radio-frequency driven polarization transfer without heteronuclear decoupling in rotating solids. *Chem. Phys. Lett.* **2004**, *385*, 435−440.

(116) Levitt, M. H.; Grant, D. M.; Harris, R. K. Symmetry-based pulse sequences in magic-angle spinning solid-state NMR. *Encyclopedia of Nuclear Magnetic Resonance*; Wiley: Chichester, U.K., 2007; Vol. *9*, pp 165−196.

(117) Hou, G.; Yan, S.; Trébosc, J.; Amoureux, J.-P.; Polenova, T. Broadband homonuclear correlation spectroscopy driven by combined R2nv sequences under fast magic angle spinning for NMR structural analysis of organic and biological solids. *J. Magn. Reson.* **2013**, *232*, 18−30.

(118) Weingarth, M.; Demco, D. E.; Bodenhausen, G.; Tekely, P. Improved magnetization transfer in solid-state NMR with fast magic angle spinning. *Chem. Phys. Lett.* **2009**, *469*, 342−348.

(119) Hou, G.; Yan, S.; Sun, S.; Han, Y.; Byeon, I.-J. L.; Ahn, J.; Concel, J.; Samoson, A.; Gronenborn, A. M.; Polenova, T. Spin diffusion driven by R-symmetry sequences: applications to homonuclear correlation spectroscopy in MAS NMR of biological and organic solids. *J. Am. Chem. Soc.* **2011**, *133*, 3943−3953.

(120) Aluas, M.; Tripon, C.; Griffin, J. M.; Filip, X.; Ladizhansky, V.; Griffin, R. G.; Brown, S. P.; Filip, C. CHHC and $^{1}H−^{1}H$ magnetization exchange: Analysis by experimental solid-state NMR and 11-spin density-matrix simulations. *J. Magn. Reson.* **2009**, *199*, 173−187.

(121) Lange, A.; Luca, S.; Baldus, M. Structural constraints from proton-mediated rare-spin correlation spectroscopy in rotating solids. *J. Am. Chem. Soc.* **2002**, *124*, 9704−9705.

(122) Paul, S.; Takahashi, H.; Hediger, S.; De Paëpe, G. Chapter three - third spin-assisted recoupling in SSNMR: theoretical insights and practicable application to biomolecular structure determination. *Annu. Rep. NMR Spectrosc.* **2015**, *85*, 93−142.

(123) De Paepe, G.; Lewandowski, J. R.; Loquet, A.; Bockmann, A.; Griffin, R. G. Proton assisted recoupling and protein structure determination. *J. Chem. Phys.* **2008**, *129*, 245101.

(124) Gelenter, M. D.; Dregni, A. J.; Hong, M. Pulsed third-spin-assisted recoupling NMR for obtaining long-range $^{13}C−^{13}C$ and $^{15}N−^{13}C$ distance restraints. *J. Phys. Chem. B* **2020**, *124*, 7138−7151.

(125) Ader, C.; Schneider, R.; Seidel, K.; Etzkorn, M.; Becker, S.; Baldus, M. Structural rearrangements of membrane proteins probed by water-edited solid-state NMR spectroscopy. *J. Am. Chem. Soc.* **2009**, *131*, 170−176.

(126) Williams, J. K.; Schmidt-Rohr, K.; Hong, M. Aromatic spectral editing techniques for magic-angle-spinning solid-state NMR spectroscopy of uniformly ^{13}C-labeled proteins. *Solid State Nucl. Magn. Reson.* **2015**, *72*, 118−126.

(127) Schmidt-Rohr, K.; Fritzsching, K. J.; Liao, S. Y.; Hong, M. Spectral editing of two-dimensional magic-angle-spinning solid-state NMR spectra for protein resonance assignment and structure determination. *J. Biomol. NMR* **2012**, *54*, 343−353.

(128) Komatsu, T.; Kikuchi, J. Selective signal detection in solid-state NMR using rotor-synchronized dipolar dephasing for the analysis of hemicellulose in lignocellulosic biomass. *J. Phys. Chem. Lett.* **2013**, *4*, 2279−2283.

(129) Shcherbakov, A. A.; Medeiros-Silva, J.; Tran, N.; Gelenter, M. D.; Hong, M. From angstroms to nanometers: measuring interatomic distances by solid-state NMR. *Chem. Rev.* **2021**, DOI: 10.1021/acs.chemrev.1c00662.

(130) Phyo, P.; Wang, T.; Kiemle, S. N.; O'Neill, H.; Pingali, S. V.; Hong, M.; Cosgrove, D. J. Gradients in wall mechanics and polysaccharides along growing inflorescence stems. *Plant Physiol.* **2017**, *175*, 1593−1607.

(131) Dick-Perez, M.; Wang, T.; Salazar, A.; Zabotina, O. A.; Hong, M. Multidimensional solid-state NMR studies of the structure and dynamics of pectic polysaccharides in uniformly ^{13}C-labeled Arabidopsis primary cell walls. *Magn. Reson. Chem.* **2012**, *50*, 539−550.

(132) Wang, T.; Hong, M. Structure and dynamics of polysaccharides in plant cell walls from solid-state NMR. *NMR in Glycoscience and Glycotechnology*; Royal Society of Chemistry: 2017; pp 290−304.

(133) Ishima, R.; Torchia, D. A. Protein dynamics from NMR. *Nat. Struct. Biol.* **2000**, *7*, 740−743.

(134) Mittermaier, A.; Kay, L. E. New tools provide new insights in NMR studies of protein dynamics. *Science* **2006**, *312*, 224−228.

(135) Barna, J. C. J.; Laue, E. D.; Mayger, M. R.; Skilling, J.; Worrall, S. P. Exponential sampling, an alternative method for sampling in two-dimensional NMR experiments. *J. Magn. Reson.* **1987**, *73*, 69−77.

(136) Kaur, M.; Lewis, C. M.; Chronister, A.; Phun, G. S.; Mueller, L. J. Non-uniform sampling in NMR spectroscopy and the preservation of spectral knowledge in the time and frequency domains. *J. Phys. Chem. A* **2020**, *124*, 5474−5486.

(137) Burakova, E.; Vasa, S. K.; Klein, A.; Linser, R. Non-uniform sampling in quantitative assessment of heterogeneous solid-state NMR line shapes. *J. Biomol. NMR* **2020**, *74*, 71−82.

(138) Sun, S.; Yan, S.; Guo, C.; Li, M.; Hoch, J. C.; Williams, J. C.; Polenova, T. A timesaving strategy for MAS NMR spectroscopy by combining non-uniform sampling and paramagnetic relaxation assisted condensed data collection. *J. Phys. Chem. B* **2012**, *116*, 13585−13596.

(139) Linser, R.; Bardiaux, B.; Andreas, L. B.; Hyberts, S. G.; Morris, V. K.; Pintacuda, G.; Sunde, M.; Kwan, A. H.; Wagner, G. Solid-state NMR structure determination from diagonal-compensated, sparsely nonuniform-sampled 4D proton−proton restraints. *J. Am. Chem. Soc.* **2014**, *136*, 11002−11010.

(140) Bertini, I.; Luchinat, C.; Parigi, G.; Pierattelli, R. NMR spectroscopy of paramagnetic metalloproteins. *ChemBioChem* **2005**, *6*, 1536−1549.

(141) Sengupta, I.; Nadaud, P. S.; Helmus, J. J.; Schwieters, C. D.; Jaroniec, C. P. Protein fold determined by paramagnetic magic-angle spinning solid-state NMR spectroscopy. *Nat. Chem.* **2012**, *4*, 410−417.

(142) Nadaud, P. S.; Helmus, J. J.; Kall, S. L.; Jaroniec, C. P. Paramagnetic ions enable tuning of nuclear relaxation rates and provide long-range structural restraints in solid-state NMR of proteins. *J. Am. Chem. Soc.* **2009**, *131*, 8108−8120.

(143) Oster, C.; Kosol, S.; Hartlmuller, C.; Lamley, J. M.; Luga, D.; Oss, A.; Org, M.-L.; Vanatalu, K.; Samoson, A.; Madl, T.; et al. Characterization of protein−protein interfaces in large complexes by solid-state NMR solvent paramagnetic relaxation enhancements. *J. Am. Chem. Soc.* **2017**, *139*, 12165−12174.

(144) Zuckerstätter, G.; Terinte, N.; Sixta, H.; Schuster, K. C. Novel insight into cellulose supramolecular structure through ^{13}C CP-MAS NMR spectroscopy and paramagnetic relaxation enhancement. *Carbohydr. Polym.* **2013**, *93*, 122−128.

(145) Wang, T.; Chen, Y.; Tabuchi, A.; Cosgrove, D. J.; Hong, M. The target of β-expansin EXPB1 in maize cell walls from binding and solid-state NMR studies. *Plant Physiol.* **2016**, *172*, 2107−2119.

(146) Clore, M. G.; Iwahara, J. Theory, practice, and applications of paramagnetic relaxation enhancement for the characterization of transient low-population states of biological macromolecules and their complexes. *Chem. Rev.* **2009**, *109*, 4108−4139.

(147) Chakraborty, A.; Deligey, F.; Quach, J.; Mentink-Vigier, F.; Wang, P.; Wang, T. Biomolecular complex viewed by dynamic nuclear polarization solid-state NMR spectroscopy. *Biochem. Soc. Trans.* **2020**, *48*, 1089−1099.

(148) Reif, B. Proton-detection in biological MAS solid-state NMR spectroscopy. *Modern Magnetic Resonance*; Springer International Publishing: Cham, Switzerland, 2017; pp 1−33.

(149) Ishii, Y.; Wickramasinghe, A.; Matsuda, I.; Endo, Y.; Ishii, Y.; Nishiyama, Y.; Nemoto, T.; Kamihara, T. Progress in proton-detected solid-state NMR (ssNMR): super-fast 2D ssNMR collection for nano-mole-scale proteins. *J. Magn. Reson.* **2018**, *286*, 99−109.

(150) Lee, D.; Hediger, S.; Paëpe, G. D. High-field solid-state NMR with dynamic nuclear polarization. *Modern Magnetic Resonance*; Springer International Publishing: Cham, Switzerland, 2017; pp 861−877.

(151) Lilly Thankamony, A. S.; Wittmann, J.J.; Kaushik, M.; Corzilius, B. Dynamic nuclear polarization for sensitivity enhancement in modern solid-state NMR. *Prog. Nucl. Magn. Reson. Spectrosc.* **2017**, *102−103*, 120−195.

(152) Gauto, D.; Dakhlaoui, O.; Marin-Montesinos, I.; Hediger, S.; De Paëpe, G. Targeted DNP for biomolecular solid-state NMR. *Chem. Sci.* **2021**, *12*, 6223−6237.

(153) Narasimhan, S.; Scherpe, S.; Lucini Paioni, A.; van der Zwan, J.; Folkers, G. E.; Ovaa, H.; Baldus, M. DNP-Supported Solid-state NMR spectroscopy of proteins inside mammalian cells. *Angew. Chem., Int. Ed.* **2019**, *58*, 12969−12973.

(154) Quinn, C. M.; Wang, M.; Polenova, T. NMR of macromolecular assemblies and machines at 1 GHz and beyond: new transformative opportunities for molecular structural biology. *Methods Mol. Biol.* **2018**, *1688*, 1−35.

(155) Nimerovsky, E.; Movellan, K. T.; Zhang, X. C.; Forster, M. C.; Najbauer, E.; Xue, K.; Dervişoğlu, R.; Giller, K.; Griesinger, C.; Becker, S.; et al. Proton detected solid-state NMR of membrane proteins at 28 T (1.2 GHz) and 100 kHz magic-angle spinning. *Biomolecules* **2021**, *11*, 752.

(156) Mance, D.; Weingarth, M.; Baldus, M. Solid-state NMR on complex biomolecules: methods and applications. *Modern Magnetic Resonance*; Springer International Publishing: Cham, Switzerland, 2016; pp 487−503.

(157) van der Wel, P. C. A. New applications of solid-state NMR in structural biology. *Emerging Top. Life Sci.* **2018**, *2*, 57−67.

(158) Ni, Q. Z.; Daviso, E.; Can, T. V.; Markhasin, E.; Jawla, S. K.; Swager, T. M.; Temkin, R. J.; Herzfeld, J.; Griffin, R. G. High frequency dynamic nuclear polarization. *Acc. Chem. Res.* **2013**, *46*, 1933−1941.

(159) Abragam, A.; Goldman, M. Principles of dynamic nuclear polarisation. *Rep. Prog. Phys.* **1978**, *41*, 395−467.

(160) Wenckebach, W. T. Dynamic nuclear polarization via the cross effect and thermal mixing: A. The role of triple spin flips. *J. Magn. Reson.* **2019**, *299*, 124−134.

(161) Serra, S. C.; Rosso, A.; Tedoldi, F. On the role of electron−nucleus contact and microwave saturation in thermal mixing DNP. *Phys. Chem. Chem. Phys.* **2013**, *15*, 8416−8428.

(162) Jannin, S.; Comment, A.; van der Klink, J. J. Dynamic nuclear polarization by thermal mixing under partial saturation. *Appl. Magn. Reson.* **2012**, *43*, 59−68.

(163) Hovav, Y.; Feintuch, A.; Vega, S. Theoretical aspects of dynamic nuclear polarization in the solid state − The cross effect. *J. Magn. Reson.* **2012**, *214*, 29−41.

(164) Wind, R. A.; Duijvestijn, M. J.; van der Lugt, C.; Manenschijn, A.; Vriend, J. Applications of dynamic nuclear polarization in ^{13}C NMR in solids. *Prog. Nucl. Magn. Reson. Spectrosc.* **1985**, *17*, 33−67.

(165) Can, T. V.; Ni, Q. Z.; Griffin, R. G. Mechanisms of dynamic nuclear polarization in insulating solids. *J. Magn. Reson.* **2015**, *253*, 23−35.

(166) Can, T. V.; Caporini, M. A.; Mentink-Vigier, F.; Corzilius, B.; Walish, J. J.; Rosay, M.; Maas, W. E.; Baldus, M.; Vega, S.; Swager, T. M.; et al. Overhauser effects in insulating solids. *J. Chem. Phys.* **2014**, *141*, No. 064202.

(167) Maly, T.; Debelouchina, G. T.; Bajaj, V. S.; Hu, K.-N.; Joo, C.-G.; Mak-Jurkauskas, M. L.; Sirigiri, J. R.; van der Wel, P. C. A.; Herzfeld, J.; Temkin, R. J.; Griffin, R. G.; et al. Dynamic nuclear polarization at high magnetic fields. *J. Chem. Phys.* **2008**, *128*, No. 052211.

(168) Smith, A. A.; Corzilius, B.; Barnes, A. B.; Maly, T.; Griffin, R. G. Solid effect dynamic nuclear polarization and polarization pathways. *J. Chem. Phys.* **2012**, *136*, No. 015101.

(169) Hediger, S.; Lee, D.; Mentink-Vigier, F.; De Paepe, G. MAS-DNP enhancements: hyperpolarization, depolarization, and absolute sensitivity. *eMagRes* **2018**, *7*, 105−116.

(170) Sauvée, C.; Rosay, M.; Casano, G.; Aussenac, F.; Weber, R. T.; Ouari, O.; Tordo, P. Highly efficient, water-soluble polarizing agents for dynamic nuclear polarization at high frequency. *Angew. Chem., Int. Ed.* **2013**, *52*, 10858−10861.

(171) Mentink-Vigier, F.; Marin-Montesinos, I.; Jagtap, A. P.; Halbritter, T.; van Tol, J.; Hediger, S.; Lee, D.; Sigurdsson, S. T.; De Paëpe, G. Computationally assisted design of polarizing agents for dynamic nuclear polarization enhanced NMR: the AsymPol family. *J. Am. Chem. Soc.* **2018**, *140*, 11013−11019.

(172) Dubroca, T.; Smith, A. N.; Pike, K. J.; Froud, S.; Wylde, R.; Trociewitz, B.; McKay, J.; Mentink-Vigier, F.; van Tol, J.; Wi, S.; et al. A quasi-optical and corrugated waveguide microwave transmission system for simultaneous dynamic nuclear polarization NMR on two separate 14.1 T spectrometers. *J. Magn. Reson.* **2018**, *289*, 35−44.

(173) Chaudhari, S. R.; Wisser, D.; Pinon, A. C.; Berruyer, P.; Gajan, D.; Tordo, P.; Ouari, O.; Reiter, C.; Engelke, F.; Copéret, C.; et al. Dynamic nuclear polarization efficiency increased by very fast magic angle spinning. *J. Am. Chem. Soc.* **2017**, *139*, 10609−10612.

(174) Lesage, A.; Lelli, M.; Gajan, D.; Caporini, M. A.; Vitzthum, V.; Miéville, P.; Alauzun, J.; Roussey, A.; Thieuleux, C.; Mehdi, A.; et al. Surface enhanced NMR spectroscopy by dynamic nuclear polarization. *J. Am. Chem. Soc.* **2010**, *132*, 15459−15461.

(175) DeHaven, B. A.; Tokarski, J. T., 3rd; Korous, A. A.; Mentink-Vigier, F.; Makris, T. M.; Brugh, A. M.; Forbes, M. D. E.; van Tol, J.; Bowers, C. R.; Shimizu, L. S. Persistent radicals of self-assembled benzophenone bis-urea macrocycles: characterization and application as a polarizing agent for solid-state DNP MAS spectroscopy. *Chem. - Eur. J.* **2017**, *23*, 8315−8319.

(176) Mentink-Vigier, F.; Akbey, Ü.; Hovav, Y.; Vega, S.; Oschkinat, H.; Feintuch, A. Fast passage dynamic nuclear polarization on rotating solids. *J. Magn. Reson.* **2012**, *224*, 13−21.

(177) Mentink-Vigier, F.; Akbey, Ü.; Oschkinat, H.; Vega, S.; Feintuch, A. Theoretical aspects of magic angle spinning - dynamic nuclear polarization. *J. Magn. Reson.* **2015**, *258*, 102−120.

(178) Mentink-Vigier, F.; Paul, S.; Lee, D.; Feintuch, A.; Hediger, S.; Vega, S.; De Paëpe, G. Nuclear depolarization and absolute sensitivity in magic-angle spinning cross effect dynamic nuclear polarization. *Phys. Chem. Chem. Phys.* **2015**, *17*, 21824−21836.

(179) Mentink-Vigier, F.; Vega, S.; De Paëpe, G. Fast and accurate MAS−DNP simulations of large spin ensembles. *Phys. Chem. Chem. Phys.* **2017**, *19*, 3506−3522.

(180) Mentink-Vigier, F. Optimizing nitroxide biradicals for cross-effect MAS-DNP: the role of g-tensors' distance. *Phys. Chem. Chem. Phys.* **2020**, *22*, 3643−3652.

(181) Mentink-Vigier, F.; Dubroca, T.; Van Tol, J.; Sigurdsson, S. T. The distance between g-tensors of nitroxide biradicals governs MAS-DNP performance: The case of the bTurea family. *J. Magn. Reson.* **2021**, *329*, 107026.

(182) Thurber, K. R.; Tycko, R. Theory for cross effect dynamic nuclear polarization under magic-angle spinning in solid state nuclear magnetic resonance: The importance of level crossings. *J. Chem. Phys.* **2012**, *137*, No. 084508.

(183) Thurber, K. R.; Tycko, R. On Mechanisms of dynamic nuclear polarization in solids. *Isr. J. Chem.* **2014**, *54*, 39−46.

(184) Thurber, K. R.; Tycko, R. Perturbation of nuclear spin polarizations in solid state NMR of nitroxide-doped samples by magic-angle spinning without microwaves. *J. Chem. Phys.* **2014**, *140*, 184201.

(185) Kundu, K.; Mentink-Vigier, F.; Feintuch, A.; Vega, S. DNP mechanisms. *eMagRes* **2019**, *8*, 295−337.

(186) Hu, K.-N.; Yu, H.-H.; Swager, T. M.; Griffin, R. G. Dynamic nuclear polarization with biradicals. *J. Am. Chem. Soc.* **2004**, *126*, 10844−10845.

(187) Song, C.; Hu, K.-N.; Joo, C.-G.; Swager, T. M.; Griffin, R. G. TOTAPOL: A biradical polarizing agent for dynamic nuclear polarization experiments in aqueous media. *J. Am. Chem. Soc.* **2006**, *128*, 11385−11390.

(188) Mathies, G.; Caporini, M. A.; Michaelis, V. K.; Liu, Y.; Hu, K.-N.; Mance, D.; Zweier, J. L.; Rosay, M.; Baldus, M.; Griffin, R. G. Efficient dynamic nuclear polarization at 800 MHz/527 GHz with trityl-nitroxide biradicals. *Angew. Chem., Int. Ed.* **2015**, *54*, 11770−11774.

(189) Sauvée, C.; Casano, G.; Abel, S.; Rockenbauer, A.; Akhmetzyanov, D.; Karoui, H.; Siri, D.; Aussenac, F.; Maas, W.; Weber, R. T.; et al. Tailoring of polarizing agents in the bTurea series for cross-effect dynamic nuclear polarization in aqueous media. *Chem. - Eur. J.* **2016**, *22*, 5598−5606.

(190) Kubicki, D. J.; Casano, G.; Schwarzwälder, M.; Abel, S.; Sauvée, C.; Ganesan, K.; Yulikov, M.; Rossini, A. J.; Jeschke, G.; Copéret, C.; et al. Rational design of dinitroxide biradicals for efficient cross-effect dynamic nuclear polarization. *Chem. Sci.* **2016**, *7*, 550−558.

(191) Stevanato, G.; Casano, G.; Kubicki, D. J.; Rao, Y.; Esteban Hofer, L.; Menzildjian, G.; Karoui, H.; Siri, D.; Cordova, M.; Yulikov, M.; et al. Open and closed radicals: local geometry around unpaired electrons governs magic-angle spinning dynamic nuclear polarization performance. *J. Am. Chem. Soc.* **2020**, *142*, 16587−16599.

(192) Zagdoun, A.; Casano, G.; Ouari, O.; Lapadula, G.; Rossini, A. J.; Lelli, M.; Baffert, M.; Gajan, D.; Veyre, L.; Maas, W. E.; et al. A slowly relaxing rigid biradical for efficient dynamic nuclear polarization surface-enhanced NMR spectroscopy: expeditious characterization of functional group manipulation in hybrid materials. *J. Am. Chem. Soc.* **2012**, *134*, 2284−2291.

(193) Lund, A.; Casano, G.; Menzildjian, G.; Kaushik, M.; Stevanato, G.; Yulikov, M.; Jabbour, R.; Wisser, D.; Renom-Carrasco, M.; Thieuleux, C.; et al. TinyPols: a family of water-soluble binitroxides tailored for dynamic nuclear polarization enhanced NMR spectroscopy at 18.8 and 21.1 T. *Chem. Sci.* **2020**, *11*, 2810−2818.

(194) Wisser, D.; Karthikeyan, G.; Lund, A.; Casano, G.; Karoui, H.; Yulikov, M.; Menzildjian, G.; Pinon, A. C.; Purea, A.; Engelke, F.; et al. BDPA-nitroxide biradicals tailored for efficient dynamic nuclear

polarization enhanced solid-state NMR at magnetic fields up to 21.1 T. *J. Am. Chem. Soc.* **2018**, *140*, 13340−13349.

(195) Jagtap, A. P.; Geiger, M.-A.; Stöppler, D.; Orwick-Rydmark, M.; Oschkinat, H.; Sigurdsson, S. T. bcTol: a highly water-soluble biradical for efficient dynamic nuclear polarization of biomolecules. *Chem. Commun.* **2016**, *52*, 7020−7023.

(196) Geiger, M.-A.; Jagtap, A. P.; Kaushik, M.; Sun, H.; Stöppler, D.; Sigurdsson, S. T.; Corzilius, B.; Oschkinat, H. Efficiency of water-soluble nitroxide biradicals for dynamic nuclear polarization in rotating solids at 9.4 T: bcTol-M and cyolyl-TOTAPOL as new polarizing agents. *Chem. - Eur. J.* **2018**, *24*, 13485−13494.

(197) Zhai, W.; Lucini Paioni, A.; Cai, X.; Narasimhan, S.; Medeiros-Silva, J.; Zhang, W.; Rockenbauer, A.; Weingarth, M.; Song, Y.; Baldus, M.; et al. Postmodification via thiol-click chemistry yields hydrophilic trityl-nitroxide biradicals for biomolecular high-field dynamic nuclear polarization. *J. Phys. Chem. B* **2020**, *124*, 9047−9060.

(198) Mentink-Vigier, F.; Mathies, G.; Liu, Y.; Barra, A.-L.; Caporini, M. A.; Lee, D.; Hediger, S.; Griffin, R. G.; De Paepe, G. Efficient cross-effect dynamic nuclear polarization without depolarization in high-resolution MAS NMR. *Chem. Sci.* **2017**, *8*, 8150−8163.

(199) Mentink-Vigier, F.; Barra, A.-L.; van Tol, J.; Hediger, S.; Lee, D.; De Paëpe, G. De novo prediction of cross-effect efficiency for magic angle spinning dynamic nuclear polarization. *Phys. Chem. Chem. Phys.* **2019**, *21*, 2166−2176.

(200) Perras, F. A.; Sadow, A.; Pruski, M. In Silico Design of DNP polarizing agents: can current dinitroxides be improved? *ChemPhysChem* **2017**, *18*, 2279−2287.

(201) Perras, F. A.; Pruski, M. Large-scale ab initio simulations of MAS DNP enhancements using a Monte Carlo optimization strategy. *J. Chem. Phys.* **2018**, *149*, 154202.

(202) Perras, F. A.; Raju, M.; Carnahan, S. L.; Akbarian, D.; van Duin, A. C. T.; Rossini, A. J.; Pruski, M. Full-scale ab initio simulation of magic-angle-spinning dynamic nuclear polarization. *J. Phys. Chem. Lett.* **2020**, *11*, 5655−5660.

(203) Becerra, L. R.; Gerfen, G. J.; Temkin, R. J.; Singel, D. J.; Griffin, R. G. Dynamic nuclear polarization with a cyclotron resonance maser at 5 T. *Phys. Rev. Lett.* **1993**, *71*, 3561−3564.

(204) Hall, D. A.; Maus, D. C.; Gerfen, G. J.; Inati, S. J.; Becerra, L. R.; Dahlquist, F. W.; Griffin, R. G. Polarization-enhanced NMR spectroscopy of biomolecules in frozen solution. *Science* **1997**, *276*, 930−932.

(205) Rosay, M.; Tometich, L.; Pawsey, S.; Bader, R.; Schauwecker, R.; Blank, M.; Borchard, P. M.; Cauffman, S. R.; Felch, K. L.; Weber, R. T.; et al. Solid-state dynamic nuclear polarization at 263 GHz: spectrometer design and experimental results. *Phys. Chem. Chem. Phys.* **2010**, *12*, 5850−5860.

(206) Rosay, M.; Blank, M.; Engelke, F. Instrumentation for solid-state dynamic nuclear polarization with magic angle spinning NMR. *J. Magn. Reson.* **2016**, *264*, 88−98.

(207) Berruyer, P.; Björgvinsdóttir, S.; Bertarello, A.; Stevanato, G.; Rao, Y.; Karthikeyan, G.; Casano, G.; Ouari, O.; Lelli, M.; Reiter, C.; et al. Dynamic nuclear polarization enhancement of 200 at 21.15 T enabled by 65 kHz magic angle spinning. *J. Phys. Chem. Lett.* **2020**, *11*, 8386−8391.

(208) Chaudhari, S. R.; Berruyer, P.; Gajan, D.; Reiter, C.; Engelke, F.; Silverio, D. L.; Copéret, C.; Lelli, M.; Lesage, A.; Emsley, L. Dynamic nuclear polarization at 40 kHz magic angle spinning. *Phys. Chem. Chem. Phys.* **2016**, *18*, 10616−10622.

(209) Purea, A.; Reiter, C.; Dimitriadis, A. I.; de Rijk, E.; Aussenac, F.; Sergeyev, I.; Rosay, M.; Engelke, F. Improved waveguide coupling for 1.3 mm MAS DNP probes at 263 GHz. *J. Magn. Reson.* **2019**, *302*, 43−49.

(210) Bouleau, E.; Saint-Bonnet, P.; Mentink-Vigier, F.; Takahashi, H.; Jacquot, J. F.; Bardet, M.; Aussenac, F.; Purea, A.; Engelke, F.; Hediger, S.; et al. Pushing NMR sensitivity limits using dynamic nuclear polarization with closed-loop cryogenic helium sample spinning. *Chem. Sci.* **2015**, *6*, 6806−6812.

(211) Lee, D.; Bouleau, E.; Saint-Bonnet, P.; Hediger, S.; De Paëpe, G. Ultra-low temperature MAS-DNP. *J. Magn. Reson.* **2016**, *264*, 116−124.

(212) Matsuki, Y.; Ueda, K.; Idehara, T.; Ikeda, R.; Ogawa, I.; Nakamura, S.; Toda, M.; Anai, T.; Fujiwara, T. Helium-cooling and -spinning dynamic nuclear polarization for sensitivity-enhanced solid-state NMR at 14T and 30K. *J. Magn. Reson.* **2012**, *225*, 1−9.

(213) Matsuki, Y.; Idehara, T.; Fukazawa, J.; Fujiwara, T. Advanced instrumentation for DNP-enhanced MAS NMR for higher magnetic fields and lower temperatures. *J. Magn. Reson.* **2016**, *264*, 107−115.

(214) Sugishita, T.; Matsuki, Y.; Fujiwara, T. Absolute ^{1}H polarization measurement with a spin-correlated component of magnetization by hyperpolarized MAS-DNP solid-state NMR. *Solid State Nucl. Magn. Reson.* **2019**, *99*, 20−26.

(215) Matsuki, Y.; Kobayashi, T.; Fukazawa, J.; Perras, F. A.; Pruski, M.; Fujiwara, T. Efficiency analysis of helium-cooled MAS DNP: case studies of surface-modified nanoparticles and homogeneous small-molecule solutions. *Phys. Chem. Chem. Phys.* **2021**, *23*, 4919−4926.

(216) Matsuki, Y.; Fujiwara, T. Cryogenic platforms and optimized DNP sensitivity. *eMagRes* **2018**, *7*, 9−23.

(217) Thurber, K. R.; Potapov, A.; Yau, W.-M.; Tycko, R. Solid state nuclear magnetic resonance with magic-angle spinning and dynamic nuclear polarization below 25K. *J. Magn. Reson.* **2013**, *226*, 100−106.

(218) Thurber, K.; Tycko, R. Low-temperature dynamic nuclear polarization with helium-cooled samples and nitrogen-driven magic-angle spinning. *J. Magn. Reson.* **2016**, *264*, 99−106.

(219) Takahashi, H.; Ayala, I.; Bardet, M.; De Paëpe, G.; Simorre, J. P.; Hediger, S. Solid-state NMR on bacterial cells: selective cell wall signal enhancement and resolution improvement using dynamic nuclear polarization. *J. Am. Chem. Soc.* **2013**, *135*, 5105−5110.

(220) Jantschke, A.; Koers, E.; Mance, D.; Weingarth, M.; Brunner, E.; Baldus, M. Insight into the supramolecular architecture of intact diatom biosilica from DNP-supported solid-state NMR spectroscopy. *Angew. Chem., Int. Ed.* **2015**, *54*, 15069−15073.

(221) Zhao, W.; Kirui, A.; Deligey, F.; Mentink-Vigier, F.; Zhou, Y.; Zhang, B.; Wang, T. Solid-state NMR of unlabeled plant cell walls: high-resolution structural analysis without isotopic enrichment. *Biotechnol. Biofuels* **2021**, *14*, 14.

(222) Zhang, L.; Gao, C.; Mentink-Vigier, F.; Tang, L.; Zhang, D.; Wang, S.; Cao, S.; Xu, Z.; Liu, X.; Wang, T.; et al. Arabinosyl deacetylase modulates the arabinoxylan acetylation profile and secondary wall formation. *Plant Cell* **2019**, *31*, 1113−1126.

(223) Lee, D.; Hediger, S.; De Paëpe, G. Is solid-state NMR enhanced by dynamic nuclear polarization? *Solid State Nucl. Magn. Reson.* **2015**, *66−67*, 6−20.

(224) Equbal, A.; Leavesley, A.; Jain, S. K.; Han, S. Cross-effect dynamic nuclear polarization explained: polarization, depolarization, and oversaturation. *J. Phys. Chem. Lett.* **2019**, *10*, 548−558.

(225) Rankin, A. G. M.; Trébosc, J.; Pourpoint, F.; Amoureux, J.-P.; Lafon, O. Recent developments in MAS DNP-NMR of materials. *Solid State Nucl. Magn. Reson.* **2019**, *101*, 116−143.

(226) Akbey, Ü.; Franks, W. T.; Linden, A.; Orwick-Rydmark, M.; Lange, S.; Oschkinat, H. Dynamic nuclear polarization enhanced NMR in the solid-state. *Top. Curr. Chem.* **2013**, *338*, 181−228.

(227) Takahashi, H.; Hediger, S.; De Paëpe, G. Matrix-free dynamic nuclear polarization enables solid-state NMR ^{13}C−^{13}C correlation spectroscopy of proteins at natural isotopic abundance. *Chem. Commun.* **2013**, *49*, 9479−9481.

(228) Rossini, A. J.; Zagdoun, A.; Hegner, F.; Schwarzwälder, M.; Gajan, D.; Copéret, C.; Lesage, A.; Emsley, L. Dynamic nuclear polarization NMR spectroscopy of microcrystalline solids. *J. Am. Chem. Soc.* **2012**, *134*, 16899−16908.

(229) Smith, A. N.; Märker, K.; Hediger, S.; De Paëpe, G. Natural isotopic abundance ^{13}C and ^{15}N multidimensional solid-state NMR enabled by dynamic nuclear polarization. *J. Phys. Chem. Lett.* **2019**, *10*, 4652−4662.

(230) Märker, K.; Paul, S.; Fernández-de-Alba, C.; Lee, D.; Mouesca, J.-M.; Hediger, S.; De Paëpe, G. Welcoming natural isotopic abundance in solid-state NMR: probing π-stacking and supramolecular structure of organic nanoassemblies using DNP. *Chem. Sci.* **2017**, *8*, 974−987.

(231) Märker, K.; Pingret, M.; Mouesca, J.-M.; Gasparutto, D.; Hediger, S.; De Paëpe, G. A new tool for NMR crystallography:

complete ^{13}C/^{15}N assignment of organic molecules at natural isotopic abundance using DNP-enhanced solid-state NMR. *J. Am. Chem. Soc.* **2015**, *137*, 13796−13799.

(232) Cosgrove, D. J. Re-constructing our models of cellulose and primary cell wall assembly. *Curr. Opin. Plant Biol.* **2014**, *22*, 122−131.

(233) Purushotham, P.; Ho, R.; Zimmer, J. Architecture of a catalytically active homotrimeric plant cellulose synthase complex. *Science* **2020**, *369*, 1089−1094.

(234) Scheller, H. V.; Ulvskov, P. Hemicelluloses. *Annu. Rev. Plant Biol.* **2010**, *61*, 263−289.

(235) Pauly, M.; Gille, S.; Liu, L.; Mansoori, N.; de Souza, A.; Schultink, A.; Xiong, G. Hemicellulose biosynthesis. *Planta* **2013**, *238*, 627−642.

(236) Mohnen, D. Pectin structure and biosynthesis. *Curr. Opin. Plant Biol.* **2008**, *11*, 266−277.

(237) Anderson, C. T. We be jammin': an update on pectin biosynthesis, trafficking and dynamics. *J. Exp. Bot.* **2016**, *67*, 495−502.

(238) Atmodjo, M. A.; Hao, Z.; Mohnen, D. Evolving views of pectin biosynthesis. *Annu. Rev. Plant Biol.* **2013**, *64*, 747−779.

(239) Biswal, A. K.; Atmodjo, M. A.; Li, M.; Baxter, H. L.; Yoo, C. G.; Pu, Y.; Lee, Y. C.; Mazarei, M.; Black, I. M.; Zhang, J. Y.; et al. Sugar release and growth of biofuel crops are improved by downregulation of pectin biosynthesis. *Nat. Biotechnol.* **2018**, *36*, 249−257.

(240) Ralph, J.; Lapierre, C.; Boerjan, W. Lignin structure and its engineering. *Curr. Opin. Biotechnol.* **2019**, *56*, 240−249.

(241) Ralph, J.; Lundquist, K.; Brunow, G.; Lu, F.; Kim, H.; Schatz, P. F.; Marita, J. M.; Hatfield, R. D.; Ralph, S. A.; Christensen, J. H.; et al. Lignins: Natural polymers from oxidative coupling of 4-hydroxyphenyl-propanoids. *Phytochem. Rev.* **2004**, *3*, 29−60.

(242) Bonawitz, N. D.; Chapple, C. The genetics of lignin biosynthesis: connecting genotype to phenotype. *Annu. Rev. Genet.* **2010**, *44*, 337−363.

(243) Fernandes, A. N.; Thomas, L. H.; Altaner, C. M.; Callow, P.; Forsyth, V. T.; Apperley, D. C.; Kennedy, C. J.; Jarvis, M. C. Nanostructure of cellulose microfibrils in spruce wood. *Proc. Natl. Acad. Sci. U. S. A.* **2011**, *108*, E1195−E1203.

(244) Carpita, N. C.; Gibeaut, D. M. Structural models of primary cell walls in flowering plants: consistency of molecular structure with the physical properties of the walls during growth. *Plant J.* **1993**, *3*, 1−30.

(245) Donaldson, L. A. Lignification and lignin topochemistry — an ultrastructural view. *Phytochemistry* **2001**, *57*, 859−873.

(246) Himmel, M. E.; Ding, S.-Y.; Johnson, D. K.; Adney, W. S.; Nimlos, M. R.; Brady, J. W.; Foust, T. D. Biomass Recalcitrance: Engineering plants and enzymes for biofuels production. *Science* **2007**, *315*, 804−807.

(247) Vanholme, R.; Morreel, K.; Ralph, J.; Boerjan, W. Lignin engineering. *Curr. Opin. Plant Biol.* **2008**, *11*, 278−285.

(248) Jarvis, M. Cellulose stacks up. *Nature* **2003**, *426*, 611−612.

(249) Hernández-Varela, J. D.; Chanona-Pérez, J. J.; Sodi, F. C.; Vicente-Flores, M. Effect of ball milling on cellulose nanoparticles structure obtained from garlic and agave waste. *Carbohydr. Polym.* **2021**, *255*, 117347.

(250) Atalla, R. H.; Vanderhart, D. L. Native cellulose: a composite of two distinct crystalline forms. *Science* **1984**, *223*, 283−285.

(251) VanderHart, D. L.; Atalla, R. H. Studies of microstructure in native celluloses using solid-state carbon-13 NMR. *Macromolecules* **1984**, *17*, 1465−1472.

(252) Nishiyama, Y.; Sugiyama, J.; Chanzy, H.; Langan, P. Crystal structure and hydrogen bonding system in cellulose Iα from synchrotron X-ray and neutron fiber diffraction. *J. Am. Chem. Soc.* **2003**, *125*, 14300−14306.

(253) Nishiyama, Y.; Langan, P.; Chanzy, H. Crystal structure and hydrogen-bonding system in cellulose Iβ from synchrotron X-ray and neutron fiber diffraction. *J. Am. Chem. Soc.* **2002**, *124*, 9074−9082.

(254) Kono, H.; Yunoki, S.; Shikano, T.; Fujiwara, M.; Erata, T.; Takai, M. CP/MAS ^{13}C NMR study of cellulose and cellulose derivatives. 1. complete assignment of the CP/MAS ^{13}C NMR spectrum of the native cellulose. *J. Am. Chem. Soc.* **2002**, *124*, 7506−7511.

(255) Ling, Z.; Wang, T.; Makarem, M.; Cintrón, M. S.; Cheng, H.; Kang, X.; Bacher, M.; Potthast, A.; Rosenau, T.; King, H. Effects of ball milling on the structure of cotton cellulose. *Cellulose* **2019**, *26*, 305−328.

(256) Kono, H.; Numata, Y. Structural investigation of cellulose Iα and Iβ by 2D RFDR NMR spectroscopy: determination of sequence of magnetically inequivalent D-glucose units along cellulose chain. *Cellulose* **2006**, *13*, 317−326.

(257) Kono, H.; Erata, T.; Takai, M. Determination of the Through-bond carbon−carbon and carbon− proton connectivities of the native celluloses in the solid state. *Macromolecules* **2003**, *36*, 5131−5138.

(258) Nomura, S.; Kugo, Y.; Erata, T. 13C NMR and XRD studies on the enhancement of cellulose II crystallinity with low concentration NaOH post-treatments. *Cellulose* **2020**, *27*, 3553−3563.

(259) Ghosh, M.; Prajapati, B. P.; Suryawanshi, R. K.; Dey, K. K.; Kango, N. Study of the effect of enzymatic deconstruction on natural cellulose by NMR measurements. *Chem. Phys. Lett.* **2019**, *727*, 105−115.

(260) Kang, X.; Kirui, A.; Dickwella Widanage, M. C.; Mentink-Vigier, F.; Cosgrove, D. J.; Wang, T. Lignin-polysaccharide interactions in plant secondary cell walls revealed by solid-state NMR. *Nat. Commun.* **2019**, *10*, 347.

(261) Wang, T.; Yang, H.; Kubicki, J. D.; Hong, M. Cellulose structural polymorphism in plant primary cell walls investigated by high-field 2D solid-state NMR spectroscopy and density functional theory calculations. *Biomacromolecules* **2016**, *17*, 2210−2222.

(262) Phyo, P.; Wang, T.; Yang, Y.; O'Neill, H.; Hong, M. Direct determination of hydroxymethyl conformations of plant cell wall cellulose using 1H polarization transfer solid-state NMR. *Biomacromolecules* **2018**, *19*, 1485−1497.

(263) Kono, H.; Numata, Y.; Erata, T.; Takai, M. 13C and 1H resonance assignment of mercerized cellulose II by two-dimensional MAS NMR spectroscopies. *Macromolecules* **2004**, *37*, 5310−5316.

(264) Nagarajan, S.; Skillen, N. C.; Irvine, J. T.; Lawton, L. A.; Robertson, P. K. Cellulose II as bioethanol feedstock and its advantages over native cellulose. *Renewable Sustainable Energy Rev.* **2017**, *77*, 182−192.

(265) Idström, A.; Schantz, S.; Sundberg, J.; Chmelka, B. F.; Gatenholm, P.; Nordstierna, L. 13C NMR assignments of regenerated cellulose from solid-state 2D NMR spectroscopy. *Carbohydr. Polym.* **2016**, *151*, 480−487.

(266) Kita, Y.; Kusumi, R.; Kimura, T.; Kitaoka, M.; Nishiyama, Y.; Wada, M. Surface structural analysis of selectively 13C-labeled cellulose II by solid-state NMR spectroscopy. *Cellulose* **2020**, *27*, 1899−1907.

(267) Heinze, T. Cellulose: structure and properties. *Cellulose chemistry and properties: fibers, nanocelluloses and advanced materials*; Springer: Cham, Switzerland, 2015; Vol. *271*, pp 1−52.

(268) Chen, Q.; Zheng, K.; Fan, Q.; Wang, K.; Yang, H.; Jiang, J.; Liu, S. Solvability and thermal response of cellulose with different crystal configurations. *Front. Eng. Manag.* **2019**, *6*, 62−69.

(269) Wu, Q.; Xu, J.; Zhu, S.; Kuang, Y.; Wang, B.; Gao, W. Crystalline stability of cellulose III nanocrystals in the hydrothermal treatment and NaOH solution. *Carbohydr. Polym.* **2020**, *249*, 116827.

(270) Somerville, C. Cellulose Synthesis in Higher Plants. *Annu. Rev. Cell Dev. Biol.* **2006**, *22*, 53−78.

(271) Ding, S.-Y.; Zhao, S.; Zeng, Y. Size, shape, and arrangement of native cellulose fibrils in maize cell walls. *Cellulose* **2014**, *21*, 863−871.

(272) Yang, H.; Kubicki, J. D. A density functional theory study on the shape of the primary cellulose microfibril in plants: effects of C6 exocyclic group conformation and H-bonding. *Cellulose* **2020**, *27*, 2389−2402.

(273) Hill, J. L., Jr.; Hammudi, M. B.; Tien, M. The *Arabidopsis* cellulose synthase complex: a proposed hexamer of CESA trimers in an equimolar stoichiometry. *Plant Cell* **2015**, *26*, 4834−4842.

(274) Sethaphong, L.; Haigler, C. H.; Kubicki, J. D.; Zimmer, J.; Bonetta, D.; DeBolt, S.; Yingling, Y. G. Tertiary model of a plant cellulose synthase. *Proc. Natl. Acad. Sci. U. S. A.* **2013**, *110*, 7512−7517.

(275) Jarvis, M. C. Cellulose biosynthesis: counting the chains. *Plant Physiol.* **2013**, *163*, 1485−1486.

(276) Foston, M. Advances in solid-state NMR of cellulose. *Curr. Opin. Biotechnol.* **2014**, *27*, 176−184.

(277) Peciulyte, A.; Karlström, K.; Larsson, P. T.; Olsson, L. Impact of the supramolecular structure of cellulose on the efficiency of enzymatic hydrolysis. *Biotechnol. Biofuels* **2015**, *8*, 56.

(278) Wickholm, K.; Hult, E.-L.; Larsson, P. T.; Iversen, T.; Lennholm, H. Quantification of cellulose forms in complex cellulose materials: a chemometric model. *Cellulose* **2001**, *8*, 139−148.

(279) Wickholm, K.; Larsson, P. T.; Iversen, T. Assignment of non-crystalline forms in cellulose I by CP/MAS 13C NMR spectroscopy. *Carbohydr. Res.* **1998**, *312*, 123−129.

(280) Yang, H.; Wang, T.; Oehme, D.; Petridis, L.; Hong, M.; Kubicki, J. D. Structural factors affecting 13C NMR chemical shifts of cellulose: a computational study. *Cellulose* **2018**, *25*, 23−36.

(281) Kirui, A.; Ling, Z.; Kang, X.; Widanage, M. C. D.; Mentink-Vigier, F.; French, A. D.; Wang, T. Atomic resolution of cotton cellulose structure enabled by dynamic nuclear polarization solid-state NMR. *Cellulose* **2019**, *26*, 329−339.

(282) Daicho, K.; Fujisawa, S.; Kobayashi, K.; Saito, T.; Ashida, J. Cross-polarization dynamics and conformational study of variously sized cellulose crystallites using solid-state 13C NMR. *J. Wood Sci.* **2020**, *66*, 62.

(283) Ferreira, J. C.; Evtuguin, D. V.; Prates, A. Effect of cellulose structure on reactivity of Eucalyptus acid sulphite dissolving pulp. *Cellulose* **2020**, *27*, 4763−4772.

(284) Ioelovich, M. Y. Models of supramolecular structure and properties of cellulose. *Polym. Sci., Ser. A* **2016**, *58*, 925−943.

(285) Sparrman, T.; Svenningsson, L.; Sahlin-Sjövold, K.; Nordstierna, L.; Westman, G.; Bernin, D. A revised solid-state NMR method to assess the crystallinity of cellulose. *Cellulose* **2019**, *26*, 8993−9003.

(286) Ghosh, M.; Kango, N.; Dey, K. K. Investigation of the internal structure and dynamics of cellulose by 13C-NMR relaxometry and 2DPASS-MAS-NMR measurements. *J. Biomol. NMR* **2019**, *73*, 601−616.

(287) Harris, D. M.; Corbin, K.; Wang, T.; Gutierrez, R.; Bertolo, A. L.; Petti, C.; Smilgies, D.-M.; Estevez, J. M.; Bonetta, D.; Urbanowicz, B. R. Cellulose microfibril crystallinity is reduced by mutating C-terminal transmembrane region residues CESA1A903V and CESA3-T942I of cellulose synthase. *Proc. Natl. Acad. Sci. U. S. A.* **2012**, *109*, 4098−4103.

(288) Newman, R. H.; Hill, S. J.; Harris, P. J. Wide-angle x-ray scattering and solid-state nuclear magnetic resonance data combined to test models for cellulose microfibrils in mung bean cell walls. *Plant Physiol.* **2013**, *163*, 1558−1567.

(289) Wang, T.; Hong, M. Solid-state NMR investigations of cellulose structure and interactions with matrix polysaccharides in plant primary cell walls. *J. Exp. Bot.* **2016**, *67*, 503−514.

(290) Zhang, X.; Qu, T.; Mosier, N. S.; Han, L.; Xiao, W. Cellulose modification by recyclable swelling solvents. *Biotechnol. Biofuels* **2018**, *11*, 191.

(291) Barnette, A. L.; Lee, C.; Bradley, L. C.; Schreiner, E. P.; Park, Y. B.; Shin, H.; Cosgrove, D. J.; Park, S.; Kim, S. H. Quantification of crystalline cellulose in lignocellulosic biomass using sum frequency generation (SFG) vibration spectroscopy and comparison with other analytical methods. *Carbohydr. Polym.* **2012**, *89*, 802−809.

(292) Zhang, Y.; Yu, J.; Wang, X.; Durachko, D. M.; Zhang, S.; Cosgrove, D. J. Molecular insights into the complex mechanics of plant epidermal cell walls. *Science* **2021**, *372*, 706−711.

(293) Zhang, T.; Tang, H.; Vavylonis, D.; Cosgrove, D. J. Disentangling loosening from softening: insights into primary cell wall structure. *Plant J.* **2019**, *100*, 1101−1117.

(294) Zheng, Y.; Wang, X.; Chen, Y.; Wagner, E.; Cosgrove, D. J. Xyloglucan in the primary cell wall: assessment by FESEM, selective enzyme digestions and nanogold affinity tags. *Plant J.* **2018**, *93*, 211−226.

(295) Dick-Pérez, M.; Zhang, Y.; Hayes, J.; Salazar, A.; Zabotina, O. A.; Hong, M. Structure and interactions of plant cell-wall poly-

saccharides by two-and three-dimensional magic-angle-spinning solid-state NMR. *Biochemistry* **2011**, *50*, 989−1000.

(296) Kafle, K.; Park, Y. B.; Lee, C. M.; Stapleton, J. J.; Kiemle, S. N.; Cosgrove, D. J.; Kim, S. H. Effects of mechanical stretching on average orientation of cellulose and pectin in onion epidermis cell wall: A polarized FT-IR study. *Cellulose* **2017**, *24*, 3145−3154.

(297) Wang, T.; Park, Y. B.; Caporini, M. A.; Rosay, M.; Zhong, L.; Cosgrove, D. J.; Hong, M. Sensitivity-enhanced solid-state NMR detection of expansin's target in plant cell walls. *Proc. Natl. Acad. Sci. U. S. A.* **2013**, *110*, 16444−16449.

(298) Kirui, A.; Du, J.; Zhao, W.; Barnes, W.; Kang, X.; Anderson, C. T.; Xiao, C.; Wang, T. A pectin Methyltransferase modulates polysaccharide dynamics and interactions in *Arabidopsis* primary cell walls: Evidence from solid-state NMR. *Carbohydr. Polym.* **2021**, *270*, 118370.

(299) Wang, T.; Park, Y. B.; Cosgrove, D. J.; Hong, M. Cellulose-pectin spatial contacts are inherent to never-dried *Arabidopsis* primary cell walls: evidence from solid-state nuclear magnetic resonance. *Plant Physiol.* **2015**, *168*, 871−884.

(300) Wang, T.; Zabotina, O.; Hong, M. Pectin−cellulose interactions in the *Arabidopsis* primary cell wall from two-dimensional magic-angle-spinning solid-state nuclear magnetic resonance. *Biochemistry* **2012**, *51*, 9846−9856.

(301) Phyo, P.; Wang, T.; Xiao, C.; Anderson, C. T.; Hong, M. Effects of pectin molecular weight changes on the structure, dynamics, and polysaccharide interactions of primary cell walls of *Arabidopsis thaliana*: insights from solid-state NMR. *Biomacromolecules* **2017**, *18*, 2937−2950.

(302) Phyo, P.; Gu, Y.; Hong, M. Impact of acidic pH on plant cell wall polysaccharide structure and dynamics: insights into the mechanism of acid growth in plants from solid-state NMR. *Cellulose* **2019**, *26*, 291−304.

(303) Wang, T.; Williams, J. K.; Schmidt-Rohr, K.; Hong, M. Relaxation-compensated difference spin diffusion NMR for detecting $^{13}C−^{13}C$ long-range correlations in proteins and polysaccharides. *J. Biomol. NMR* **2015**, *61*, 97−107.

(304) White, P. B.; Wang, T.; Park, Y. B.; Cosgrove, D. J.; Hong, M. Water−polysaccharide interactions in the primary cell wall of *Arabidopsis thaliana* from polarization transfer solid-state NMR. *J. Am. Chem. Soc.* **2014**, *136*, 10399−10409.

(305) Wang, T.; Salazar, A.; Zabotina, O. A.; Hong, M. Structure and dynamics of *Brachypodium* primary cell wall polysaccharides from two-dimensional ^{13}C solid-state nuclear magnetic resonance spectroscopy. *Biochemistry* **2014**, *53*, 2840−2854.

(306) Duan, P.; Kaser, S. J.; Lyczakowski, J. J.; Phyo, P.; Tryfona, T.; Dupree, P.; Hong, M. Xylan structure and dynamics in native *Brachypodium* grass cell walls investigated by solid-state NMR spectroscopy. *Acs Omega* **2021**, *6*, 15460−15471.

(307) Gao, Y.; Lipton, A. S.; Wittmer, Y.; Murray, D. T.; Mortimer, J. C. A grass-specific cellulose−xylan interaction dominates in sorghum secondary cell walls. *Nat. Commun.* **2020**, *11*, 6081.

(308) Terrett, O. M.; Lyczakowski, J. J.; Yu, L.; Iuga, D.; Franks, W. T.; Brown, S. P.; Dupree, R.; Dupree, P. Molecular architecture of softwood revealed by solid-state NMR. *Nat. Commun.* **2019**, *10*, 4978.

(309) Simmons, T. J.; Mortimer, J. C.; Bernardinelli, O. D.; Pöppler, A.-C.; Brown, S. P.; Deazevedo, E. R.; Dupree, R.; Dupree, P. Folding of xylan onto cellulose fibrils in plant cell walls revealed by solid-state NMR. *Nat. Commun.* **2016**, *7*, 13902.

(310) Dupree, R.; Simmons, T. J.; Mortimer, J. C.; Patel, D.; Iuga, D.; Brown, S. P.; Dupree, P. Probing the molecular architecture of *Arabidopsis thaliana* secondary cell walls using two- and three-dimensional ^{13}C solid state nuclear magnetic resonance spectroscopy. *Biochemistry* **2015**, *54*, 2335−2345.

(311) Falcoz-Vigne, L.; Ogawa, Y.; Molina-Boisseau, S.; Nishiyama, Y.; Meyer, V.; Petit-Conil, M.; Mazeau, K.; Heux, L. Quantification of a tightly adsorbed monolayer of xylan on cellulose surface. *Cellulose* **2017**, *24*, 3725−3739.

(312) Addison, B.; Stengel, D.; Bharadwaj, V. S.; Happs, R. M.; Doeppke, C.; Wang, T.; Bomble, Y. J.; Holland, G. P.; Harman-Ware, A.

E. Selective one-dimensional $^{13}C−^{13}C$ spin-diffusion solid-state nuclear magnetic resonance methods to probe spatial arrangements in biopolymers including plant cell walls, peptides, and spider silk. *J. Phys. Chem. B* **2020**, *124*, 9870−9883.

(313) Terrett, O. M.; Dupree, P. Covalent interactions between lignin and hemicelluloses in plant secondary cell walls. *Curr. Opin. Biotechnol.* **2019**, *56*, 97−104.

(314) Berglund, J.; Mikkelsen, D.; Flanagan, B. M.; Dhital, S.; Gaunitz, S.; Henriksson, G.; Lindström, M. E.; Yakubov, G. E.; Gidley, M. J.; Vilaplana, F. Wood hemicelluloses exert distinct biomechanical contributions to cellulose fibrillar networks. *Nat. Commun.* **2020**, *11*, 4692.

(315) Vanholme, R.; Demedts, B.; Morreel, K.; Ralph, J.; Boerjan, W. Lignin biosynthesis and structure. *Plant Physiol.* **2010**, *153*, 895−905.

(316) Wang, H.-M.; Ma, C.-Y.; Li, H.-Y.; Chen, T.-Y.; Wen, J.-L.; Cao, X.-F.; Wang, X.-L.; Yuan, T.-Q.; Sun, R.-C. Structural variations of lignin macromolecules from early growth stages of poplar cell walls. *ACS Sustainable Chem. Eng.* **2020**, *8*, 1813−1822.

(317) Capanema, E. A.; Balakshin, M. Y.; Kadla, J. F. A comprehensive approach for quantitative lignin characterization by NMR spectroscopy. *J. Agric. Food Chem.* **2004**, *52*, 1850−1860.

(318) Cheng, K.; Sorek, H.; Zimmermann, H.; Wemmer, D. E.; Pauly, M. Solution-state 2D NMR spectroscopy of plant cell walls enabled by a dimethylsulfoxide-d$_6$/1-ethyl-3-methylimidazolium acetate solvent. *Anal. Chem.* **2013**, *85*, 3213−3221.

(319) Haw, J. F.; Maciel, G. E.; Schroeder, H. A. Carbon-13 nuclear magnetic resonance spectrometric study of wood and wood pulping with cross polarization and magic-angle spinning. *Anal. Chem.* **1984**, *56*, 1323−1329.

(320) Love, G.; Snape, C.; Jarvis, M. Determination of the aromatic lignin content in oak wood by quantitative solid state ^{13}C-NMR. *Biopolymers* **1992**, *32*, 1187−1192.

(321) Yasuda, S.; Fukushima, K.; Kakehi, A. Formation and chemical structures of acid-soluble lignin I: sulfuric acid treatment time and acid-soluble lignin content of hardwood. *J. Wood Sci.* **2001**, *47*, 69−72.

(322) Matsushita, Y.; Kakehi, A.; Miyawaki, S.; Yasuda, S. Formation and chemical structures of acid-soluble lignin II: reaction of aromatic nuclei model compounds with xylan in the presence of a counterpart for condensation, and behavior of lignin model compounds with guaiacyl and syringyl nuclei in 72% sulfuric acid. *J. Wood Sci.* **2004**, *50*, 136−141.

(323) Fu, L.; McCallum, S. A.; Miao, J.; Hart, C.; Tudryn, G. J.; Zhang, F.; Linhardt, R. J. Rapid and accurate determination of the lignin content of lignocellulosic biomass by solid-state NMR. *Fuel* **2015**, *141*, 39−45.

(324) Happs, R. M.; Addison, B.; Doeppke, C.; Donohoe, B. S.; Davis, M. F.; Harman-Ware, A. E. Comparison of methodologies used to determine aromatic lignin unit ratios in lignocellulosic biomass. *Biotechnol. Biofuels* **2021**, *14*, 58.

(325) Evstigneyev, E. I.; Mazur, A. S.; Kalugina, A. V.; Pranovich, A. V.; Vasilyev, A. V. Solid-State ^{13}C CP/MAS NMR for Alkyl-O-Aryl bond determination in lignin preparations. *J. Wood Chem. Technol.* **2018**, *38*, 137−148.

(326) Porto, D. S.; Forim, M. R.; Costa, E. S.; Fernandes, J. B.; da Silva, M. F. Evaluation of lignins of trunk and roots from *Citrus sinensis* L. Osbeck: a large available Brazilian biomass. *J. Braz. Chem. Soc.* **2021**, *32*, 29−39.

(327) Cipriano, D. F.; Chinelatto, L. S.; Nascimento, S. A.; Rezende, C. A.; de Menezes, S. M. C.; Freitas, J. C. C. Potential and limitations of ^{13}C CP/MAS NMR spectroscopy to determine the lignin content of lignocellulosic feedstock. *Biomass Bioenergy* **2020**, *142*, 105792.

(328) Gao, X.; Laskar, D. D.; Zeng, J.; Helms, G. L.; Chen, S. A ^{13}C CP/MAS-based nondegradative method for lignin content analysis. *ACS Sustainable Chem. Eng.* **2015**, *3*, 153−162.

(329) Perras, F. A.; Luo, H.; Zhang, X.; Mosier, N. S.; Pruski, M.; Abu-Omar, M. M. Atomic-level structure characterization of biomass pre- and post-lignin treatment by dynamic nuclear polarization-enhanced solid-state NMR. *J. Phys. Chem. A* **2017**, *121*, 623−630.

(330) Giummarella, N.; Pu, Y.; Ragauskas, A. J.; Lawoko, M. A critical review on the analysis of lignin carbohydrate bonds. *Green Chem.* **2019**, *21*, 1573−1595.

(331) Wilson, L.; Deligey, F.; Wang, T.; Cosgrove, D. J. Saccharide analysis of onion outer epidermal walls. *Biotechnol. Biofuels* **2021**, *14*, 66.

(332) Coutinho, I. D.; Moraes, T. B.; Mertz-Henning, L. M.; Nepomuceno, A. L.; Giordani, W.; Marcolino-Gomes, J.; Santagneli, S.; Colnago, L. A. Integrating high-resolution and solid-state magic angle spinning NMR spectroscopy and a transcriptomic analysis of soybean tissues in response to water deficiency. *Phytochem. Anal.* **2017**, *28*, 529−540.

(333) Deborde, C.; Fontaine, J.-X.; Jacob, D.; Botana, A.; Nicaise, V.; Richard-Forget, F.; Lecomte, S.; Decourtil, C.; Hamade, K.; Mesnard, F. Optimizing 1D ¹H-NMR profiling of plant samples for high throughput analysis: Extract preparation, standardization, automation and spectra processing. *Metabolomics* **2019**, *15*, 28.

(334) Tian, H.; Lam, S. M.; Shui, G. Metabolomics, a powerful tool for agricultural research. *Int. J. Mol. Sci.* **2016**, *17*, 1871.

(335) Ibragimova, N.; Mokshina, N.; Ageeva, M.; Gurjanov, O.; Mikshina, P. Rearrangement of the cellulose-enriched cell wall in flax phloem fibers over the course of the gravitropic reaction. *Int. J. Mol. Sci.* **2020**, *21*, 5322.

(336) Bourmaud, A.; Siniscalco, D.; Foucat, L.; Goudenhooft, C.; Falourd, X.; Pontoire, B.; Arnould, O.; Beaugrand, J.; Baley, C. Evolution of flax cell wall ultrastructure and mechanical properties during the retting step. *Carbohydr. Polym.* **2019**, *206*, 48−56.

(337) Reddy, K. O.; Maheswari, C. U.; Dhlamini, M.; Mothudi, B.; Kommula, V.; Zhang, J.; Zhang, J.; Rajulu, A. V. Extraction and characterization of cellulose single fibers from native african napier grass. *Carbohydr. Polym.* **2018**, *188*, 85−91.

(338) Kang, X.; Zhao, W.; Widanage, M. C. D.; Kirui, A.; Ozdenvar, U.; Wang, T. CCMRD: a solid-state NMR database for complex carbohydrates. *J. Biomol. NMR* **2020**, *74*, 239−245.

(339) Walker, T. W.; Kuch, N.; Vander Meulen, K. A.; Clewett, C. F.; Huber, G. W.; Fox, B. G.; Dumesic, J. A. Solid-state NMR studies of solvent-mediated, acid-catalyzed woody biomass pretreatment for enzymatic conversion of residual cellulose. *ACS Sustainable Chem. Eng.* **2020**, *8*, 6551−6563.

(340) Tsuchida, M.; Yamaguchi, H.; Katayama, N.; Sato, Y.; Kawashima, W.; Kasai, M. Structural changes in cell wall of Japanese radish accompanied by release of rhamnogalacturonan during pressure cooker heating. *Food Chem.* **2021**, *349*, 129117.

(341) Hossain, A.; Rahaman, M. S.; Lee, D.; Phung, T. K.; Canlas, C. G.; Simmons, B. A.; Renneckar, S.; Reynolds, W.; George, A.; Tulaphol, S. Enhanced softwood cellulose accessibility by H₃PO₄ pretreatment: high sugar yield without compromising lignin integrity. *Ind. Eng. Chem. Res.* **2020**, *59*, 1010−1024.

(342) Nishida, M.; Tanaka, T.; Miki, T.; Hayakawa, Y.; Kanayama, K. Instrumental analyses of nanostructures and interactions with water molecules of biomass constituents of Japanese cypress. *Cellulose* **2017**, *24*, 5295−5312.

(343) Chen, M.-J.; Zhang, X.-Q.; Matharu, A.; Melo, E.; Li, R.-M.; Liu, C.-F.; Shi, Q.-S. Monitoring the crystalline structure of sugar cane bagasse in aqueous ionic liquids. *ACS Sustainable Chem. Eng.* **2017**, *5*, 7278−7283.

(344) Nishida, M.; Tanaka, T.; Miki, T.; Hayakawa, Y.; Kanayama, K. Integrated analysis of modified Japanese cypress using solid-state NMR spectra and nuclear magnetic relaxation times. *Cellulose* **2019**, *26*, 3625−3642.

(345) Jiang, J.; Hu, Y.; Tian, Z.; Chen, K.; Ge, S.; Xu, Y.; Tian, D.; Yang, J. Development of a rapid method for the quantification of cellulose in tobacco by ¹³C CP/MAS NMR. *Carbohydr. Polym.* **2016**, *135*, 121−127.

(346) Thimm, J. C.; Burritt, D. J.; Sims, I. M.; Newman, R. H.; Ducker, W. A.; Melton, L. D. Celery (*Apium graveolens*) parenchyma cell walls: cell walls with minimal xyloglucan. *Physiol. Plant.* **2002**, *116*, 164−171.

(347) Chen, D.; Harris, P. J.; Sims, I. M.; Zujovic, Z.; Melton, L. D. Polysaccharide compositions of collenchyma cell walls from celery (*Apium graveolens L.*) petioles. *BMC Plant Biol.* **2017**, *17*, 104.

(348) Chen, D.; Melton, L. D.; Zujovic, Z.; Harris, P. J. Developmental changes in collenchyma cell-wall polysaccharides in celery (*Apium graveolens L.*) petioles. *BMC Plant Biol.* **2019**, *19*, 81.

(349) Ha, M.-A.; Viëtor, R. J.; Jardine, G. D.; Apperley, D. C.; Jarvis, M. C. Conformation and mobility of the arabinan and galactan side-chains of pectin. *Phytochemistry* **2005**, *66*, 1817−1824.

(350) Zujovic, Z.; Chen, D.; Melton, L. D. Comparison of celery (*Apium graveolens L.*) collenchyma and parenchyma cell wall polysaccharides enabled by solid-state ¹³C NMR. *Carbohydr. Res.* **2016**, *420*, 51−57.

(351) Viger-Gravel, J.; Lan, W.; Pinon, A. C.; Berruyer, P.; Emsley, L.; Bardet, M.; Luterbacher, J. Topology of pretreated wood fibers using dynamic nuclear polarization. *J. Phys. Chem. C* **2019**, *123*, 30407−30415.

(352) Berruyer, P.; Gericke, M.; Moutzouri, P.; Jakobi, D.; Bardet, M.; Karlson, L.; Schantz, S.; Heinze, T.; Emsley, L. Advanced characterization of regioselectively substituted methylcellulose model compounds by DNP enhanced solid-state NMR spectroscopy. *Carbohydr. Polym.* **2021**, *262*, 117944.

(353) Xie, Y.; Liu, Y.; Jiang, C.; Wu, H.; Bi, S. The Existence of Cellulose and Lignin Chemical Connections in Ginkgo Traced by ²H-¹³C Dual Isotopes. *BioResources* **2020**, *15*, 9028−9044.

(354) Cegelski, L.; O'Connor, R. D.; Stueber, D.; Singh, M.; Poliks, B.; Schaefer, J. Plant cell-wall cross-links by REDOR NMR spectroscopy. *J. Am. Chem. Soc.* **2010**, *132*, 16052−16057.

(355) Denning, D. W. Invasive aspergillosis. *Clin. Infect. Dis.* **1998**, *26*, 781−803.

(356) Denning, D. W. Therapeutic outcome in invasive aspergillosis. *Clin. Infect. Dis.* **1996**, *23*, 608−615.

(357) Sague, C. M. B.; Jarvis, W. R. Secular trends in the epidemiology of nosocomial fungal-infections in the United-States, 1980−1990. *J. Infect. Dis.* **1993**, *167*, 1247−1251.

(358) Andriole, V. T. Infections with *Aspergillus* Species. *Clin. Infect. Dis.* **1993**, *17*, 481−486.

(359) Latge, J. P. *Aspergillus fumigatus* and aspergillosis. *Clin. Microbiol. Rev.* **1999**, *12*, 310−350.

(360) Marr, K. A.; Boeckh, M.; Carter, R. A.; Kim, H. W.; Corey, L. Combination antifungal therapy for invasive aspergillosis. *Clin. Infect. Dis.* **2004**, *39*, 797−802.

(361) Andes, D. R.; Safdar, N.; Baddley, J. W.; Playford, G.; Reboli, A. C.; Rex, J. H.; Sobel, J. D.; Pappas, P. G.; Kullberg, B. J.; Group, f. t. M. S. Impact of treatment strategy on outcomes in patients with candidemia and other forms of invasive candidiasis: a patient-level quantitative review of randomized trials. *Clin. Infect. Dis.* **2012**, *54*, 1110−1122.

(362) Perfect, J. R. The antifungal pipeline: a reality check. *Nat. Rev. Drug Discovery* **2017**, *16*, 603−616.

(363) Le, T.; Van Kinh, N.; Cuc, N. T. K.; Tung, N. L. N.; Lam, N. T.; Thuy, P. T. T.; Cuong, D. D.; Phuc, P. T. H.; Vinh, V. H.; Hanh, D. T. H.; et al. A trial of itraconazole or amphotericin B for HIV-associated talaromycosis. *N. Engl. J. Med.* **2017**, *376*, 2329−2340.

(364) Ghannoum, M. A.; Rice, L. B. Antifungal agents: mode of action, mechanisms of resistance, and correlation of these mechanisms with bacterial resistance. *Clin. Microbiol. Rev.* **1999**, *12*, 501−517.

(365) Gray, K. C.; Palacios, D. S.; Dailey, I.; Endo, M. M.; Uno, B. E.; Wilcock, B. C.; Burke, M. D. Amphotericin primarily kills yeast by simply binding ergosterol. *Proc. Natl. Acad. Sci. U. S. A.* **2012**, *109*, 2234−2239.

(366) Marco, F.; Pfaller, M. A.; Messer, S. A.; Jones, R. N. Antifungal activity of a new triazole, voriconazole (UK-109,496), compared with three other antifungal agents tested against clinical isolates of filamentous fungi. *Med. Mycol.* **1998**, *36*, 433−436.

(367) Odds, F. C.; Brown, A. J. P.; Gow, N. A. R. Antifungal agents: mechanisms of action. *Trends Microbiol.* **2003**, *11*, 272−279.

(368) Perlin, D. S. Current perspectives on echinocandin class drugs. *Future Microbiol.* **2011**, *6*, 441−457.

(369) Aruanno, M.; Glampedakis, E.; Lamoth, F. Echinocandins for the treatment of invasive aspergillosis: from laboratory to bedside. *Antimicrob. Agents Chemother.* **2019**, *63*, e00399-19.

(370) Loiko, V.; Wagener, J. The paradoxical effect of echinocandins in *Aspergillus fumigatus* relies on recovery of the β-1,3-glucan synthase fks1. *Antimicrob. Agents Chemother.* **2017**, *61*, e01690-16.

(371) Wagener, J.; Loiko, V. Recent insights into the paradoxical effect of echinocandins. *J. Fungi* **2018**, *4*, 5.

(372) Rinaudo, M. Chitin and chitosan: properties and applications. *Prog. Polym. Sci.* **2006**, *31*, 603−632.

(373) Bowman, S. M.; Free, S. J. The structure and synthesis of the fungal cell wall. *BioEssays* **2006**, *28*, 799−808.

(374) Latgé, J.-P.; Chamilos, G. *Aspergillus fumigatus* and aspergillosis in 2019. *Clin. Microbiol. Rev.* **2019**, *33*, e00140-00118.

(375) Gastebois, A.; Clavaud, C.; Aimanianda, V.; Latgé, J.-P. *Aspergillus fumigatus*: cell wall polysaccharides, their biosynthesis and organization. *Future Microbiol.* **2009**, *4*, 583−595.

(376) Orlean, P. Architecture and biosynthesis of the *Saccharomyces cerevisiae* cell wall. *Genetics* **2012**, *192*, 775−818.

(377) Lipke, P. N.; Ovalle, R. Cell wall architecture in yeast: new structure and new challenges. *J. Bacteriol.* **1998**, *180*, 3735−3740.

(378) Brown, J. A.; Catley, B. J. Monitoring polysaccharide synthesis in *Candida albicans*. *Carbohydr. Res.* **1992**, *227*, 195−202.

(379) Cherniak, R.; Sundstrom, J. B. Polysaccharide antigens of the capsule of *Cryptococcus neoforman*. *Infect. Immun.* **1994**, *62*, 1507−1512.

(380) Cortés, J. C. G.; Curto, M. Á.; Carvalho, V. S. D.; Pérez, P.; Ribas, J. C. The fungal cell wall as a target for the development of new antifungal therapies. *Biotechnol. Adv.* **2019**, *37*, 107352.

(381) Latgé, J.-P.; Beauvais, A. Functional duality of the cell wall. *Curr. Opin. Microbiol.* **2014**, *20*, 111−117.

(382) Wang, Z. A.; Li, L. X.; Doering, T. L. Unraveling synthesis of the cryptococcal cell wall and capsule. *Glycobiology* **2018**, *28*, 719−730.

(383) Kollár, R.; Petrakova, E.; Ashwell, G.; Robbins, P. W.; Cabib, E. Architecture of the yeast-cell wall: the linkage between chitin and $\beta(1\rightarrow3)$-glucan. *J. Biol. Chem.* **1995**, *270*, 1170−1178.

(384) Kollár, R.; Reinhold, B. B.; Petrakova, E.; Yeh, H. J. C.; Ashwell, G.; Drgonova, J.; Kapteyn, J. C.; Klis, F. M.; Cabib, E. Architecture of the yeast cell wall - $\beta(1\rightarrow6)$-glucan interconnects mannoprotein, $\beta(1\rightarrow3)$-glucan, and chitin. *J. Biol. Chem.* **1997**, *272*, 17762−17775.

(385) Latgé, J. P.; Kobayashi, H.; Debeaupuis, J. P.; Diaquin, M.; Sarfati, J.; Wieruszeski, J. M.; Parra, E.; Bouchara, J. P.; Fournet, B. Chemical and immunological characterization of the extracellular galactomannan of Aspergillus fumigatus. *Infect. Immun.* **1994**, *62*, 5424−5433.

(386) Gressler, M.; Heddergott, C.; N'Go, I. C.; Renga, G.; Oikonomou, V.; Moretti, S.; Coddeville, B.; Gaifem, J.; Silvestre, R.; Romani, L.; et al. Definition of the anti-inflammatory oligosaccharides derived from the galactosaminogalactan (GAG) from *Aspergillus fumigatus*. *Front. Cell. Infect. Microbiol.* **2019**, *9*, 365.

(387) Chakraborty, A.; Fernando, L. D.; Fang, W.; Dickwella Widanage, M. C.; Wei, P.; Jin, C.; Fontaine, T.; Latgé, J. P.; Wang, T. A molecular vision of fungal cell wall organization by functional genomics and solid-state NMR. *Nat. Commun.* **2021**, *12*, 6346.

(388) Ohm, R. A.; de Jong, J. F.; Lugones, L. G.; Aerts, A.; Kothe, E.; Stajich, J. E.; de Vries, R. P.; Record, E.; Levasseur, A.; Baker, S. E.; et al. Genome sequence of the model mushroom *Schizophyllum commune*. *Nat. Biotechnol.* **2010**, *28*, 957−963.

(389) Sietsma, J. H.; Wessels, J. G. H. Chemical analysis of the hyphal walls of *Schizophyllum commune*. *Biochim. Biophys. Acta, Gen. Subj.* **1977**, *496*, 225−239.

(390) Sietsma, J. H.; Wessels, J. G. H. Solubility of $(1\rightarrow3)$-β-D/$(1\rightarrow6)$-β-D-glucan in fungal walls: importance of presumed linkage between glucan and chitin. *Microbiology* **1981**, *125*, 209−212.

(391) van der Valk, P.; Marchant, R.; Wessels, J. G. H. Ultrastructural localization of polysaccharides in the wall and septum of the basidiomycete *Schizophyllum commune*. *Exp. Mycol.* **1977**, *1*, 69−82.

(392) Sietsma, J. H.; Wessels, J. G. H. Evidence for covalent linkages between chitin and β-glucan in a fungal wall. *J. Gen. Microbiol.* **1979**, *114*, 99−108.

(393) Li, Y.; Sun, H.; Zhu, X.; Bian, C.; Wang, Y.; Si, S. Identification of new antifungal agents targeting chitin synthesis by a chemical-genetic method. *Molecules* **2019**, *24*, 3155.

(394) Fernando, L. D.; Dickwella Widanage, M. C.; Penfield, J.; Lipton, A. S.; Washton, N.; Latge, J.-P.; Wang, P.; Zhang, L.; Wang, T. Structural polymorphism of chitin and chitosan in fungal cell walls from solid-state NMR and principal component analysis. *Front. Mol. Biosci.* **2021**, *8*, 727053.

(395) Nielsen, K.; Cox, G. M.; Litvintseva, A. P.; Mylonakis, E.; Malliaris, S. D.; Benjamin, D. K.; Giles, S. S.; Mitchell, T. G.; Casadevall, A.; Perfect, J. R.; et al. *Cryptococcus neoformans* α strains preferentially disseminate to the central nervous system during coinfection. *Infect. Immun.* **2005**, *73*, 4922−4933.

(396) Rajasingham, R.; Smith, R. M.; Park, B. J.; Jarvis, J. N.; Govender, N. P.; Chiller, T. M.; Denning, D. W.; Loyse, A.; Boulware, D. R. Global burden of disease of HIV-associated cryptococcal meningitis: an updated analysis. *Lancet Infect. Dis.* **2017**, *17*, 873−881.

(397) Chrissian, C.; Lin, C. P.-C.; Camacho, E.; Casadevall, A.; Neiman, A. M.; Stark, R. E. Unconventional constituents and shared molecular architecture of the melanized cell wall of *C. neoformans* and spore wall of *S. cerevisiae*. *J. Fungi* **2020**, *6*, 329.

(398) Eisenman, H. C.; Casadevall, A. Synthesis and assembly of fungal melanin. *Appl. Microbiol. Biotechnol.* **2012**, *93*, 931−940.

(399) Ikeda, R.; Sugita, T.; Jacobson, E. S.; Shinoda, T. Effects of melanin upon susceptibility of *Cryptococcus* to antifungals. *Microbiol. Immunol.* **2003**, *47*, 271−277.

(400) Nosanchuk, J. D.; Valadon, P.; Feldmesser, M.; Casadevall, A. Melanization of *Cryptococcus neoformans* in murine Iinfection. *Mol. Cell. Biol.* **1999**, *19*, 745−750.

(401) Eisenman, H. C.; Nosanchuk, J. D.; Webber, J. B. W.; Emerson, R. J.; Camesano, T. A.; Casadevall, A. Microstructure of cell wall-associated melanin in the human pathogenic fungus *Cryptococcus neoformans*. *Biochemistry* **2005**, *44*, 3683−3693.

(402) Camacho, E.; Vij, R.; Chrissian, C.; Prados-Rosales, R.; Gil, D.; O'Meally, R. N.; Cordero, R. J. B.; Cole, R. N.; McCaffery, J. M.; Stark, R. E.; et al. The structural unit of melanin in the cell wall of the fungal pathogen *Cryptococcus neoformans*. *J. Biol. Chem.* **2019**, *294*, 10471−10489.

(403) Chatterjee, S.; Prados-Rosales, R.; Frases, S.; Itin, B.; Casadevall, A.; Stark, R. E. Using solid-state NMR To Monitor the Molecular Consequences of Cryptococcus neoformans Melanization with different catecholamine precursors. *Biochemistry* **2012**, *51*, 6080−6088.

(404) Chatterjee, S.; Prados-Rosales, R.; Tan, S.; Phan, V. C.; Chrissian, C.; Itin, B.; Wang, H.; Khajo, A.; Magliozzo, R. S.; Casadevall, A.; et al. The melanization road more traveled by: Precursor substrate effects on melanin synthesis in cell-free and fungal cell systems. *J. Biol. Chem.* **2018**, *293*, 20157−20168.

(405) Chatterjee, S.; Prados-Rosales, R.; Itin, B.; Casadevall, A.; Stark, R. E. Solid-state NMR reveals the carbon-based molecular architecture of *Cryptococcus neoformans* fungal eumelanins in the cell wall. *J. Biol. Chem.* **2015**, *290*, 13779−13790.

(406) Free, S. J. Chapter two - fungal cell wall organization and biosynthesis. *Adv. Genet.* **2013**, *81*, 33−82.

(407) Crocker, E.; Patel, A. B.; Eilers, M.; Jayaraman, S.; Getmanova, E.; Reeves, P. J.; Ziliox, M.; Khorana, H. G.; Sheves, M.; Smith, S. O. Dipolar assisted rotational resonance NMR of tryptophan and tyrosine in rhodopsin. *J. Biomol. NMR* **2004**, *29*, 11−20.

(408) Simon, J. D.; Peles, D. N. The red and the black. *Acc. Chem. Res.* **2010**, *43*, 1452−1460.

(409) Della Vecchia, N. F.; Avolio, R.; Alfè, M.; Errico, M. E.; Napolitano, A.; d'Ischia, M. Building-block diversity in polydopamine underpins a multifunctional eumelanin-type platform tunable through a quinone control point. *Adv. Funct. Mater.* **2013**, *23*, 1331−1340.

(410) Schnitzer, M.; Chan, Y. K. Structural characteristics of a fungal melanin and a soil humic acid. *Soil Sci. Soc. Am. J.* **1986**, *50*, 67−71.

(411) Knicker, H.; Almendros, G.; González-Vila, F. J.; Lüdemann, H. D.; Martin, F. ^{13}C and ^{15}N NMR analysis of some fungal melanins in

comparison with soil organic matter. *Org. Geochem.* **1995**, *23*, 1023−1028.

(412) Zhong, J. Y.; Frases, S.; Wang, H.; Casadevall, A.; Stark, R. E. Following fungal melanin biosynthesis with solid-state NMR: biopolyrner molecular structures and possible connections to cell-wall polysaccharides. *Biochemistry* **2008**, *47*, 4701−4710.

(413) Chrissian, C.; Camacho, E.; Fu, M. S.; Prados-Rosales, R.; Chatterjee, S.; Cordero, R. J. B.; Lodge, J. K.; Casadevall, A.; Stark, R. E. Melanin deposition in two *Cryptococcus* species depends on cell-wall composition and flexibility. *J. Biol. Chem.* **2020**, *295*, 1815−1828.

(414) Neiman, A. M. Sporulation in the budding yeast *Saccharomyces cerevisiae*. *Genetics* **2011**, *189*, 737−765.

(415) Anderson, T. M.; Clay, M. C.; Cioffi, A. G.; Diaz, K. A.; Hisao, G. S.; Tuttle, M. D.; Nieuwkoop, A. J.; Comellas, G.; Maryum, N.; Wang, S.; et al. Amphotericin forms an extramembranous and fungicidal sterol sponge. *Nat. Chem. Biol.* **2014**, *10*, 400−406.

(416) Ermishkin, L. N.; Kasumov, K. M.; Potzeluyev, V. M. Single ionic channels induced in lipid bilayers by polyene antibiotics amphotericin B and nystatine. *Nature* **1976**, *262*, 698−699.

(417) Cereghetti, D. M.; Carreira, E. M. Amphotericin B: 50 years of chemistry and biochemistry. *Synthesis* **2006**, *2006*, 0914−0942.

(418) Fernandez-Lopez, S.; Kim, H.-S.; Choi, E. C.; Delgado, M.; Granja, J. R.; Khasanov, A.; Kraehenbuehl, K.; Long, G.; Weinberger, D. A.; Wilcoxen, K. M.; et al. Antibacterial agents based on the cyclic D,L-*α*-peptide architecture. *Nature* **2001**, *412*, 452−455.

(419) Mouri, R.; Konoki, K.; Matsumori, N.; Oishi, T.; Murata, M. Complex formation of amphotericin B in sterol-containing membranes as evidenced by surface plasmon resonance. *Biochemistry* **2008**, *47*, 7807−7815.

(420) Murata, M.; Kasai, Y.; Umegawa, Y.; Matsushita, N.; Tsuchikawa, H.; Matsumori, N.; Oishi, T. Ion channel complex of antibiotics as viewed by NMR. *Pure Appl. Chem.* **2009**, *81*, 1123−1129.

(421) Matsumori, N.; Sawada, Y.; Murata, M. Large molecular assembly of amphotericin B formed in ergosterol-containing membrane evidenced by solid-state NMR of intramolecular bridged derivative. *J. Am. Chem. Soc.* **2006**, *128*, 11977−11984.

(422) Matsuoka, S.; Ikeuchi, H.; Umegawa, Y.; Matsumori, N.; Murata, M. Membrane interaction of amphotericin B as single-length assembly examined by solid state NMR for uniformly ^{13}C-enriched agent. *Bioorg. Med. Chem.* **2006**, *14*, 6608−6614.

(423) Umegawa, Y.; Nakagawa, Y.; Tahara, K.; Tsuchikawa, H.; Matsumori, N.; Oishi, T.; Murata, M. Head-to-tail interaction between amphotericin B and ergosterol occurs in hydrated phospholipid membrane. *Biochemistry* **2012**, *51*, 83−89.

(424) de Kruijff, B.; Demel, R. A. Polyene antibiotic-sterol interactions in membranes of *Acholeplasma laidlawii* cells and lecithin liposomes. 3. Molecular structure of the polyene antibiotic-cholesterol complexes. *Biochim. Biophys. Acta, Biomembr.* **1974**, *339*, 57−70.

(425) Nakagawa, Y.; Umegawa, Y.; Matsushita, N.; Yamamoto, T.; Tsuchikawa, H.; Hanashima, S.; Oishi, T.; Matsumori, N.; Murata, M. The structure of the bimolecular complex between amphotericin B and ergosterol in membranes is stabilized by face-to-face van der Waals interaction with their rigid cyclic cores. *Biochemistry* **2016**, *55*, 3392−3402.

(426) Ostrosky-Zeichner, L.; Casadevall, A.; Galgiani, J. N.; Odds, F. C.; Rex, J. H. An insight into the antifungal pipeline: selected new molecules and beyond. *Nat. Rev. Drug Discovery* **2010**, *9*, 719−727.

(427) Foglia, F.; Drake, A. F.; Terry, A. E.; Rogers, S. E.; Lawrence, M. J.; Barlow, D. J. Small-angle neutron scattering studies of the effects of amphotericin B on phospholipid and phospholipid−sterol membrane structure. *Biochim. Biophys. Acta, Biomembr.* **2011**, *1808*, 1574−1580.

(428) Reichhardt, C.; Joubert, L. M.; Clemons, K. V.; Stevens, D. A.; Cegelski, L. Integration of electron microscopy and solid-state NMR analysis for new views and compositional parameters of *Aspergillus fumigatus* biofilms. *Med. Mycol.* **2019**, *57*, S239−s244.

(429) Pfaller, M. A.; Diekema, D. J. Epidemiology of invasive candidiasis: a persistent public health problem. *Clin. Microbiol. Rev.* **2007**, *20*, 133−163.

(430) White, T. C.; Marr, K. A.; Bowden, R. A. Clinical, cellular, and molecular factors that contribute to antifungal drug resistance. *Clin. Microbiol. Rev.* **1998**, *11*, 382−402.

(431) Mann, D. G.; Vanormelingen, P. An inordinate fondness? The number, distributions, and origins of diatom species. *J. Eukaryotic Microbiol.* **2013**, *60*, 414−420.

(432) Guiry, M. D. How many species of algae are there? *J. Phycol.* **2012**, *48*, 1057−1063.

(433) Flombaum, P.; Gallegos, J.; Gordillo, R.; Rincón, J.; Zabala, L.; Jiao, N.; Karl, D.; Li, W.; Lomas, M.; Veneziano, D.; et al. Present and future global distributions of the marine Cyanobacteria *Prochlorococcus* and *Synechococcus*. *Proc. Natl. Acad. Sci. U. S. A.* **2013**, *110*, 9824−9829.

(434) Van Den Hoek, C.; Mann, D. G.; Jahns, H. M. *Algae: an introduction to phycology*; Cambridge University Press: Cambridge ; New York, 1995.

(435) Round, F. E. *The ecology of algae*; Cambridge University Press: Cambridge, U.K., 1981; pp 1−653.

(436) Lyon, B. R.; Mock, T. Polar microalgae: new approaches towards understanding adaptations to an extreme and changing environment. *Biology* **2014**, *3*, 56−80.

(437) Cardon, Z. G.; Gray, D. W.; Lewis, L. A. The green algal underground: evolutionary secrets of desert cells. *BioScience* **2008**, *58*, 114−122.

(438) Tesson, S. V. M.; Skjøth, C. A.; Šantl-Temkiv, T.; Löndahl, J. Airborne microalgae: insights, opportunities, and challenges. *Appl. Environ. Microbiol.* **2016**, *82*, 1978.

(439) Radakovits, R.; Jinkerson, R. E.; Darzins, A.; Posewitz, M. C. Genetic engineering of algae for enhanced biofuel production. *Eukaryotic Cell* **2010**, *9*, 486−501.

(440) Goncalves, E. C.; Koh, J.; Zhu, N.; Yoo, M.-J.; Chen, S.; Matsuo, T.; Johnson, J. V.; Rathinasabapathi, B. Nitrogen starvation-induced accumulation of triacylglycerol in the green algae: evidence for a role for ROC40, a transcription factor involved in circadian rhythm. *Plant J.* **2016**, *85*, 743−757.

(441) Barkia, I.; Saari, N.; Manning, S. R. Microalgae for high-value products towards human health and nutrition. *Mar. Drugs* **2019**, *17*, 304.

(442) Le Costaouëc, T.; Unamunzaga, C.; Mantecon, L.; Helbert, W. New structural insights into the cell-wall polysaccharide of the diatom *Phaeodactylum tricornutum*. *Algal Res.* **2017**, *26*, 172−179.

(443) Berteau, O.; Mulloy, B. Sulfated fucans, fresh perspectives: structures, functions, and biological properties of sulfated fucans and an overview of enzymes active toward this class of polysaccharide. *Glycobiology* **2003**, *13*, 29R−40R.

(444) Pomin, V. H.; Mourão, P. A. S. Structure, biology, evolution, and medical importance of sulfated fucans and galactans. *Glycobiology* **2008**, *18*, 1016−1027.

(445) Barry, V. C.; Dillon, T.; Hawkins, B.; O'Colla, P. The xylan of *Rhodymenia palmata*. *Nature* **1950**, *166*, 788−788.

(446) Bjorndal, H.; Eriksson, K.-E.; Garegg, P. J.; Lindberg, B.; Swan, B.; Westerdahl, A. Studies on the Xylan from the Red Seaweed Rhodymenia palmata. *Acta Chem. Scand.* **1965**, *19*, 2309−2315.

(447) Percival, E.; McDowell, R. H.; Husemann, E. *Chemistry and enzymology of marine algal polysaccharides*; Academic Press: London, New York, 1967.

(448) Mikkelsen, M. D.; Harholt, J.; Ulvskov, P.; Johansen, I. E.; Fangel, J. U.; Doblin, M. S.; Bacic, A.; Willats, W. G. T. Evidence for land plant cell wall biosynthetic mechanisms in charophyte green algae. *Ann. Bot.* **2014**, *114*, 1217−1236.

(449) Fry, S. C. Cell wall polysaccharide composition and covalent crosslinking. *Annu. Plant Rev.* **2010**, *41*, 1−42.

(450) Domozych, D. S.; Sørensen, I.; Popper, Z. A.; Ochs, J.; Andreas, A.; Fangel, J. U.; Pielach, A.; Sacks, C.; Brechka, H.; Ruisi-Besares, P.; et al. Pectin metabolism and assembly in the cell wall of the charophyte green alga *Penium margaritaceum*. *Plant Physiol.* **2014**, *165*, 105−118.

(451) Deniaud-Bouët, E.; Kervarec, N.; Michel, G.; Tonon, T.; Kloareg, B.; Hervé, C. Chemical and enzymatic fractionation of cell walls from fucales: insights into the structure of the extracellular matrix of brown algae. *Ann. Bot.* **2014**, *114*, 1203−1216.

(452) Zang, X.; Nguyen, R. T.; Harvey, H. R.; Knicker, H.; Hatcher, P. G. Preservation of proteinaceous material during the degradation of the green alga *Botryococcus braunii*: A solid-state 2D ^{15}N ^{13}C NMR spectroscopy study. *Geochim. Cosmochim. Acta* **2001**, *65*, 3299−3305.

(453) Weich, R. G.; Lundberg, P.; Vogel, H. J.; Jensén, P. Phosphorus-31 NMR studies of cell wall-associated calcium-phosphates in *Ulva lactuca*. *Plant Physiol.* **1989**, *90*, 230−236.

(454) La Vars, S. M.; Johnston, M. R.; Hayles, J.; Gascooke, J. R.; Brown, M. H.; Leterme, S. C.; Ellis, A. V. ^{29}Si{^{1}H} CP-MAS NMR comparison and ATR-FTIR spectroscopic analysis of the diatoms *Chaetoceros muelleri* and *Thalassiosira pseudonana* grown at different salinities. *Anal. Bioanal. Chem.* **2013**, *405*, 3359−3365.

(455) Lahaye, M.; Robic, A. Structure and functional properties of ulvan, a polysaccharide from green seaweeds. *Biomacromolecules* **2007**, *8*, 1765−1774.

(456) Michel, G.; Tonon, T.; Scornet, D.; Cock, J. M.; Kloareg, B. The cell wall polysaccharide metabolism of the brown alga *Ectocarpus siliculosus*. Insights into the evolution of extracellular matrix polysaccharides in eukaryotes. *New Phytol.* **2010**, *188*, 82−97.

(457) Lahaye, M.; Alvarez-Cabal Cimadevilla, E.; Kuhlenkamp, R.; Quemener, B.; Lognoné, V.; Dion, P. Chemical composition and ^{13}C NMR spectroscopic characterisation of ulvans from *Ulva* (Ulvales, Chlorophyta). *J. Appl. Phycol.* **1999**, *11*, 1.

(458) Llanes, F.; Sauriol, F.; Morin, F. G.; Perlin, A. S. An examination of sodium alginate from *Sargassum* by NMR spectroscopy. *Can. J. Chem.* **1997**, *75*, 585−590.

(459) Miller, I.; Blunt, J. Evaluation of the Structure of the Polysaccharides from *Chondria macrocarpa* and *Ceramium rubrum* as determined by ^{13}C NMR Spectroscopy. *Bot. Mar.* **2002**, *45*, 1−8.

(460) Shams El-Din, N. G.; Shaltout, N. A.; Ghazal, M. A.; Ali, A. E.; Beltagy, D. M. Chemical pretreatment of *Ulva fasciata* cell wall for enhancing biodiesel yield and properties. *Egypt. J. Aquat. Biol. Fish.* **2020**, *24*, 103−125.

(461) Soleymani, F.; Khani, M. H.; Pahlavanzadeh, H.; Manteghian, M. Study of cobalt (II) biosorption on Sargassum sp. by experimental design methodology. *Int. J. Environ. Sci. Technol.* **2015**, *12*, 1907−1922.

(462) Chandler, C. J.; Wilts, B. D.; Vignolini, S.; Brodie, J.; Steiner, U.; Rudall, P. J.; Glover, B. J.; Gregory, T.; Walker, R. H. Structural colour in *Chondrus crispus*. *Sci. Rep.* **2015**, *5*, 11645.

(463) Suresh, S. Biosynthesis and assemblage of extracellular cellulose by bacteria. *Handbook of environmental materials management*; Springer International Publishing: Cham, Switzerland, 2018; pp 1−43.

(464) Mihranyan, A. Cellulose from cladophorales green algae: From environmental problem to high-tech composite materials. *J. Appl. Polym. Sci.* **2011**, *119*, 2449−2460.

(465) Samiee, S.; Ahmadzadeh, H.; Hosseini, M.; Lyon, S. Chapter 17 - algae as a source of microcrystalline cellulose. *Advanced bioprocessing for alternative fuels, biobased chemicals, and bioproducts*; Woodhead Publishing: 2019; pp 331−350.

(466) Revol, J.-F. On the cross-sectional shape of cellulose crystallites in *Valonia ventricosa*. *Carbohydr. Polym.* **1982**, *2*, 123−134.

(467) Sugiyama, J.; Chanzy, H.; Revol, J. F. On the polarity of cellulose in the cell wall of *Valonia*. *Planta* **1994**, *193*, 260−265.

(468) Sugiyama, J.; Okano, T.; Yamamoto, H.; Horii, F. Transformation of *Valonia* cellulose crystals by an alkaline hydrothermal treatment. *Macromolecules* **1990**, *23*, 3196−3198.

(469) Yamamoto, H.; Horii, F. CPMAS carbon-13 NMR analysis of the crystal transformation induced for Valonia cellulose by annealing at high temperatures. *Macromolecules* **1993**, *26*, 1313−1317.

(470) Ibrahim, R.; Melton, L.; B,G, S.; Schroeder, R. Mannans in primary and secondary plant cell walls. *N. Z. J. For. Sci.* **2009**, *39*, 153−160.

(471) Estevez, J. M.; Fernández, P. V.; Kasulin, L.; Dupree, P.; Ciancia, M. Chemical and in situ characterization of macromolecular components of the cell walls from the green seaweed *Codium fragile*. *Glycobiology* **2009**, *19*, 212−228.

(472) Dunn, E. K.; Shoue, D. A.; Huang, X.; Kline, R. E.; MacKay, A. L.; Carpita, N. C.; Taylor, I. E.; Mandoli, D. F. Spectroscopic and

biochemical analysis of regions of the cell wall of the unicellular 'mannan weed'. *Plant Cell Physiol.* **2006**, *48*, 122−133.

(473) George, J.; Sabapathi, S. N. Cellulose nanocrystals: synthesis, functional properties, and applications. *Nanotechnol., Sci. Appl.* **2015**, *8*, 45−54.

(474) Hsieh, Y. S. Y.; Harris, P. J. Xylans of red and green algae: what is known about their structures and how they are synthesised? *Polymers* **2019**, *11*, 354.

(475) Furneaux, R. H.; Miller, I. J. Isolation and C-NMR spectral study of the water soluble polysaccharides from four south african red algae. *Bot. Mar.* **1986**, *29*, 3−10.

(476) Yamagaki, T.; Maeda, M.; Kanazawa, K.; Ishizuka, Y.; Nakanishi, H. Structural clarification of *Caulerpa* cell wall/M,3-xylan by NMR spectroscopy. *Biosci., Biotechnol., Biochem.* **1997**, *61*, 1077−1080.

(477) Ciancia, M.; Alberghina, J.; Arata, P.; Benavides, H.; Leliaert, F.; Verbruggen, H.; Estevez, J. Characterization of cell wall polysaccharides of the coencocytic green seaweed *Bryopsis plumosa* (Bryopsidaceae, Chlorophyta) from the argentine coast. *J. Phycol.* **2012**, *48*, 326−35.

(478) Lahaye, M.; Rondeau-Mouro, C.; Deniaud, E.; Buléon, A. Solid-state ^{13}C NMR spectroscopy studies of xylans in the cell wall of *Palmaria palmata* (L. Kuntze, Rhodophyta). *Carbohydr. Res.* **2003**, *338*, 1559−1569.

(479) Deniaud, E.; Quemener, B.; Fleurence, J.; Lahaye, M. Structural studies of the mix-linked β-$(1{\rightarrow}3)$/β-$(1{\rightarrow}4)$-D-xylans from the cell wall of *Palmaria palmata* (Rhodophyta). *Int. J. Biol. Macromol.* **2003**, *33*, 9−18.

(480) Hervé, C.; Siméon, A.; Jam, M.; Cassin, A.; Johnson, K. L.; Salmeán, A. A.; Willats, W. G.; Doblin, M. S.; Bacic, A.; Kloareg, B. Arabinogalactan proteins have deep roots in eukaryotes: identification of genes and epitopes in brown algae and their role in *Fucus serratus* embryo development. *New Phytol.* **2016**, *209*, 1428−1441.

(481) Johnson, K. L.; Cassin, A. M.; Lonsdale, A.; Wong, G. K.-S.; Soltis, D. E.; Miles, N. W.; Melkonian, M.; Melkonian, B.; Deyholos, M. K.; Leebens-Mack, J.; et al. Insights into the evolution of hydroxyproline-rich glycoproteins from 1000 plant transcriptomes. *Plant Physiol.* **2017**, *174*, 904−921.

(482) Lahaye, M. Developments on gelling algal galactans, their structure and physico-chemistry. *J. Appl. Phycol.* **2001**, *13*, 173−184.

(483) van de Velde, F.; Pereira, L.; Rollema, H. S. The revised NMR chemical shift data of carrageenans. *Carbohydr. Res.* **2004**, *339*, 2309−2313.

(484) Rocha, H. A.; Moraes, F. A.; Trindade, E. S.; Franco, C. R.; Torquato, R. J.; Veiga, S. S.; Valente, A. P.; Mourão, P. A.; Leite, E. L.; Nader, H. B.; et al. Structural and hemostatic activities of a sulfated galactofucan from the brown alga *Spatoglossum schroederi*. An ideal antithrombotic agent? *J. Biol. Chem.* **2005**, *280*, 41278−41288.

(485) Farias, E. H.; Pomin, V. H.; Valente, A. P.; Nader, H. B.; Rocha, H. A.; Mourão, P. A. A preponderantly 4-sulfated, 3-linked galactan from the green alga *Codium isthmocladum*. *Glycobiology* **2007**, *18*, 250−259.

(486) Li, B.; Lu, F.; Wei, X.; Zhao, R. Fucoidan: structure and bioactivity. *Molecules* **2008**, *13*, 1671−1695.

(487) Deniaud-Bouët, E.; Hardouin, K.; Potin, P.; Kloareg, B.; Hervé, C. A review about brown algal cell walls and fucose-containing sulfated polysaccharides: Cell wall context, biomedical properties and key research challenges. *Carbohydr. Polym.* **2017**, *175*, 395−408.

(488) Gordon-Mills, E.; Tate, M.; Hounslow, A. Use of solid and gel state ^{13}C NMR spectroscopy for differentiation between agarophytes and carrageenophytes. *Hydrobiologia* **1990**, *204*−*205*, 629−636.

(489) Lahaye, M.; Rochas, C. Chemical structure and physico-chemical properties of agar. *Hydrobiologia* **1991**, *221*, 137−148.

(490) Youngs, H. L.; Gretz, M. R.; West, J. A.; Sommerfeld, M. R. The cell wall chemistry of *Bangia atropurpurea* (Bangiales, Rhodophyta) and *Bostrychia moritziana* (Ceramiales, Rhodophyta) from marine and freshwater environments. *Phycol. Res.* **1998**, *46*, 63−73.

(491) Haug, A.; Larsen, B.; Smidsrød, O. Uronic acid sequence in alginate from different sources. *Carbohydr. Res.* **1974**, *32*, 217−225.

(492) Lahaye, M.; Robic, A. Structure and functional properties of ulvan, a polysaccharide from green seaweeds. *Biomacromolecules* **2007**, *8*, 1765−1774.

(493) Blokker, P.; Schouten, S.; van den Ende, H.; de Leeuw, J. W.; Hatcher, P. G.; Sinninghe Damsté, J. S. Chemical structure of algaenans from the fresh water algae *Tetraedron minimum, Scenedesmus communis* and *Pediastrum boryanum. Org. Geochem.* **1998**, *29*, 1453−1468.

(494) Rodríguez, M. C.; Cerezo, A. S. The resistant 'biopolymer' in cell walls of *Coelastrum sphaericum. Phytochemistry* **1996**, *43*, 731−734.

(495) Rodríguez, M. C.; Noseda, M. D.; Cerezo, A. S. The Fibrillar Polysaccharides and their Linkage to Algaenan in the Trilaminar Layer of the Cell Wall of *Coelastrum Sphaericum* (Chlorophyceae). *J. Phycol.* **1999**, *35*, 1025−1031.

(496) Simpson, A. J.; Zang, X.; Kramer, R.; Hatcher, P. G. New insights on the structure of algaenan from *Botryoccocus braunii* race A and its hexane insoluble botryals based on multidimensional NMR spectroscopy and electrospray-mass spectrometry techniques. *Phytochemistry* **2003**, *62*, 783−796.

(497) Rahman, M. A.; Halfar, J. First evidence of chitin in calcified coralline algae: new insights into the calcification process of *Clathromorphum compactum. Sci. Rep.* **2015**, *4*, 6162.

(498) Rahman, M. A.; Halfar, J.; Adey, W. H.; Nash, M.; Paulo, C.; Dittrich, M. The role of chitin-rich skeletal organic matrix on the crystallization of calcium carbonate in the crustose coralline alga *Leptophytum foecundum. Sci. Rep.* **2019**, *9*, 11869.

(499) Ehrlich, H. Chitin and collagen as universal and alternative templates in biomineralization. *Int. Geol. Rev.* **2010**, *52*, 661−699.

(500) Kitaoku, Y.; Fukamizo, T.; Numata, T.; Ohnuma, T. Chitin oligosaccharide binding to the lysin motif of a novel type of Chitinase from the multicellular green alga. *Plant Mol. Biol.* **2017**, *93*, 97−108.

(501) Kawasaki, T.; Tanaka, M.; Fujie, M.; Usami, S.; Sakai, K.; Yamada, T. Chitin synthesis in chlorovirus CVK2-infected Chlorella cells. *Virology* **2002**, *302*, 123−131.

(502) Hecky, R. E.; Mopper, K.; Kilham, P.; Degens, E. T. The amino acid and sugar composition of diatom cell-walls. *Mar. Biol.* **1973**, *19*, 323−331.

(503) Bedoshvili, Y. D.; Likhoshway, Y. V. Cellular mechanisms of diatom valve morphogenesis. *Diatoms: fundamentals and applications.* **2019**, 99−114.

(504) Shrestha, R. P.; Tesson, B.; Norden-Krichmar, T.; Federowicz, S.; Hildebrand, M.; Allen, A. E. Whole transcriptome analysis of the silicon response of the diatom *Thalassiosira pseudonana. BMC Genomics* **2012**, *13*, 499.

(505) Hildebrand, M.; Lerch, S. J. L.; Shrestha, R. P. Understanding diatom cell wall silicification—moving forward. *Front. Mar. Sci.* **2018**, DOI: 10.3389/fmars.2018.00125.

(506) Kroger, N.; Sandhage, K. H. From diatom biomolecules to bioinspired syntheses of silica- and titania-based materials. *MRS Bull.* **2010**, *35*, 122−126.

(507) Tesson, B.; Masse, S.; Laurent, G.; Maquet, J.; Livage, J.; Martin-Jézéquel, V.; Coradin, T. Contribution of multi-nuclear solid state NMR to the characterization of the *Thalassiosira pseudonana* diatom cell wall. *Anal. Bioanal. Chem.* **2008**, *390*, 1889−1898.

(508) Görlich, S.; Pawolski, D.; Zlotnikov, I.; Kröger, N. Control of biosilica morphology and mechanical performance by the conserved diatom gene *Silicanin-1. Commun. Biol.* **2019**, *2*, 245.

(509) Ehren, H. L.; Kolbe, F.; Paioni, A. L.; Brunner, E.; Baldus, M. DNP-supported solid-state NMR studies of ${}^{13}C, {}^{15}N, {}^{29}Si$-enriched biosilica of *Cyclotella cryptica* and *Thalassiosira pseudonan. Discovery Mater.* **2021**, *1*, 9.

(510) Kröger, N.; Poulsen, N. Diatoms—from cell wall biogenesis to nanotechnology. *Annu. Rev. Genet.* **2008**, *42*, 83−107.

(511) Scheffel, A.; Poulsen, N.; Shian, S.; Kröger, N. Nanopatterned protein microrings from a diatom that direct silica morphogenesis. *Proc. Natl. Acad. Sci. U. S. A.* **2011**, *108*, 3175−3180.

(512) Brunner, E.; Richthammer, P.; Ehrlich, H.; Paasch, S.; Simon, P.; Ueberlein, S.; van Pée, K. H. Chitin-based organic networks: an integral part of cell wall biosilica in the diatom *Thalassiosira pseudonana. Angew. Chem., Int. Ed.* **2009**, *48*, 9724−9727.

(513) Tesson, B.; Hildebrand, M. Extensive and intimate association of the cytoskeleton with forming silica in diatoms: control over patterning on the meso- and micro-scale. *PLoS One* **2010**, *5*, No. e14300.

(514) Tesson, B.; Hildebrand, M. Dynamics of silica cell wall morphogenesis in the diatom *Cyclotella cryptica*: Substructure formation and the role of microfilaments. *J. Struct. Biol.* **2010**, *169*, 62−74.

(515) Kolbe, F.; Ehren, H. L.; Kohrs, S.; Butscher, D.; Reiß, L.; Baldus, M.; Brunner, E. Solid-state NMR spectroscopic studies of ${}^{13}C, {}^{15}N, {}^{29}Si$-enriched biosilica from the marine diatom *Cyclotella cryptica. Discovery Mater.* **2021**, *1*, 3.

(516) Bertermann, R.; Kröger, N.; Tacke, R. Solid-state ${}^{29}Si$ MAS NMR studies of diatoms: structural characterization of biosilica deposits. *Anal. Bioanal. Chem.* **2003**, *375*, 630−634.

(517) Johnston, M. R.; Gascooke, J. R.; Ellis, A. V.; Leterme, S. C. Diatoms response to salinity changes: investigations using single pulse and cross polarisation magic angle spinning ${}^{29}Si$ NMR spectra. *Analyst* **2018**, *143*, 4930−4935.

(518) Tesson, B.; Hildebrand, M. Characterization and localization of insoluble organic matrices associated with diatom cell walls: insight into their roles during cell wall formation. *PLoS One* **2013**, *8*, No. e61675.

(519) Arias, J. L.; Fernández, M. S. Polysaccharides and proteoglycans in calcium carbonate-based biomineralization. *Chem. Rev.* **2008**, *108*, 4475−4482.

(520) Falk, M.; Smith, D. G.; McLachlan, J.; McInnes, A. G. Studies on chitan (β-($1\rightarrow4$)-linked 2-acetamido-2-deoxy-D-glucan) fibers of the diatom *Thalassiosira fluviatilis* hustedt: II. proton magnetic resonance, Infrared, and X-ray studies. *Can. J. Chem.* **1966**, *44*, 2269−2281.

(521) Ford, C. W.; Percival, E. The carbohydrates of phaeodactylum tricornutum. Part I. preliminary examination of the organism, and characterisation of low molecular weight material and of a glucan. *J. Chem. Soc.* **1965**, 7035−7041.

(522) Wisser, D.; Brückner, S. I.; Wisser, F. M.; Althoff-Ospelt, G.; Getzschmann, J.; Kaskel, S.; Brunner, E. ${}^{1}H$-${}^{13}C$-${}^{29}Si$ triple resonance and REDOR solid-state NMR-A tool to study interactions between biosilica and organic molecules in diatom cell walls. *Solid State Nucl. Magn. Reson.* **2015**, *66−67*, 33−39.

(523) Akhter, M.; Dutta Majumdar, R.; Fortier-McGill, B.; Soong, R.; Liaghati-Mobarhan, Y.; Simpson, M.; Arhonditsis, G.; Schmidt, S.; Heumann, H.; Simpson, A. J. Identification of aquatically available carbon from algae through solution-state NMR of whole ${}^{13}C$-labelled cells. *Anal. Bioanal. Chem.* **2016**, *408*, 4357−4370.

(524) Bouillaud, D.; Heredia, V.; Castaing-Cordier, T.; Drouin, D.; Charrier, B.; Gonçalves, O.; Farjon, J.; Giraudeau, P. Benchtop flow NMR spectroscopy as an online device for the *in vivo* monitoring of lipid accumulation in microalgae. *Algal Res.* **2019**, *43*, 101624.

(525) Bouillaud, D.; Drouin, D.; Charrier, B.; Jacquemmoz, C.; Farjon, J.; Giraudeau, P.; Gonçalves, O. Using benchtop NMR spectroscopy as an online non-invasive *in vivo* lipid sensor for microalgae cultivated in photobioreactors. *Process Biochem.* **2020**, *93*, 63−68.

(526) Mobarhan, Y. L.; Fortier-McGill, B.; Soong, R.; Maas, W. E.; Fey, M.; Monette, M.; Stronks, H. J.; Schmidt, S.; Heumann, H.; Norwood, W.; et al. Comprehensive multiphase NMR applied to a living organism. *Chem. Sci.* **2016**, *7*, 4856−4866.

(527) Ghosh Biswas, R.; Fortier-McGill, B.; Akhter, M.; Soong, R.; Ning, P.; Bastawrous, M.; Jenne, A.; Schmidig, D.; De Castro, P.; Graf, S.; Kuehn, T.; Busse, F.; Struppe, J.; Fey, M.; Heumann, H.; Boenisch, H.; Gundy, M.; Simpson, M. J.; Simpson, A. J.; et al. *Ex vivo* Comprehensive Multiphase NMR of whole organisms: a complementary tool to *in vivo* NMR. *Analytica Chimica Acta: X* **2020**, *6*, 100051.

(528) Chauton, M. S.; Størseth, T. HR MAS NMR spectroscopy of marine microalgae. *Modern Magnetic Resonance*; Springer International Publishing: Cham, Switzerland, 2018; pp 1927−1935.

(529) Chauton, M. S.; Størseth, T. R.; Krane, J. High-resolution magic angle spinning NMR analysis of whole cells of *Chaetoceros muelleri* (Bacillariophyceae) and comparison with ${}^{13}C$-NMR and distortionless

enhancement by polarization transfer ^{13}C-NMR analysis of lipophilic extracts. *J. Phycol.* **2004**, *40*, 611−618.

(530) Skogen Chauton, M.; Røvik Størseth, T.; Johnsen, G. High-resolution magic angle spinning ^{1}H NMR analysis of whole cells of *Thalassiosira pseudonana* (Bacillariophyceae): broad range analysis of metabolic composition and nutritional value. *J. Appl. Phycol.* **2003**, *15*, 533−542.

(531) Chauton, M.; Optun, O.; Bathen, T.; Volent, Z; Gribbestad, I.; Johnsen, G HR MAS ^{1}H NMR spectroscopy analysis of marine microalgal whole cells. *Mar. Ecol.: Prog. Ser.* **2003**, *256*, 57−62.

(532) Arnold, A.; Genard, B.; Zito, F.; Tremblay, R.; Warschawski, D.; Marcotte, I. Identification of lipid and saccharide constituents of whole microalgal cells by ^{13}C solid-state NMR. *Biochim. Biophys. Acta, Biomembr.* **2015**, *1848*, 369−377.

(533) Arnold, A. A.; Bourgouin, J. P.; Genard, B.; Warschawski, D. E.; Tremblay, R.; Marcotte, I. Whole cell solid-state NMR study of *Chlamydomonas reinhardtii* microalgae. *J. Biomol. NMR* **2018**, *70*, 123−131.

(534) Poulhazan, A.; Dickwella Widanage, M. C.; Muszynski, A.; Arnold, A. A.; Warschawski, D. E.; Azadi, P.; Marcotte, I.; Wang, T. Identification and quantification of glycans in whole cells: architecture of microalgal polysaccharides described by solid-state nuclear magnetic resonance. *J. Am. Chem. Soc.* **2021**, *143*, 19374.

(535) Magazù, S.; Migliardo, F.; Gonzalez, M. A.; Mondelli, C.; Parker, S. F.; Vertessy, B. G. Molecular mechanisms of survival strategies in extreme conditions. *Life (Basel, Switz.)* **2012**, *2*, 364−376.

(536) Gupta, A.; Gupta, R.; Singh, R. L. Microbes and environment. *Principles and applications of environmental biotechnology for a sustainable future*; Springer Singapore: Singapore, 2017; pp 43−84.

(537) Nelson, M. L.; Dinardo, A.; Hochberg, J.; Armelagos, G. J. Brief communication: mass spectroscopic characterization of tetracycline in the skeletal remains of an ancient population from Sudanese Nubia 350−550 CE. *Am. J. Phys. Anthropol.* **2010**, *143*, 151−154.

(538) Aminov, R. I. A brief history of the antibiotic era: lessons learned and challenges for the future. *Front. Microbiol.* **2010**, *1*, 134−134.

(539) Kapoor, G.; Saigal, S.; Elongavan, A. Action and resistance mechanisms of antibiotics: A guide for clinicians. *J. Anaesthesiol Clin Pharmacol* **2017**, *33*, 300−305.

(540) Reygaert, W. C. An overview of the antimicrobial resistance mechanisms of bacteria. *AIMS Microbiol* **2018**, *4*, 482−501.

(541) Iwu, C. D.; Korsten, L.; Okoh, A. I. The incidence of antibiotic resistance within and beyond the agricultural ecosystem: A concern for public health. *MicrobiologyOpen* **2020**, *9*, No. e1035.

(542) Blair, J. M.; Richmond, G. E.; Piddock, L. J. Multidrug efflux pumps in Gram-negative bacteria and their role in antibiotic resistance. *Future Microbiol.* **2014**, *9*, 1165−1177.

(543) Giedraitienè, A.; Vitkauskienè, A.; Naginienè, R.; Pavilonis, A. Antibiotic resistance mechanisms of clinically important bacteria. *Medicina* **2011**, *47*, 19.

(544) Shunmugaperumal, T. The role of biofilms in device-related infections. *J. Med. Devices* **2011**, *5*, 016501.

(545) Magana, M.; Sereti, C.; Ioannidis, A.; Mitchell, C. A.; Ball, A. R.; Magiorkinis, E.; Chatzipanagiotou, S.; Hamblin, M. R.; Hadjifrangiskou, M.; Tegos, G. P. Options and limitations in clinical investigation of bacterial biofilms. *Clin. Microbiol. Rev.* **2018**, *31*, e00084-16.

(546) Zhang, B.; Powers, R. Analysis of bacterial biofilms using NMR-based metabolomics. *Future Med. Chem.* **2012**, *4*, 1273−1306.

(547) Reichhardt, C.; Ferreira, J. A. G.; Joubert, L.-M.; Clemons, K. V.; Stevens, D. A.; Cegelski, L. Analysis of the *Aspergillus fumigatus* biofilm extracellular matrix by solid-state nuclear magnetic resonance spectroscopy. *Eukaryotic Cell* **2015**, *14*, 1064−1072.

(548) Romaniuk, J. A. H.; Cegelski, L. Bacterial cell wall composition and the influence of antibiotics by cell-wall and whole-cell NMR. *Philos. Trans. R. Soc., B* **2015**, *370*, 20150024.

(549) Kern, T.; Giffard, M.; Hediger, S.; Amoroso, A.; Giustini, C.; Bui, N. K.; Joris, B.; Bougault, C.; Vollmer, W.; Simorre, J.-P. Dynamics characterization of fully hydrated bacterial cell walls by solid-state

NMR: evidence for cooperative binding of metal ions. *J. Am. Chem. Soc.* **2010**, *132*, 10911−10919.

(550) Pasquina-Lemonche, L.; Burns, J.; Turner, R. D.; Kumar, S.; Tank, R.; Mullin, N.; Wilson, J. S.; Chakrabarti, B.; Bullough, P. A.; Foster, S. J.; et al. The architecture of the Gram-positive bacterial cell wall. *Nature* **2020**, *582*, 294−297.

(551) Huang, K. C.; Mukhopadhyay, R.; Wen, B.; Gitai, Z.; Wingreen, N. S. Cell shape and cell-wall organization in Gram-negative bacteria. *Proc. Natl. Acad. Sci. U. S. A.* **2008**, *105*, 19282−19287.

(552) Wickham, J. R.; Halye, J. L.; Kashtanov, S.; Khandogin, J.; Rice, C. V. Revisiting magnesium chelation by teichoic acid with phosphorus solid-state NMR and theoretical calculations. *J. Phys. Chem. B* **2009**, *113*, 2177−2183.

(553) Romaniuk, J. A. H.; Cegelski, L. Peptidoglycan and Teichoic Acid Levels and Alterations in *Staphylococcus aureus* by cell-wall and whole-cell nuclear magnetic resonance. *Biochemistry* **2018**, *57*, 3966−3975.

(554) Bugg, T. D. H.; Braddick, D.; Dowson, C. G.; Roper, D. I. Bacterial cell wall assembly: still an attractive antibacterial target. *Trends Biotechnol.* **2011**, *29*, 167−173.

(555) Taguchi, A.; Welsh, M. A.; Marmont, L. S.; Lee, W.; Sjodt, M.; Kruse, A. C.; Kahne, D.; Bernhardt, T. G.; Walker, S. FtsW is a peptidoglycan polymerase that is functional only in complex with its cognate penicillin-binding protein. *Nat. Microbiol.* **2019**, *4*, 587−594.

(556) Cho, H.; Wivagg, C. N.; Kapoor, M.; Barry, Z.; Rohs, P. D. A.; Suh, H.; Marto, J. A.; Garner, E. C.; Bernhardt, T. G. Bacterial cell wall biogenesis is mediated by SEDS and PBP polymerase families functioning semi-autonomously. *Nat. Microbiol.* **2016**, *1*, 16172.

(557) Meeske, A. J.; Riley, E. P.; Robins, W. P.; Uehara, T.; Mekalanos, J. J.; Kahne, D.; Walker, S.; Kruse, A. C.; Bernhardt, T. G.; Rudner, D. Z. SEDS proteins are a widespread family of bacterial cell wall polymerases. *Nature* **2016**, *537*, 634−638.

(558) Fagan, R. P.; Fairweather, N. F. Biogenesis and functions of bacterial S-layers. *Nat. Rev. Microbiol.* **2014**, *12*, 211−222.

(559) Sára, M.; Sleytr, U. B. S-layer proteins. *J. Bacteriol.* **2000**, *182*, 859−868.

(560) Sleytr, U. B.; Györvary, E.; Pum, D. Crystallization of S-layer protein lattices on surfaces and interfaces. *Prog. Org. Coat.* **2003**, *47*, 279−287.

(561) Messner, P.; Sleytr, U. B. Crystalline bacterial cell-surface layers. *Adv. Microb. Physiol.* **1992**, *33*, 213−275.

(562) Rajagopal, M.; Walker, S. Envelope structures of Gram-positive bacteria. *Curr. Top. Microbiol. Immunol.* **2015**, *404*, 1−44.

(563) Caroff, M.; Novikov, A. LPS structure, function, and heterogeneity. *Endotoxin detection and control in pharma, limulus, and mammalian systems*; Springer International Publishing: Cham, Switzerland, 2019; pp 53−93.

(564) Jankute, M.; Cox, J. A. G.; Harrison, J.; Besra, G. S. Assembly of the mycobacterial cell wall. *Annu. Rev. Microbiol.* **2015**, *69*, 405−423.

(565) Mayer, C.; Kluj, R. M.; Mühleck, M.; Walter, A.; Unsleber, S.; Hottmann, I.; Borisova, M. Bacteria's different ways to recycle their own cell wall. *Int. J. Med. Microbiol.* **2019**, *309*, 151326.

(566) Kim, S. J.; Chang, J.; Singh, M. Peptidoglycan architecture of Gram-positive bacteria by solid-state NMR. *Biochim. Biophys. Acta, Biomembr.* **2015**, *1848*, 350−362.

(567) Zhou, X.; Cegelski, L. Nutrient-dependent structural changes in *S. aureus* peptidoglycan revealed by solid-state NMR spectroscopy. *Biochemistry* **2012**, *51*, 8143−8153.

(568) Schanda, P.; Triboulet, S.; Laguri, C.; Bougault, C. M.; Ayala, I.; Callon, M.; Arthur, M.; Simorre, J.-P. Atomic model of a cell-wall cross-linking enzyme in complex with an intact bacterial peptidoglycan. *J. Am. Chem. Soc.* **2014**, *136*, 17852−17860.

(569) Beveridge, T. J. Structures of Gram-negative cell walls and their derived membrane vesicles. *J. Bacteriol.* **1999**, *181*, 4725−4733.

(570) Laguri, C.; Silipo, A.; Martorana, A. M.; Schanda, P.; Marchetti, R.; Polissi, A.; Molinaro, A.; Simorre, J. P. Solid state NMR studies of intact lipopolysaccharide endotoxin. *ACS Chem. Biol.* **2018**, *13*, 2106−2113.

(571) Di Lorenzo, F.; Duda, K. A.; Lanzetta, R.; Silipo, A.; De Castro, C.; Molinaro, A. A journey from structure to function of bacterial lipopolysaccharides. *Chem. Rev.* **2021**, DOI: 10.1021/acs.chemrev.0c01321.

(572) Jachymek, W.; Niedziela, T.; Petersson, C.; Lugowski, C.; Czaja, J.; Kenne, L. Structures of the O-specific polysaccharides from *Yokenella regensburgei* (*Koserella trabulsii*) strains PCM 2476, 2477, 2478, and 2494: high-resolution magic-angle spinning NMR investigation of the O-specific polysaccharides in native lipopolysaccharides and directly on the surface of living bacteria. *Biochemistry* **1999**, *38*, 11788−11795.

(573) Dekoninck, K.; Létoquart, J.; Laguri, C.; Demange, P.; Bevernaegie, R.; Simorre, J.-P.; Dehu, O.; Iorga, B.; Elias, B.; Cho, S.-H. Defining the function of OmpA in the Rcs stress response. *eLife* **2020**, *9*, e60861.

(574) Brown, S.; Santa Maria, J. P., Jr.; Walker, S. Wall teichoic acids of Gram-positive bacteria. *Annu. Rev. Microbiol.* **2013**, *67*, 313−336.

(575) Wickham, J. R.; Rice, C. V. Solid-state NMR studies of bacterial lipoteichoic acid adsorption on different surfaces. *Solid State Nucl. Magn. Reson.* **2008**, *34*, 154−161.

(576) Rice, C. V.; Wickham, J. R. Heterogeneous binding of lipoteichoic acid to the surface of titanium dioxide as determined with ^{31}P solid-state NMR spectroscopy. *J. Am. Chem. Soc.* **2005**, *127*, 856−857.

(577) Halye, J. L.; Rice, C. V. Cadmium chelation by bacterial teichoic acid from solid-state nuclear magnetic resonance spectroscopy. *Biomacromolecules* **2010**, *11*, 333−340.

(578) Renault, M.; Boxtel, R.; Bos, M.; Post, J.; Tommassen, J.; Baldus, M. Cellular solid-state nuclear magnetic resonance spectroscopy. *Proc. Natl. Acad. Sci. U. S. A.* **2012**, *109*, 4863−4868.

(579) Nordmark, E. L.; Yang, Z.; Huttunen, E.; Widmalm, G. Structural studies of the exopolysaccharide produced by *Propionibacterium freudenreichii* ssp. *shermanii* JS. *Biomacromolecules* **2005**, *6*, 521−523.

(580) Bui, N. K.; Eberhardt, A.; Vollmer, D.; Kern, T.; Bougault, C.; Tomasz, A.; Simorre, J. P.; Vollmer, W. Isolation and analysis of cell wall components from *Streptococcus pneumoniae*. *Anal. Biochem.* **2012**, *421*, 657−666.

(581) De Sa Peixoto, P.; Roiland, C.; Thomas, D.; Briard-Bion, V.; Le Guellec, R.; Parayre, S.; Deutsch, S. M.; Jan, G.; Guyomarc'h, F. Recrystallized S-layer protein of a probiotic *Propionibacterium*: structural and nanomechanical changes upon temperature or pH shifts probed by solid-state NMR and AFM. *Langmuir* **2015**, *31*, 199−208.

(582) Lee, R. E.; Li, W.; Chatterjee, D.; Lee, R. E. Rapid structural characterization of the arabinogalactan and lipoarabinomannan in live mycobacterial cells using 2D and 3D HR-MAS NMR: structural changes in the arabinan due to ethambutol treatment and gene mutation are observed. *Glycobiology* **2004**, *15*, 139−151.

(583) Wieruszeski, J. M.; Bohin, A.; Bohin, J. P.; Lippens, G. *In vivo* detection of the cyclic osmoregulated periplasmic glucan of *Ralstonia solanacearum* by high-resolution magic angle spinning NMR. *J. Magn. Reson.* **2001**, *151*, 118−123.

(584) Li, W.; Lee, R. E.; Lee, R. E.; Li, J. Methods for acquisition and assignment of multidimensional high-resolution magic angle spinning NMR of whole cell bacteria. *Anal. Chem.* **2005**, *77*, 5785−5792.

(585) Kim, S. J.; Cegelski, L.; Studelska, D. R.; O'Connor, R. D.; Mehta, A. K.; Schaefer, J. Rotational-echo double resonance characterization of vancomycin binding sites in *Staphylococcus aureus*. *Biochemistry* **2002**, *41*, 6967−6977.

(586) Yang, H.; Singh, M.; Kim, S. J.; Schaefer, J. Characterization of the tertiary structure of the peptidoglycan of *Enterococcus faecalis*. *Biochim. Biophys. Acta, Biomembr.* **2017**, *1859*, 2171−2180.

(587) Patti, G. J.; Kim, S. J.; Yu, T.-Y.; Dietrich, E.; Tanaka, K. S. E.; Parr, T. R., Jr.; Far, A. R.; Schaefer, J. Vancomycin and oritavancin have different modes of action in *Enterococcus faecium*. *J. Mol. Biol.* **2009**, *392*, 1178−1191.

(588) Nygaard, R.; Romaniuk, J. A. H.; Rice, D. M.; Cegelski, L. Spectral snapshots of bacterial cell-wall composition and the influence of antibiotics by whole-cell NMR. *Biophys. J.* **2015**, *108*, 1380−1389.

(589) Singh, M.; Kim, S. J.; Sharif, S.; Preobrazhenskaya, M.; Schaefer, J. REDOR constraints on the peptidoglycan lattice architecture of *Staphylococcus aureus* and its FemA mutant. *Biochim. Biophys. Acta, Biomembr.* **2015**, *1848*, 363−368.

(590) Singh, M.; Chang, J.; Coffman, L.; Kim, S. J. Solid-state NMR characterization of amphomycin effects on peptidoglycan and wall teichoic acid biosyntheses in Staphylococcus aureus. *Sci. Rep.* **2016**, *6*, 31757.

(591) Kim, S. J.; Schaefer, J. Hydrophobic side-chain length determines activity and conformational heterogeneity of a vancomycin derivative bound to the cell wall of *Staphylococcus aureus*. *Biochemistry* **2008**, *47*, 10155−10161.

(592) Kim, S. J.; Matsuoka, S.; Patti, G. J.; Schaefer, J. Vancomycin derivative with damaged D-Ala-D-Ala binding cleft binds to crosslinked peptidoglycan in the cell wall of *Staphylococcus aureus*. *Biochemistry* **2008**, *47*, 3822−3831.

(593) Patti, G. J.; Chen, J.; Schaefer, J.; Gross, M. L. Characterization of structural variations in the peptidoglycan of vancomycin-susceptible *Enterococcus faecium*: understanding glycopeptide-antibiotic binding sites using mass spectrometry. *J. Am. Soc. Mass Spectrom.* **2008**, *19*, 1467−1475.

(594) Medeiros-Silva, J.; Jekhmane, S.; Paioni, A. L.; Gawarecka, K.; Baldus, M.; Swiezewska, E.; Breukink, E.; Weingarth, M. High-resolution NMR studies of antibiotics in cellular membranes. *Nat. Commun.* **2018**, *9*, 3963.

(595) Kern, T.; Hediger, S.; Müller, P.; Giustini, C.; Joris, B.; Bougault, C.; Vollmer, W.; Simorre, J. P. Toward the characterization of peptidoglycan structure and protein-peptidoglycan interactions by solid-state NMR spectroscopy. *J. Am. Chem. Soc.* **2008**, *130*, 5618−5619.

(596) Torrent, M.; Navarro, S.; Moussaoui, M.; Nogués, M. V.; Boix, E. Eosinophil cationic protein high-affinity binding to bacteria-wall lipopolysaccharides and peptidoglycans. *Biochemistry* **2008**, *47*, 3544−3555.

(597) Overall, S. A.; Zhu, S.; Hanssen, E.; Separovic, F.; Sani, M.-A. *In Situ* Monitoring of Bacteria under Antimicrobial Stress Using ^{31}P Solid-State NMR. *Int. J. Mol. Sci.* **2019**, *20*, 181.

(598) Separovic, F.; Keizer, D. W.; Sani, M.-A. In-cell solid-state NMR studies of antimicrobial peptides. *Front. Med. Technol.* **2020**, *2*, 610203.

(599) Balzer, M.; Witt, N.; Flemming, H. C.; Wingender, J. Faecal indicator bacteria in river biofilms. *Water Sci. Technol.* **2010**, *61*, 1105−1111.

(600) Berlanga, M.; Guerrero, R. Living together in biofilms: the microbial cell factory and its biotechnological implications. *Microb. Cell Fact.* **2016**, *15*, 165−165.

(601) Okada, M.; Sato, I.; Cho, S. J.; Iwata, H.; Nishio, T.; Dubnau, D.; Sakagami, Y. Structure of the *Bacillus subtilis* quorum-sensing peptide pheromone ComX. *Nat. Chem. Biol.* **2005**, *1*, 23−24.

(602) Hentzer, M.; Eberl, L.; Givskov, M. Transcriptome analysis of *Pseudomonas aeruginosa* biofilm development: anaerobic respiration and iron limitation. *Biofilms* **2005**, *2*, 37−61.

(603) Serra, D. O.; Richter, A. M.; Hengge, R. Cellulose as an architectural element in spatially structured *Escherichia coli* biofilms. *J. Bacteriol.* **2013**, *195*, 5540−5554.

(604) Hobley, L.; Harkins, C.; MacPhee, C. E.; Stanley-Wall, N. R. Giving structure to the biofilm matrix: an overview of individual strategies and emerging common themes. *FEMS Microbiol. Rev.* **2015**, *39*, 649−669.

(605) Secor, P. R.; Sweere, J. M.; Michaels, L. A.; Malkovskiy, A. V.; Lazzareschi, D.; Katznelson, E.; Rajadas, J.; Birnbaum, M. E.; Arrigoni, A.; Braun, K. R.; et al. Filamentous bacteriophage promote biofilm assembly and function. *Cell Host Microbe* **2015**, *18*, 549−559.

(606) Stoodley, P.; Sauer, K.; Davies, D. G.; Costerton, J. W. Biofilms as complex differentiated communities. *Annu. Rev. Microbiol.* **2002**, *56*, 187−209.

(607) Verderosa, A. D.; Totsika, M.; Fairfull-Smith, K. E. Bacterial biofilm eradication agents: a current review. *Front. Chem.* **2019**, *7*, 824.

(608) Wu, W.; Jin, Y.; Bai, F.; Jin, S. *Pseudomonas aeruginosa*; Academic Press: Boston, MA, 2015.

(609) Shen, Y.; Stojicic, S.; Haapasalo, M. Antimicrobial efficacy of chlorhexidine against bacteria in biofilms at different stages of development. *J. Endod.* **2011**, *37*, 657−661.

(610) Suarez, C.; Piculell, M.; Modin, O.; Langenheder, S.; Persson, F.; Hermansson, M. Thickness determines microbial community structure and function in nitrifying biofilms via deterministic assembly. *Sci. Rep.* **2019**, *9*, 5110.

(611) Muhammad, M. H.; Idris, A. L.; Fan, X.; Guo, Y.; Yu, Y.; Jin, X.; Qiu, J.; Guan, X.; Huang, T. Beyond risk: bacterial biofilms and their regulating approaches. *Front. Microbiol.* **2020**, *11*, 928.

(612) Garny, K.; Neu, T. R.; Horn, H.; Volke, F.; Manz, B. Combined application of ^{13}C NMR spectroscopy and confocal laser scanning microscopy—Investigation on biofilm structure and physico-chemical properties. *Chem. Eng. Sci.* **2010**, *65*, 4691−4700.

(613) Sutherland, I. W. The biofilm matrix—an immobilized but dynamic microbial environment. *Trends Microbiol.* **2001**, *9*, 222−227.

(614) Smolinska, A.; Blanchet, L.; Buydens, L. M. C.; Wijmenga, S. S. NMR and pattern recognition methods in metabolomics: from data acquisition to biomarker discovery: a review. *Anal. Chim. Acta* **2012**, *750*, 82−97.

(615) Xu, Y.; Wang, C.; Hou, J.; Wang, P.; You, G.; Miao, L.; Lv, B.; Yang, Y. Effects of cerium oxide nanoparticles on the species and distribution of phosphorus in enhanced phosphorus removal sequencing batch biofilm reactor. *Bioresour. Technol.* **2017**, *227*, 393−397.

(616) Zeng, F.; Jin, W.; Zhao, Q. Temperature effect on extracellular polymeric substances (EPS) and phosphorus accumulating organisms (PAOs) for phosphorus release of anaerobic sludge. *RSC Adv.* **2019**, *9*, 2162−2171.

(617) Flemming, H.-C.; Wingender, J. The biofilm matrix. *Nat. Rev. Microbiol.* **2010**, *8*, 623−633.

(618) Mandakhalikar, K. D.; Rahmat, J. N.; Chiong, E.; Neoh, K. G.; Shen, L.; Tambyah, P. A. Extraction and quantification of biofilm bacteria: method optimized for urinary catheters. *Sci. Rep.* **2018**, *8*, 8069.

(619) Chiba, A.; Sugimoto, S.; Sato, F.; Hori, S.; Mizunoe, Y. A refined technique for extraction of extracellular matrices from bacterial biofilms and its applicability. *Microb. Biotechnol.* **2015**, *8*, 392−403.

(620) Cegelski, L. Bottom-up and top-down solid-state NMR approaches for bacterial biofilm matrix composition. *J. Magn. Reson.* **2015**, *253*, 91−97.

(621) McCrate, O. A.; Zhou, X.; Reichhardt, C.; Cegelski, L. Sum of the parts: composition and architecture of the bacterial extracellular matrix. *J. Mol. Biol.* **2013**, *425*, 4286−4294.

(622) Jeffries, J.; Thongsomboon, W.; Visser, J. A.; Enriquez, K.; Yager, D.; Cegelski, L. Variation in the ratio of curli and phosphoethanolamine cellulose associated with biofilm architecture and properties. *Biopolymers* **2021**, *112*, 23395.

(623) Reichhardt, C.; Fong, J. C. N.; Yildiz, F.; Cegelski, L. Characterization of the *Vibrio cholerae* extracellular matrix: a top-down solid-state NMR approach. *Biochim. Biophys. Acta, Biomembr.* **2015**, *1848*, 378−383.

(624) El Mammeri, N.; Hierrezuelo, J.; Tolchard, J.; Camara-Almiron, J.; Caro-Astorga, J.; Alvarez-Mena, A.; Dutour, A.; Berbon, M.; Shenoy, J.; Morvan, E.; Grelard, A.; Kauffmann, B.; Lecomte, S.; Vicente, A.; Habenstein, B.; Romero, D.; Loquet, A.; et al. Molecular architecture of bacterial amyloids in *Bacillus* biofilms. *FASEB J.* **2019**, *33*, 12146−12163.

(625) Thongsomboon, W.; Serra, D. O.; Possling, A.; Hadjineophytou, C.; Hengge, R.; Cegelski, L. Phosphoethanolamine cellulose: A naturally produced chemically modified cellulose. *Science* **2018**, *359*, 334−338.

(626) Olsén, A.; Jonsson, A.; Normark, S. Fibronectin binding mediated by a novel class of surface organelles on *Escherichia coli*. *Nature* **1989**, *338*, 652−655.

(627) Reichhardt, C.; Lim, J. Y.; Rice, D.; Fong, J. N.; Cegelski, L. Structure and function of bacterial biofilms by solid-state NMR. *Biophys. J.* **2014**, *106*, 192a.

(628) Jeffries, J.; Fuller, G. G.; Cegelski, L. Unraveling *Escherichia coli*'s cloak: identification of phosphoethanolamine cellulose, its functions, and applications. *Microbiol. Insights* **2019**, *12*, 1178636119865234.

(629) Tang, W.; Bhatt, A.; Smith, A. N.; Crowley, P. J.; Brady, L. J.; Long, J. R. Specific binding of a naturally occurring amyloidogenic fragment of *Streptococcus mutans* adhesin P1 to intact P1 on the cell surface characterized by solid state NMR spectroscopy. *J. Biomol. NMR* **2016**, *64*, 153−164.

(630) Van Gerven, N.; Van der Verren, S. E.; Reiter, D. M.; Remaut, H. The role of functional amyloids in bacterial virulence. *J. Mol. Biol.* **2018**, *430*, 3657−3684.

(631) Jordal, P. B.; Dueholm, M. S.; Larsen, P.; Petersen, S. V.; Enghild, J. J.; Christiansen, G.; Højrup, P.; Nielsen, P. H.; Otzen, D. E. Widespread abundance of functional bacterial amyloid in mycolata and other gram-positive bacteria. *Appl. Environ. Microbiol.* **2009**, *75*, 4101−4110.

(632) Lattner, D.; Flemming, H. C.; Mayer, C. ^{13}C-NMR study of the interaction of bacterial alginate with bivalent cations. *Int. J. Biol. Macromol.* **2003**, *33*, 81−88.

(633) Mayer, C.; Lattner, D.; Schürks, N. ^{13}C nuclear magnetic resonance studies on selectively labeled bacterial biofilms. *J. Ind. Microbiol. Biotechnol.* **2001**, *26*, 62−69.

(634) Diehl, A.; Roske, Y.; Ball, L.; Chowdhury, A.; Hiller, M.; Molière, N.; Kramer, R.; Stöppler, D.; Worth, C. L.; Schlegel, B.; et al. Structural changes of TasA in biofilm formation of *Bacillus subtilis*. *Proc. Natl. Acad. Sci. U. S. A.* **2018**, *115*, 3237−3242.

(635) Pandit, S.; Fazilati, M.; Gaska, K.; Derouiche, A.; Nypelö, T.; Mijakovic, I.; Kádár, R. The exo-polysaccharide component of extracellular matrix is essential for the viscoelastic properties of *Bacillus subtilis* biofilms. *Int. J. Mol. Sci.* **2020**, *21*, 6755.

(636) Jiao, Y.; Cody, G. D.; Harding, A. K.; Wilmes, P.; Schrenk, M.; Wheeler, K. E.; Banfield, J. F.; Thelen, M. P. Characterization of extracellular polymeric substances from acidophilic microbial biofilms. *Appl. Environ. Microbiol.* **2010**, *76*, 2916−2922.

(637) Lim, J. Y.; May, J. M.; Cegelski, L. Dimethyl sulfoxide and ethanol elicit increased amyloid biogenesis and amyloid-integrated biofilm formation in *Escherichia coli*. *Appl. Environ. Microbiol.* **2012**, *78*, 3369−3378.

(638) McLean, J. S.; Ona, O. N.; Majors, P. D. Correlated biofilm imaging, transport and metabolism measurements via combined nuclear magnetic resonance and confocal microscopy. *ISME J.* **2008**, *2*, 121−131.

(639) Zhang, Y.; Xu, A.; Lv, X.; Wang, Q.; Feng, C.; Lin, J. Non-invasive measurement, mathematical simulation and in situ detection of biofilm evolution in porous media: a review. *Appl. Sci.* **2021**, *11*, 1391.

(640) Caudill, E. R.; Hernandez, R. T.; Johnson, K. P.; O'Rourke, J. T.; Zhu, L.; Haynes, C. L.; Feng, Z. V.; Pedersen, J. A. Wall teichoic acids govern cationic gold nanoparticle interaction with Gram-positive bacterial cell walls. *Chem. Sci.* **2020**, *11*, 4106−4118.

(641) Joshi, A. S.; Singh, P.; Mijakovic, I. Interactions of gold and silver nanoparticles with bacterial biofilms: molecular interactions behind inhibition and resistance. *Int. J. Mol. Sci.* **2020**, *21*, 7658.

(642) Molina-Santiago, C.; Pearson, J. R.; Navarro, Y.; Berlanga-Clavero, M. V.; Caraballo-Rodriguez, A. M.; Petras, D.; García-Martín, M. L.; Lamon, G.; Haberstein, B.; Cazorla, F. M.; et al. The extracellular matrix protects *Bacillus subtilis* colonies from *Pseudomonas* invasion and modulates plant co-colonization. *Nat. Commun.* **2019**, *10*, 1919.

(643) Righi, V.; Constantinou, C.; Kesarwani, M.; Rahme, L. G.; Tzika, A. A. Effects of a small, volatile bacterial molecule on *Pseudomonas aeruginosa* bacteria using whole cell high-resolution magic angle spinning nuclear magnetic resonance spectroscopy and genomics. *Int. J. Mol. Med.* **2018**, *42*, 2129−2136.

(644) Gjersing, E. L.; Herberg, J. L.; Horn, J.; Schaldach, C. M.; Maxwell, R. S. NMR metabolomics of planktonic and biofilm modes of growth in *Pseudomonas aeruginosa*. *Anal. Chem.* **2007**, *79*, 8037−8045.

(645) Mizuno, S.; Amida, H.; Kobayashi, N.; Aizawa, S.; Tate, S. The NMR structure of FliK, the trigger for the switch of substrate specificity in the flagellar type III secretion apparatus. *J. Mol. Biol.* **2011**, *409*, 558−573.

(646) Lombardi, C.; Tolchard, J.; Bouillot, S.; Signor, L.; Gebus, C.; Liebl, D.; Fenel, D.; Teulon, J. M.; Brock, J.; Habenstein, B.; et al. Structural and functional characterization of the type three secretion system (T3SS) needle of *Pseudomonas aeruginosa*. *Front. Microbiol.* **2019**, *10*, 573.

(647) Stones, D. H.; Krachler, A. M. Fatal attraction: how bacterial adhesins affect host signaling and what we can learn from them. *Int. J. Mol. Sci.* **2015**, *16*, 2626−2640.

(648) Korotkov, K. V.; Sandkvist, M.; Hol, W. G. J. The type II secretion system: biogenesis, molecular architecture and mechanism. *Nat. Rev. Microbiol.* **2012**, *10*, 336−351.

(649) López-Castilla, A.; Thomassin, J.-L.; Bardiaux, B.; Zheng, W.; Nivaskumar, M.; Yu, X.; Nilges, M.; Egelman, E. H.; Izadi-Pruneyre, N.; Francetic, O. Structure of the calcium-dependent type 2 secretion pseudopilus. *Nat. Microbiol.* **2017**, *2*, 1686−1695.

(650) Shewmaker, F. The application of NMR techniques to bacterial adhesins. *Adv. Exp. Med. Biol.* **2011**, *715*, 241−256.

(651) Ramboarina, S.; Garnett, J. A.; Zhou, M.; Li, Y.; Peng, Z.; Taylor, J. D.; Lee, W.-c.; Bodey, A.; Murray, J. W.; Alguel, Y.; et al. Structural insights into serine-rich fimbriae from Gram-positive bacteria. *J. Biol. Chem.* **2010**, *285*, 32446−32457.

(652) Habenstein, B.; Loquet, A.; Hwang, S.; Giller, K.; Vasa, S. K.; Becker, S.; Habeck, M.; Lange, A. Hybrid structure of the type 1 pilus of uropathogenic *Escherichia coli*. *Angew. Chem., Int. Ed.* **2015**, *54*, 11691−11695.

(653) Demers, J.-P.; Habenstein, B.; Loquet, A.; Kumar Vasa, S.; Giller, K.; Becker, S.; Baker, D.; Lange, A.; Sgourakis, N. G. High-resolution structure of the Shigella type-III secretion needle by solid-state NMR and cryo-electron microscopy. *Nat. Commun.* **2014**, *5*, 4976.

(654) Demers, J.-P.; Sgourakis, N. G.; Gupta, R.; Loquet, A.; Giller, K.; Riedel, D.; Laube, B.; Kolbe, M.; Baker, D.; Becker, S.; et al. The common structural architecture of *Shigella flexneri* and *Salmonella typhimurium* type three secretion needles. *PLoS Pathog.* **2013**, *9*, No. e1003245.

(655) Loquet, A.; Sgourakis, N. G.; Gupta, R.; Giller, K.; Riedel, D.; Goosmann, C.; Griesinger, C.; Kolbe, M.; Baker, D.; Becker, S.; et al. Atomic model of the type III secretion system needle. *Nature* **2012**, *486*, 276−279.

(656) Guo, E. Z.; Desrosiers, D. C.; Zalesak, J.; Tolchard, J.; Berbon, M.; Habenstein, B.; Marlovits, T.; Loquet, A.; Galán, J. E. A polymorphic helix of a *Salmonella* needle protein relays signals defining distinct steps in type III secretion. *PLoS Biol.* **2019**, *17*, No. e3000351.

(657) Renault, M.; Pawsey, S.; Bos, M. P.; Koers, E. J.; Nand, D.; Tommassen-van Boxtel, R.; Rosay, M.; Tommassen, J.; Maas, W. E.; Baldus, M. Solid-state NMR spectroscopy on cellular preparations enhanced by dynamic nuclear polarization. *Angew. Chem., Int. Ed.* **2012**, *51*, 2998−3001.

(658) Judge, P. T.; Sesti, E. L.; Price, L. E.; Albert, B. J.; Alaniva, N.; Saliba, E. P.; Halbritter, T.; Sigurdsson, S. T.; Kyei, G. B.; Barnes, A. B. Dynamic nuclear polarization with electron decoupling in intact human cells and cell lysates. *J. Phys. Chem. B* **2020**, *124*, 2323−2330.